Università degli Studi di Cagliari

PHD DEGREE IN PHYSICS

Cycle XXXIII

TITLE OF THE PHD THESIS

Ab initio study of thermoelectric properties of layered materials

Scientific Disciplinary Sector
FIS/03 FISICA DELLA MATERIA

PhD Student: Roberta Farris

Supervisors Prof. Vincenzo Fiorentini
Prof. Alessio Filippetti

Final exam. Academic Year 2019 – 2020
Thesis defence: February 2021 Session

Declaration

I hereby declare that the contents of this thesis are original and have not been submitted, in whole or in part, in any previous application for a degree or qualification in this, or any other university. This thesis should be seen as resulting from my entire Ph.D work and contains nothing which is the outcome of work done in collaboration with others, except as specified in the text, References and Acknowledgements. It is based mostly on published articles.

Roberta Farris
January 2021

Acknowledgements

Many people have contributed to this work.

First and foremost I want to thank my supervisor Prof. Vincenzo Fiorentini for giving me the opportunity to enter the world of thermoelectricity. His scientific input and many ideas have been essential for all my thesis. During the past three years, he not only helped me a lot in my research, but also impressed me with his way of solving scientific problems. I do not think I could have completed my PhD study without his help, and it would have been impossible for me to publish my papers without his supervision.

Secondly, co-supervisor Prof. Alessio Filippetti was also very important for most of the work. His input was central for most of the material calculations done.
Thirdly, I want to thank Dr. Maria Barbara Maccioni who also gave me a lot of help at the beginning stage of my PhD career, and her help enabled me to begin my PhD research quickly.

I also want to thank Prof. Gian-Marco Rignanese for his hospitality during my stay at the Institute of Condensed Matter and Nanosciences (IMCN), Université Catholique de Louvain, Belgium. The experience I got there proved helpful in my work. Particular thanks are due to Dr. Francesco Ricci, for his patience in helping me to learn the new softwares. His support has been essential in achieving my goals. I really saved much time under his excellent assistance.

I would like to thank Prof. Luciano Colombo, for all the advice and direction he has given me concerning both academics and life. The enthusiasm he shows for the work is encouraging for me.

I would like to express my sincere gratitude to Università degli studi di Cagliari, for the Ph.D Scholarship and to all of the Department of Physics members for their help and support.

I want to thank Prof. Paolo Ruggerone, for supporting me all three years long and for the helpful tips on how to deal with oral presentations. I am also grateful to all the other people that make this such a great place to work: my office mates, for helping make these years just a little sweeter and to my colleagues for having shared so many funny moments.

Although the present work is presented as my own, it could not have been done without the help of my family. I would like to thank my parents, who raised me with love and supported me in all my pursuits, for always providing me with the opportunities to become a better person. Without their support none of this would have been possible.
To my brother Davide with whom we encouraged each other during this difficult year. A heartfelt thanks goes to my brother Daniel, that, despite the kilometric distance that separates us, has always been near me. To Alessandro, who always provides a refreshing break from the monotony of running calculations and to Daniela, to try to give another point of view and insights.
I would like to thank Michela, the sister I never had, thank you so much for everything, for always being there.

And finally and most importantly, to Cristiano, thank you for all the understanding and guidance, for putting up with me during the many times I complain, for encouraging me to start this adventure and for sticking with me, always. Henri Matisse said *"Il y a des fleurs partout pour qui veut bien les voir"* (There are always flowers for those who want to see them). Thank you for helping me to understand it.

Abstract

Human activity is overloading our atmosphere with carbon dioxide and other global warming emissions with immense risks to our climate. Green energy harvesting are needed to supply electricity from one or different energy sources present in the environment. One of this sources is thermal energy through the phenomenon called thermoelectricity. The thermoelectric energy harvesting technology exploits the conversion of temperature gradient into electric power. The significant request for thermoelectric energy harvesting is justified by developing new thermoelectric materials and the design of new thermoelectric generator (TEG) devices for many different applications. The fundamental problem in creating efficient thermoelectric materials is that they need to be good at conducting electricity, but not at conducting thermal energy. But in most materials, electrical and thermal conductivity go hand in hand.

The aim of this thesis is to describe the methods and results in the field of thermoelectricity. I report a theoretical study of electronic properties, transport coefficients and lattice thermal conductivity for promising thermoelctric materials. The theoretical approach to thermoelectricity is unusually complex as it tackles transport in the two distinct subsystems of electrons and phonons. The calculations are rather difficult and use multifarious methods, each with its peculiar problems and pitfalls. In general, there are ab initio electronic bands calculations, rigid-band Boltzmann-equation calculations of electronic transport including various scattering mechanisms, ab initio or model calculations of phonon transport under several scattering (which in turn involve phonon calculations etc.). Comfortingly, the final product is the ZT figure of merit, a blend of the various ingredients that is relatively insensitive to the fine details.

Chapter 1 provides context on the importance of thermoelectricity, the basics of this phenomenon and ways proposed in the literature to improve it. Chapter 2 reports the background of density functional theory used for our calculations while Chapter 3 is about transport phenomena in the Boltzmann Transport Equation framework. Chapter 4 reports the methods and results about the β-phase of Mg_3Sb_2. Then in Chapter 5, a study of layered perovskite $La_2Ti_2O_7$ is presented, and finally, in Chapter 6, a new promising material, the orthorhombic phase of LaSO is studied. The last part contains the conclusion remarks.

List of papers

- *Ab initio* thermal conductivity of thermoelectric Mg_3Sb_2: Evidence for dominant extrinsic effects, M.B. Maccioni, **R. Farris**, V. Fiorentini; *Physical Review B* **98** (22), 220301 (2018)
- Theory of thermoelectricity in Mg_3Sb_2 with an energy-and temperature-dependent relaxation time, **R. Farris**, M.B. Maccioni, A. Filippetti, V. Fiorentini; *Journal of Physics: Condensed Matter* **31** (6), 065702 (2018)
- Influence of thermal conductivity and of non-constant relaxation time on thermoelectricity in Mg_3Sb_2, **R. Farris**, M.B. Maccioni, A. Filippetti, V. Fiorentini; *Journal of Physics: Conference Series* **1226** (1), 012010 (2019)
- High thermoelectric figure of merit and thermopower in layered perovskite oxides, V. Fiorentini, **R. Farris**, E. Argiolas, M.B. Maccioni; *Physical Review Materials* **3** (2), 022401 (2019)
- Giant thermoelectric figure of merit in multivalley high-complexity-factor LaSO, **R. Farris**, F. Ricci, G. Casu, G. Hautier, G.-M. Rignanese, V. Fiorentini; Manuscript submitted for publication. (2020)

Table of contents

List of figures

List of tables

Chapter 1

Introduction

1.1 Thermoelectric Phenomena: Background and Applications

Thermoelectricity is the direct conversion of heat into electrical energy. Thermoelectric systems are solid-state devices that either convert heat directly into electricity or transform electric power into thermal power for heating or cooling. Such devices are based on thermoelectric effects involving interactions between the flow of heat and electricity through solid bodies. These phenomena, called **Seebeck effect** and **Peltier effect** (and **Thomson effect** as an extension created by Lord Kelvin), can be used to generate electric power and heating or cooling. More specifically, the Seebeck effect is the build up of an electric potential across a temperature gradient, the Peltier Effect is the presence of heating or cooling at an electrified junction of two different conductors, and finally the Thomson effect is the presence of cooling when electric current passes through a circuit composed of a single material (this is the biggest difference with the Peltier Effect) when a temperature gradient is applied along its length. We will look into this matter in the next paragraph.

Over the past decades, there has been heightened interest in the field of thermoelectrics, driven by the need of more efficient materials for electronic refrigeration and power generation [1]. This solid-state technology has long been used for powering the spacecrafts of several NASA deep-space missions [2]: when a spacecraft is too far from the Sun or on the dark side of the Planet, it does not have access to photovoltaic and the only access to energy needs to be some other source; Radioisotope Thermoelectric Generators (RTGs) provide electricity using heat from the natural radioactive decay of PU-238, in the form of plutonium dioxide. The difference in temperature between this hot fuel and the cold environment of space is applied across p-n junctions of silicon-germanium generating a voltage [3]. This process worked for 30 years without a single failure.

Although thermoelectrics have limited commercial use in niche applications, these are growing due to interest in waste-heat recovery and increasing global energy efficiency reducing our dependence on fossil fuels. Proposed industrial and military applications of thermoelectric materials are generating increased activity in this field by demanding higher performance high temperature TE materials than those that are currently in use. Thus, the development of higher-performance TE materials is

becoming ever more important. Power-generation applications are currently being investigated by the automotive industry (ATEGs - automotive thermoelectric generators) as a means to develop electrical power from waste engine heat from the radiator and exhaust systems for use in next-generation vehicles. Indeed, it is estimated that roughly 75% of the energy produced during combustion is lost in the form of heat [4], this heat is wasted unless it can be used for other applications, such as to charge the battery instead of using an alternator. By converting the lost heat into electricity, ATEGs lead to a less fuel consumption by reducing the electric generator load on the engine. Since the electricity is generated from waste heat that would otherwise be released into the environment, the engine burns less fuel to power electrical components. In ATEGs, thermoelectric materials are packed between the hot-side and the cold-side heat exchangers (metal plates with high thermal conductivity).The temperature difference between the two surfaces of the thermoelectric modules (several hundred degrees) generates electricity using the Seebeck Effect.
In addition,TE refrigeration applications include seat coolers for comfort and electronic component cooling by exploiting the Peltier effect. In these cases, Peltier effect is used to create a heat pump which transfers heat from one side of the device to the other, consuming electrical energy, It can be used either for heating or for cooling or as a temperature controller that either heats or cools. This effect is commonly used for cooling electronic components and small instruments

1.1.1 Advantages and disadvantages of Thermoelectrics

Thermoelectric devices are solid-state devices without moving parts, noise or vibrations, ensuring increased reliability and long life. In addition, they are thermoelectric cooling and thermoelectric power generation is very scalable from less than one watt of cooling power or power generation up to kilowatts. In the cooling process, since the temperature of a thermoelectric cooler is dependent on the current provided to it, there is a precise temperature control and below ambient temperatures can be achieved.
Its main disadvantages are high cost for a given cooling capacity (in Peltier devices) and poor power efficiency. Many researchers and companies are trying to develop thermoelectrics that are cheap and more efficient.

1.2 The thermoelectric effects

1.2.1 Seebeck and Peltier effects

In the early 1800s, Seebeck observed that when two dissimilar materials are joined together and the junctions are held at different temperatures (T and T+ΔT), a voltage difference (ΔV) develops. This voltage is proportional to the temperature difference (ΔT) [5]. The ratio of the voltage developed to the temperature gradient (ΔV/ΔT) is related to an intrinsic property of the materials called the *Seebeck coefficient* **S** (Equation 1.1). More in detail, consider a finite rod of a conducting material heated only

on one end. Due to temperature gradient the charge carriers (either electrons, or places where an electron is missing, known as "holes") are forced to move from the heated side to the cooler side. If a temperature gradient exists in a junction of two dissimilar conductors, a voltage is produced: that is the definition of thermocouple. The voltage generated depends on Seebeck coefficient and on temperature gradient between the two parts on the thermocouple (Fig 1.1).

$$S = \frac{\Delta V}{\Delta T} \tag{1.1}$$

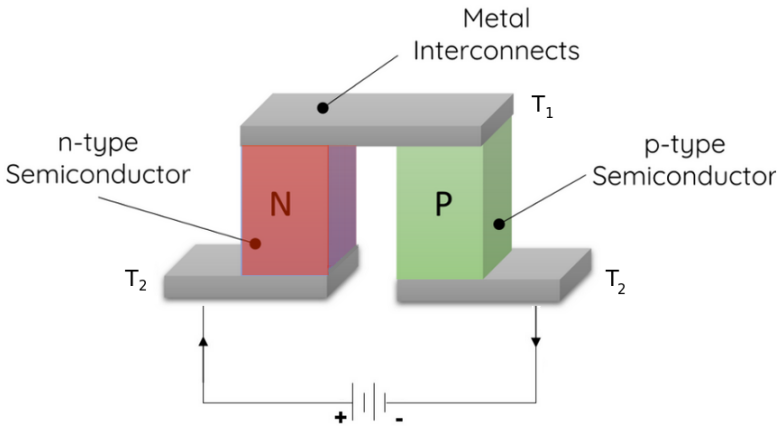

Fig. 1.1 A functioning thermocouple requires a p-type/n-type pair (acceptor/donor). The sign of the Seebeck coefficient is determined by the direction of current flow. If T_2 is greater than T_1 and the current is flowing clockwise, then the Seebeck coefficient is positive, and if the current is counter-clockwise it is negative. The Seebeck coefficient is very low for metals (only a few μV/K) and much larger for semiconductors (typically a few hundred μV/K).

A p-type/n-type module allows for an exchange between electrons and holes or holes and electrons at the junctions J_1 and J_2, completing the circuit and allowing for either power generation or refrigeration. Thermoelectric devices contain many thermoelectric couples connected electrically in series and thermally in parallel (Fig. 1.2).

A related effect was discovered a few years later by Peltier, in which, when an electrical current is passed through the junction of two dissimilar materials, heat is either absorbed or rejected at the junction, depending on the direction of the current. This effect is due largely to the difference in Fermi energies of the two materials, i.e. the highest occupied energy level of a material at zero Kelvin: in n-type semiconductors, Fermi energy is close to the conduction band while p-type semiconductors have Fermi energies close to the valence band. Peltier coefficients represent how much heat is carried per unit charge: electrons can transfer heat in two ways: through collisions with other electrons, or by carrying internal kinetic energy during transport; the second way is the Peltier effect. We can say that if the Seebeck effect describes how a temperature difference creates electrical current, the Peltier effect describes how an electrical current can create a heat flow. These two effects are related to each

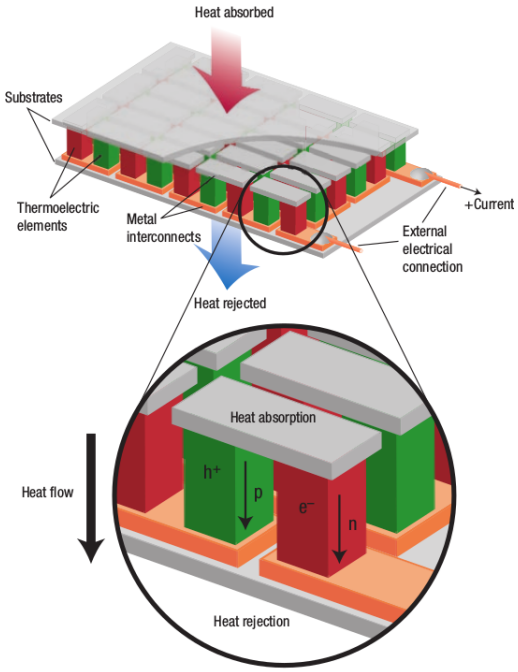

Fig. 1.2 Thermoelectric module showing the direction of charge flow on both cooling and power generation. Original Figure on [6].

other, as shown in the definition of the Peltier coefficient:

$$\Pi = \mathbf{S}T$$

Lord Kelvin discovered later a third effect: an electric current is passed through a homogeneous circuit in the presence of a temperature gradient. This is now called the Thomson effect and it has the smallest magnitude among the thermoelectric effects.
These effects, which are generally quite inefficient, began to be developed into practical products, such as power generators for spacecraft, in the 1960s.

1.3 Figure of Merit and Thermoelectric Performance

The potential of a TE material and the efficiency of a thrermoelectric device are determined in large part by a measure of the material's figure of merit ZT which is simply a particular combination of transport coefficents:

$$ZT = \frac{S^2\sigma T}{\kappa} = \frac{S^2\sigma T}{\kappa_\ell + \kappa_e} \tag{1.2}$$

where S is the Seebeck coefficient, σ is the electrical conductivity, and κ is the total thermal conductivity (κ_ℓ and κ_e, the lattice and electronic contributions, respectively). The higher the material fiugre of merit is, the higher the performance of the device. The figure of merit is linked to the

maximum efficiency of the device by:

$$\eta_{max} = \frac{T_H - T_C}{T_H} \frac{\sqrt{1+ZT^{av}} - 1}{\sqrt{1+ZT^{av}} + \frac{T_C}{T_H}} \tag{1.3}$$

Where T_C and T_H are the cold and the hot temperature respectively, while the average temperature T^{av} is given by $\frac{T_H + T_C}{2}$.
Since thermoelectric devices are heat engines, their efficiency is limited by the Carnot efficiency $\frac{T_H - T_C}{T_H}$ and by the value of ZT (Fig 1.3).
The best TE materials currently used in devices have ZT ≈ 1. This value has been a practical upper

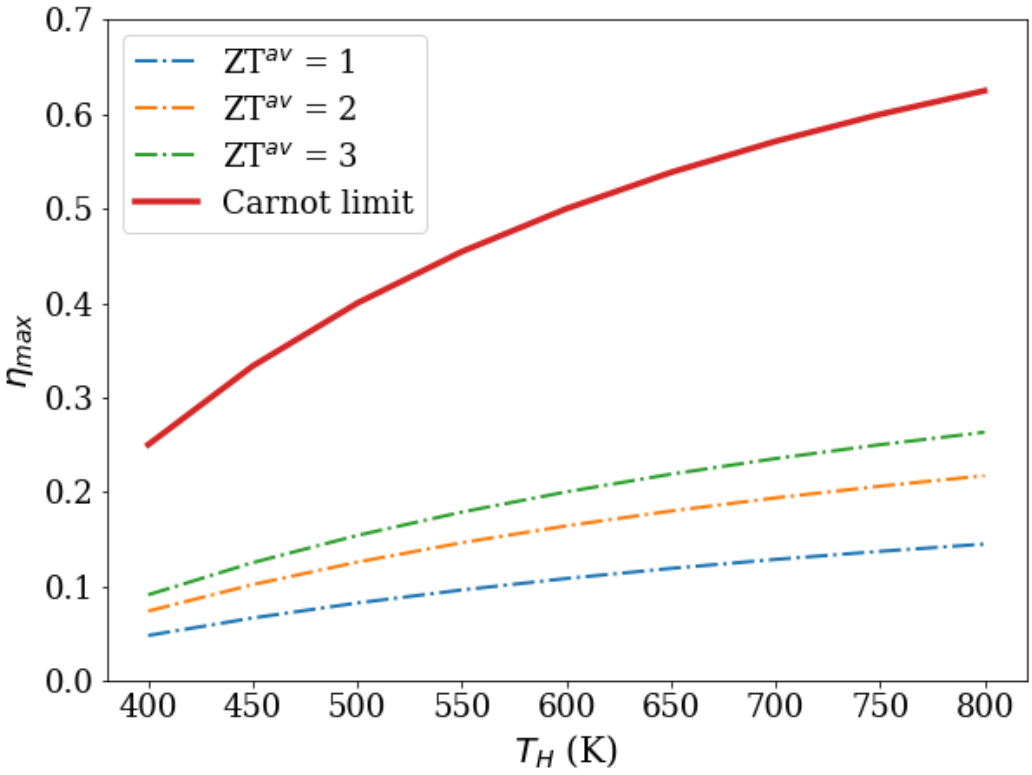

Fig. 1.3 Maximum efficiency of a thermocouple in function of hot temperature T_H when T_C is kept at 300 K and ZT is treated as a constant, the red curve represents the maximum efficiency for a heat engine according to Carnot's theorem.

limit for more than 30 years, yet there are no theoretical or thermodynamic reasons for that value as an upper barrier [6]. If the ZT could be increased to 3 or 4, the potential applications would dramatically increase [1].

[1] Going on to the practical aspect, the ZT for a single material is somewhat meaningless, since an array of TE couples is utilized in a device or module.

1.3.1 Optimize thermoelectric properties

A detailed derivation of thermoelectric parameters is discussed in Chapter 3. Here we limit to report the essential elements for the discussion.
Considering parabolic bands and an energy-independent scattering approximation [7], the expression for Seebeck coefficient S is:

$$S = \frac{8\pi^2 k_B^2}{3eh^2} m^* T \left(\frac{\pi}{3n}\right)^{2/3} \tag{1.4}$$

Where m^* is the effective mass of the carrier and n is the carrier concentration, while the basic expression for electrical conductivity is

$$\sigma = ne\mu \tag{1.5}$$

with μ the carrier mobility.
To ensure that Seebeck coefficient is large, one should have low carrier concentration insulators or semiconductors but this leads to low electrical conductivity. Therefore we say that maximize ZT means make a trade-off between conflicting properties. The peak of ZT typically occurs at carrier concentrations between 10^{19} and 10^{21} carriers per cm^3 depending on the material system. In particular figure 1.4 refers to Bi_2Ti_3, one of the best thermoelectrics. We might get an idea of the value power factor ($S^2\sigma$) we should have by considering a total thermal conductivity of about 1 (W/mK) typical of low thermal conductivity good thermoelectric materials and a desirable ZT of at least 1. At 300 K, it is needed a power factor of 3.3 (mW/mK^2). By looking at some well characterized materials (not necessarily good thermoelectrics), we found Silicon with a peak of 2 (mW/mK^2) [8], considerably less than Bi_2Ti_3 with a peak in power factor of 4 (mW/mK^2) [9]. The power factor($S^2\sigma$), is typically optimized in narrow-gap semiconducting materials as a function of carrier concentration (typically 10^{19} carriers/cm^3), through doping, to give the largest ZT [10]. High-mobility carriers are most desirable, in order to have the highest electrical conductivity for a given carrier concentration. At the same time , total thermal conductivity needs to be as small as possible to increase ZT.
A key factor in developing these technologies is the development of higher-performance TE materials, either completely new materials or through more ingenious materials engineering of existing materials. Some of the research efforts focus on minimizing the lattice thermal conductivity as we will see in the next section, while other efforts focus on materials that exhibit large power factors. This latter point will be our main focus on Chapter 6.

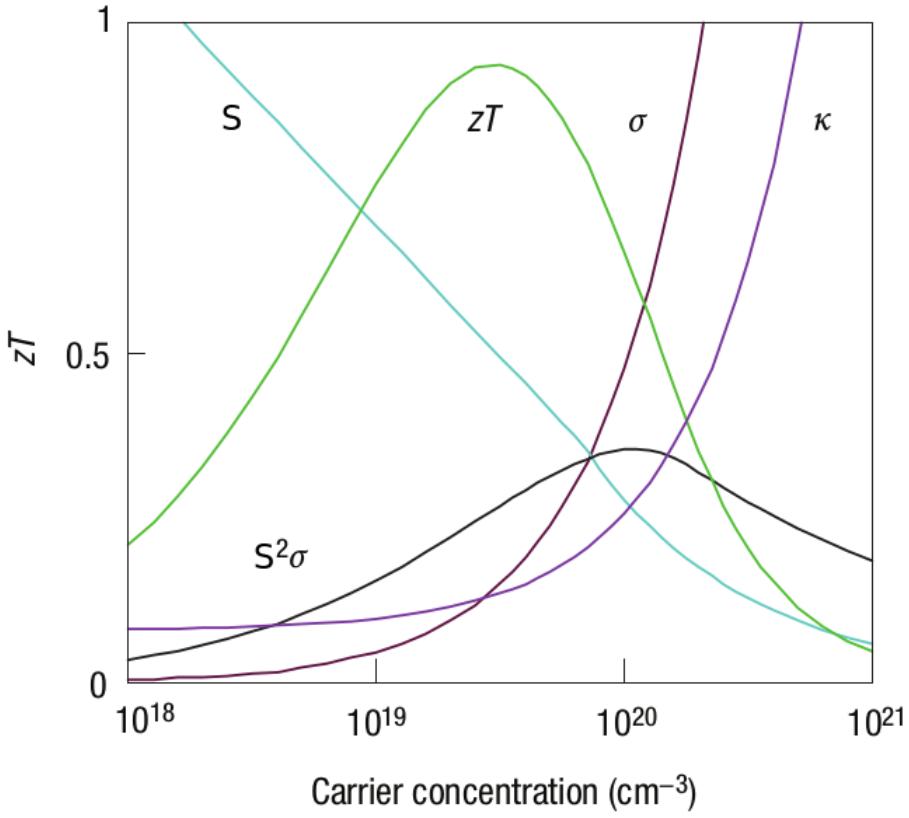

Fig. 1.4 Constituents of the Thermoelectric Figure-of-Merit, ZT. In this figure S is the Seebeck coefficient plotted from 0 to 500 μV K^{-1}, σ is the electrical conductivity plotted from 0 to 5000 Ω^{-1} cm^{-1} , κ is the electrical contribution to the thermal conductivity plotted from 0 to a top value of 10 W m$-$1 K^{-1}, $S^2\sigma$ is the power factor, and ZT is the thermoelectric figure-of-merit. Trends shown for Bi_2Ti_3. Published in Nature (see [6]).

1.3.2 Nanostructuring

Thermoelectrics require a rather unusual material: a *phonon-glass electron-crystal* [11] The electron-crystal behavior is needed because crystalline semiconductors possess the required electronic properties that are Seebeck coefficient, electrical conductivity and electronic thermal conductivity. The phonon-glass is needed in order to have a lattice thermal conductivity as low as possible. The minimization of lattice thermal conductivity can come through solid solution alloying with isoelectronic elements to preserve a crystalline electronic structure while creating large structural anisotropy to disrupt the phonon path (for example SiGe alloys). Recently, another approach in this field is the nanostructuring. Indeed, one of the development of the past couple of decades has been the artificially structurization at the nanoscale to engineer the lattice thermal conductivity and reduce it from the value that it would normally have. This can be done, for instance, by introducing an high density of grain boundaries and other scattering centers that scatter phonons but non effective in scattering electrons(Fig. 1.5). Reduced thermal conductivity in thin-film superlattices was investigated in the

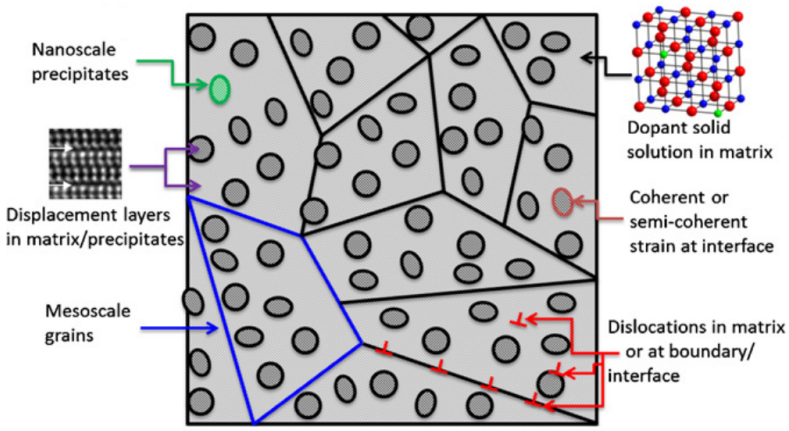

Fig. 1.5 Schematic illustration of all length-scale structures for high performance TE systems where major contributing factors for reducing the lattice thermal conductivity are indicated [12]

1980s, but has only recently been applied to enhanced thermoelectric materials. This idea represented a significant advancement in thermoelectric performance (Fig 1.6).

1.3.3 Calculation methodology

The intention of this study is to calculate the thermoelectric properties of materials with *ab initio* methods.
The methodology for this study is split into two major steps:

1) A density functional theory (DFT) calculation (A detailed explanation of the density functional theory is reported in Chapter 2), to find both the minimum energy structure and the ground-state electronic structure.

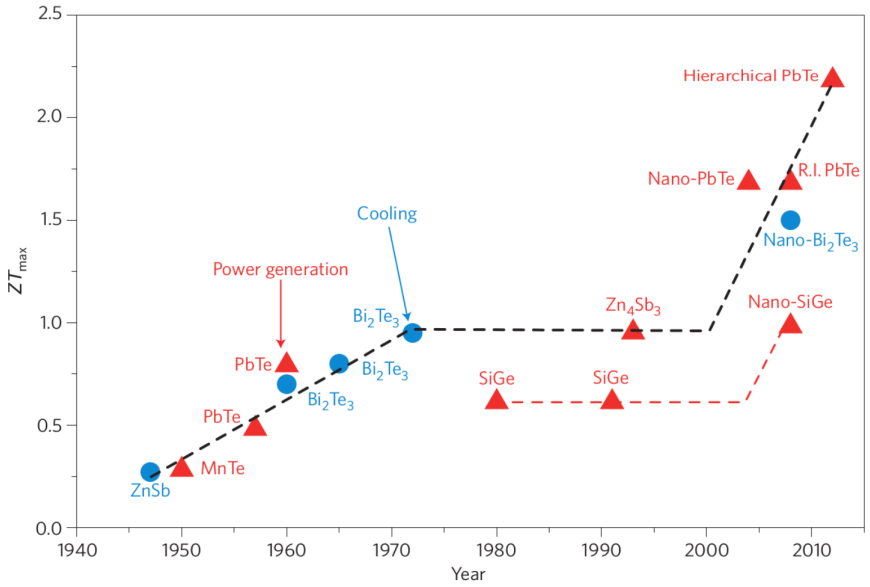

Fig. 1.6 Materials for thermoelectric cooling are shown as blue dots and for thermoelectric power generation as red triangles. After 1970 there was a period of time when almost no progress occured. When the idea of using nanostructuring to enhance TE performance was introduced, there was an important advance in them. References for the ZT of nanoscale thermoelectric materials can be found in the original graph [13]

2) The application of the Boltzmann transport theory (presented in Chapter 3), by using data from a density functional theory calculation to determine the thermoelectric properties

With this approach we computed thermoelectric properties for different materials. In Chapter 4 we will present the main results for the hexagonal Zintl phase of Mg_3Sb_2 while in Chapter 5 the Layered-structural monoclinic-orthorhombic perovskite $La_2Ti_2O_7$. Chapter 6 is devoted to the High-Throughput database search method and the results following this line of research about a orthorhombic phase of LaSO. Chapter 7 contains the conclusion remarks.

Chapter 2

Computational methods

2.1 Density Functional Theory

Density functional theory is nowadays the primary tool for the calculation of electronic structure in condensed matter and is increasingly important in quantitative studies of molecules and other finite systems. The first formulation of density functional theory has been made by Hohenberg and Kohn in a famous paper written in 1964. In this paper they showed that all properties of a quantum many-body system can be considered to be universal functional of the ground state density (n_0) [14]. The next year Kohn and Sham completed the theory with an *ansatz*: to replace the original many-body problem with a problem of non-interacting particles introducing an exchange-correlation functional which contains all the many-body terms [15]. In this chapter will be explained, in broad terms, the general principles behind this theory.

2.1.1 Theoretical background

A physical problem can be described by the solution of the Schödinger equation.

$$i\hbar\frac{\partial\Psi(\mathbf{r},\mathbf{R};t)}{\partial t} = \hat{H}\Psi(\mathbf{r},\mathbf{R};t) \tag{2.1}$$

Where the wavefunctions $\Psi(\mathbf{r},\mathbf{R})$ depends on electronic positions $\mathbf{r}$ and nuclei positions $\mathbf{R}$, $\hat{H}$ is the Hamiltonian of the system:

$$\begin{aligned}\hat{H} = -\frac{\hbar^2}{2m_e}\sum_i \nabla_i^2 - \sum_{i,I}\frac{Z_I e^2}{|r_i - R_I|} + \frac{1}{2}\sum_{i\neq j}\frac{e^2}{|r_i - r_j|} \\ -\frac{\hbar^2}{2M_I}\sum_i \nabla_i^2 + \frac{1}{2}\sum_{I\neq J}\frac{Z_I Z_J e^2}{|R_I - R_J|}\end{aligned} \tag{2.2}$$

where lower case letters indicate electrons and upper case letters indicate nuclei [16]. The stationary equation can be written as:

$$\hat{H}\,|\Psi\rangle = E\,|\Psi\rangle \tag{2.3}$$

The first approximation to solve the many-body system is the *adiabatic approximation* of Born and Oppenheimer (1927) for which it can be possible to neglect the ionic contribution at kinetic energy due to the large ionic masses compared with electronic masses. This is a good approximation for many purposes, e.g. the calculation of nuclei vibration modes in solids and also it is the starting point for the perturbation theroy in electron-phonon interactions.
By using the Born- Oppenheimer approximation, the Hamiltonian which acts onto the electronic variables and depends parametrically upon R can be written as:

$$\hat{H} = -\frac{\hbar^2}{2m_e}\sum_i \nabla_i^2 + \frac{1}{2}\sum_{i\neq j}\frac{e^2}{|r_i - r_j|} + \sum_{i,I}\frac{Z_I e^2}{|r_i - R_I|} + E_N(R) \tag{2.4}$$

Or implicitly:

$$\hat{H} = T_e + V_{ext} + V_{int} + E_N \tag{2.5}$$

T_e is the kinetic energy of electrons, V_{ext} the potential energy of electrons due to their interaction with ions, V_{int} is the potential energy due to electron-electron interactions and $E_N(R)$ is the classical electrostatic energy between different nuclei that doesn't concern the electronic problem.
As it has been anticipated, the density of particles plays a central role in electronic structure theory, and in view of quantum mechanics, it can be written as the expectation value of density operator $\hat{n}(\mathbf{r}) = \sum_{i=1,N}\delta(\mathbf{r}-\mathbf{r}_i)$:

$$n(\mathbf{r}) = \frac{\langle\Psi|\,\hat{n}(\mathbf{r})\,|\Psi\rangle}{\langle\Psi\,|\,\Psi\rangle} \tag{2.6}$$

The same applies to the total energy, which is the expectation value of the hamiltonian:

$$E = \frac{\langle\Psi|\,\hat{H}\,|\Psi\rangle}{\langle\Psi\,|\,\Psi\rangle} \tag{2.7}$$

2.1.2 Hohenberg-Kohn theorems

The Hohenberg-Kohn theory starts considering the system of interacting particles in an external potential V_{ext}. This theory is based on two theorems:

1. V_{ext}(r) is a unique functional of n_0(r), apart from a trivial additive constant.

2. $E[n]$ is a universal functional for the energy, valid for any number of particles and any external potential. For a given V_{ext}(r) the global minimum of this functional represents the ground state energy of the system and the density $n(r)$ that minimizes this functional is the exact ground state energy $n_0(r)$

According to these theorems, no two different potentials acting on the electrons of a given system can give rise to a same ground-state electronic charge density. This property can be used in conjunction with the standard Rayleigh- Ritz variational principle of quantum mechanics to show that a universal functional $F[n(\mathbf{r})]$ of the electron charge density exists such that the functional is minimized by the electron charge density of the ground state corresponding to the external potential $V_{ext}(\mathbf{r})$, under the constraint that the integral of n($\mathbf{r}$) equals the total fixed number of electrons.

$$E[n(\mathbf{r})] = F[n(\mathbf{r})] + \int n(\mathbf{r}) V_{ext}(\mathbf{r}) d\mathbf{r} \tag{2.8}$$

Furthermore, the value of the minimum coincides with the ground-state energy. From the first theorem:

$$\left\langle \hat{H} \right\rangle = \left\langle \hat{T}_e \right\rangle + \left\langle \hat{V}_{int} \right\rangle + \int d^3\mathbf{r} \; V_{ext}(\mathbf{r}) n(\mathbf{r}) + \left\langle \hat{E}_N \right\rangle \tag{2.9}$$

The classical term with the nuclear-nuclear interactions can be also included on the external potential. Unfortunately, Hohenberg-Kohn theory does not tell how to construct this functional and this is the reason why so much effort has been dedicated to the task of obtaining approximate functionals for the description of the ground-state properties of many-particle systems. This ignorance can be handled considering, in agreement with Kohn and Sham ansatz, an auxiliary non-interacting particle system. This leads to soluble independent equations with all the terms unknown incorporated into an exchange-correlation functional of the density (a reminiscence from the Hartree-Fock theory) [16]. In this approach the Hohenberg-Kohn ground-state energy can be written as:

$$E_{KS} = T_e[n] + \int n(\mathbf{r}) V_{ext}(\mathbf{r}) d(\mathbf{r}) + E_{Hartee}[n] + E_N + E_{xc}[n] \tag{2.10}$$

In which the Hartree term takes into account the classical Coulomb interaction energy of the electron density interacting with itself and the kinetic independent contribution is given directly as a functional of orbitals. Variation of the energy functional with respect to *n(r)* with the constraint that the number of electrons be kept fixed leads formally to the same equation as would hold for a system of noninteracting electrons subject to an effective potential.

$$V_{KS}(\mathbf{r}) = V_{ext}(\mathbf{r}) + V_{Hartree}(\mathbf{r}) + V_{xc}(\mathbf{r}) \tag{2.11}$$

with the Kohn-Sham Hamiltonian given by:

$$H_{KS}(\mathbf{r}) = -\frac{1}{2}\nabla^2 + V_{KS}(\mathbf{r}) \tag{2.12}$$

These equations have the form of independent-particle equations with a potential found self-consistently with the resulting density. Solving separately the kinetic energy and the Hartree contributions, the

exchange and correlation contribution can be approximated with a local functional of the density:

$$E_{xc}(\mathbf{r}) = \int n(\mathbf{r})\varepsilon_{xc}(\mathbf{r})d\mathbf{r} \tag{2.13}$$

with ε_{xc} the energy contribution per electron.

2.1.3 Functional for exchange and correlation

The exchange correlation energy can be approximated with a functional of the density. The most widely used approximations for the exchange and correlation potential are:

- Local Density Approximation (LDA)
- Generalized Gradient Approximation (GGA)
- Hybid functionals

LDA

The exchange and correlation energy is an integral over all space with the energy density at each point the same as a homogeneous electron gas with that density. The LDA is exact in the limit of high density or of a slowly varying charge-density distribution([15]). On the other hand LDA overestimates binding energies producing a bad description of some kind of materials.

GGA

This approximation is the step beyond LDA. Indeed in this case the functional depends not only on density, but also on the magnitude of its gradient ($|\nabla n|$) and higher order derivatives.

$$E_{xc}^{GGA} = \int n(\mathbf{r})\varepsilon_{xc}[n, \nabla n, \nabla^2 n, ...]d\mathbf{r} \tag{2.14}$$

In this case not only there is a correction for the LDA overbinding, but generally this approximation improves agreement with experiments. The most popular functionals of this type are those of Perdew, Burke and Ernzerhof (PBE) [17] and Perdew and Wang [18]. Generally, the GGA Functionals give total energies of atoms and cohesive energies of solids that are closer to experiment than the LDA results [19]. However GGA sometimes overcorrects LDA results in ionic crystals where the lattice constants from LDA calculations fit well with experimental data but GGA will overestimate it. Nevertheless, both LDA and GGA perform badly in materials where the electrons tend to be localized and strongly correlated such as transition metal oxides and rare-earth elements and compounds. This weakness leads to go beyond these approximations.

Hybrid functionals

Hybrid functionals were introduced since the beginning of the nineties and are mainly used in quantum chemistry calculations. These functionals solve problems related to the local density approximation and generalized gradient approximation by adding explicitly a fraction of the real exchange energy which can be obtained by Hartree-Fock methods. As a result they take into account non-local effects of the exchange energy and are the most accurate functionals if we consider energetics [16].

2.1.4 Solving Kohn-Sham Equations

By using independent-particle methods, the KS equations provide a way to obtain the exact density and energy of the ground state of a condensed matter system. The KS equations must be solved consistently because the effective Kohn-Sham potentials V_{KS} and the electron density $n(r)$ are related to each other. This can be done numerically with a self-consistent scheme as shown in the flow chart 2.1.

The concept of self-consistency has been prevalent across many fields of physics. At the beginning of the process an electron density is required n^{in} to compute the Hartree and exchange-correlation potentials. Then, the effective KS potential V_{KS} is calculated and the KS equation is solved with single-particle eigenvalues and wavefunctions and a new electron density n^{out} is then calculated from the wavefunctions [20]. After this, self-consistent condition(s) is checked. For a given external potential and exchange-correlation functional, the density is self-consistent when $n^{\text{in}} = n^{\text{out}}$. To put it in the words of Hartree [21] : *"If the final field is the same as the initial field, the field will be called self-consistent"*. If the self-consistency is not achieved,the calculated electron density will be mixed with electron density from previous iterations to get a new electron density. A new iteration will start with the new electron density. This process continues until self-consistency is reached. After the self-consistency is reached, several quantities can be calculated including total energy, forces, stress, eigenvalues, electron density of states, band structure, etc.. The most timing consuming step in the whole process is to solve KS equation with a given KS potential V_{KS}. Modern computational implementations of Kohn-Sham theory can vary significantly due to the choice of basis set, which leads to the related problem of whether one treats all the electrons in the computation explicitly, or treats core electrons with a pseudopotential.

2.1.5 Pseudopotentials

Pseudopotentials are generated in atomic calculations and used to reproduce properties of valence electrons in molecules and solids. To solve electronic structure in solids, it can be used the so called plane wave pseudo potential method. This method adopts a complete set of plane waves ($e^{i\mathbf{k}\cdot\mathbf{r}}$) to describe non-interacting electronic orbitals moving in a local field which takes into account electron-electron interactions and the external potential of nuclei are replaced by pseudopotentials which

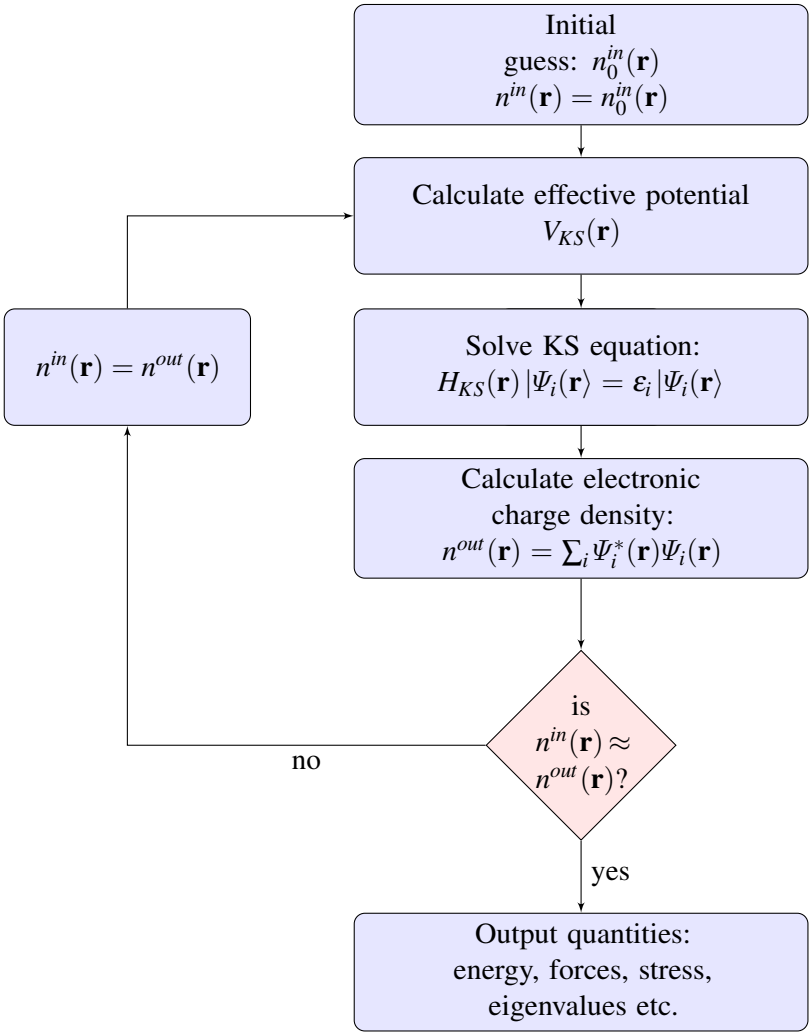

Fig. 2.1 Flowchart of self-consistency loop for solving KS equations. At the beginning an electron density is required n^{in}. Then the effective KS potential V_{KS} is calculated and the KS equation is solved with single-particle eigenvalues and wavefunction and a new electron density n^{out} is calculated from the wavefunctions. For given V_{ext} and V_{xc} , the $n(\mathbf{r})$ is self-consistent when $n^{\text{in}} = n^{\text{out}}$. If the self-consistency is not achieved, the calculated electron density will be mixed with electron density from previous iterations to get a new electron density. A new iteration will start with the new electron density. This process continues until self-consistency is reached.

include effects from core electrons.
There are two desirable characteristics for Pseudopotentials:

1. *Transferability*: modern pseudopotentials are constructed on the isolated atom. Transferability can be estimated by computing eigenvalues from atomic calculations on different configurations.

2. *Softness*: atoms with strongly oscillating pseudo-wavefunctions (first-row elements, elements with 3d and 4f valence electrons) will require many plane waves in calculations. Larger core radius means better softness but worse transferability.

It is convinient to distinguish between *norm-conserving* (NCPP) and *ultrasoft* (USPP) pseudopotentials. For the first type, the key is to create pseudopotentials which are accurate and trasferible from an environment to another (for example they should describe the valence properties of an atom in ions and condensed matter). Norm-conserving pseudopotentials are constructed to enforce two conditions [22]:

1. Inside the chosen cut-off radius r_c, the norm of each pseudo-wavefunction should be identical to its corresponding all-electron wavefunction:

$$\int_{r<r_c} dr^3 \Psi_{\mathbf{R},i}(\vec{r})\Psi_{\mathbf{R},j}(\vec{r}) = \int_{r<r_c} dr^3 \tilde{\Psi}_{\mathbf{R},i}(\vec{r})\tilde{\Psi}_{\mathbf{R},j}(\vec{r})$$

Where $\Psi_{\mathbf{R},i}$ and $\tilde{\Psi}_{\mathbf{R},i}$ are the all-electron and pseudo reference states for the pseudopotential on atom $\mathbf{R}$.

2. All-electron and pseudo wavefunctions are identical for $r > r_c$

NCPPs require a large plane-wave basis sets ($E_c > 70Ry$) for first-row elements (in particular N, O, F) and for transition metals (Cr, Mn, Fe, Co, Ni, ...) and that means large computational cost.
To reduce CPU and RAM requirements, USPPs have been introduced: considering auxiliary localized functions, it is possible to define ultrasoft potentials as the sum of a smooth part and a rapidly varying function localized around each ion core, improving the accuracy of norm-conserving pseudopotential and at the same time making the calculation less costly because norm-conservation condition is not required and this significantly reduces the number of plane waves needed to expand the wavefunctions (the computational cost scales as a power of the number of Fourier components needed to complete the calculation). Plane waves calculations are generalized to projector augmented wave (PAW) method. The PAW formalism is strongly linked to ultrasoft pseudopotentials [23] and it was first proposed and implemented by Blöchl [24]. Basically, in the PAW method, the one electron wavefunctions Ψ_n are derived from the pseudo orbitals $\widetilde{\Psi}_n$ in a linear transformation:

$$\Psi_n = \mathscr{T}\widetilde{\Psi}_n.$$

How to define the operator $\mathscr{T}$?

- define a complete set of initial and final states for the transformation :
  $\forall i \qquad |\phi_i\rangle = \mathscr{T}\,|\tilde{\phi}_i\rangle$

- Final states: All-electron valence partial waves: $|\phi_i\rangle$
- Initial states: Auxiliary partial waves $|\tilde{\phi}_i\rangle$
  True and auxiliary wave function are identical outsides the augmentation radius r_c $\phi_i(\vec{r}) = \widetilde{\phi}_i(\vec{r}) \quad |\vec{r}-\vec{R}| < r_c$

$$\mathscr{T} = 1 + \sum_j (|\phi_j\rangle - |\tilde{\phi}_j\rangle) \langle \tilde{p}_j|$$

With $\langle \tilde{p}_j|$ the Projector function localized in the augumentation region and it must obey the orthogonality condition: $\langle \tilde{p}_i|\tilde{\phi}_j\rangle = \delta_{i,j}$.
By using this transformation, the all-electrons wave function is:

$$|\Psi_n\rangle = |\tilde{\Psi}_n\rangle + \sum_j (|\phi_j\rangle - |\tilde{\phi}_j\rangle) \langle \tilde{p}_j|\tilde{\Psi}_n\rangle$$

The most widely used codes with plane waves and pseudopotentials are ABINIT [25], VASP [26] and Quantum ESPRESSO [27] [28].

2.2 Phonons

In any solid crystal, atoms are bound into a specific periodic three-dimensional lattice. One could imagine that, because of an external force or their own thermal energies, atoms vibrate as a system of tiny springs connected to each other. This generates mechanical waves that carry energy in form of heat and sound through the lattice. A packet of these waves can travel throughout the crystal with a definite energy and momentum, so in quantum mechanical terms the waves can be treated as a particle and in condensed matter Physics this quantum of vibrational mechanical energy is called a *phonon*.
The term *phonons* comes from the Greek $\phi\omega\nu\eta$ which translates to sound since phonons give rise to sound. The name stresses the analogy with photons (minute energy packet of electromagnetic radiation).
Phonon calculation is the starting point to obtain lattice dynamical properties as we will see in the next paragraph.

2.2.1 Linear response and density functional perturbation theory

Density Functional Perturbation Theory (DFPT) is widely used to predict the linear response (and related physical quantities) of periodic systems when they are submitted to an external perturbation [31] [32]. Some perturbations can be for example atomic displacements (phonons), dilatation and contraction of the primitive cell, homogeneous external field. In solid state physics, there are many properties associated with derivatives of the total energy with respect to the "atomic displacement" and "homogeneous electric field" perturbations. Examples of first order derivative is the force exerted

on nuclei, stresses and dipole moments.
Physical properties connected with second derivatives of total energy are often referred to as linear-response coefficients. The first-order Hamiltonian and the polarizability tensor are indeed second-order derivatives of the energy. The description of the molecular vibrations, in the harmonic approximation, is based on the knowledge of the "interatomic force constants", second derivatives of the total energy with respect to the change of nuclei positions, describing the forces that appear when a nucleus is displaced from its equilibrium position, in the linear regime. Going to the nonlinear regime, one has higher-order derivatives, such as the nonlinear dielectric tensor and anharmonic force constants (phonon - phonon interaction, Grüneisen parameters).
In this method, it is essential to calculate the second-order perturbation of DFT total energy, i.e. $\delta^2 E$, in the framework of density functional theory.
Let us consider one perturbation, and suppose each atom to be displaced by an atomic displacement $\delta\mathbf{u}$ from its equilibrium position, which results in changes in the external potential V_{ext}, the wave function of Kohn-Sham equation and the charge density $n(r)$. The atomic frequencies can be obtained by the diagonalization of the dynamical matrix:

$$D_{s\alpha s'\beta}(\mathbf{q}) = \sqrt{\frac{1}{M_s M_{s'}}} \sum_{\nu} \frac{\partial^2 E_{tot}}{\partial \mathbf{u}_{\mu s\alpha} \partial \mathbf{u}_{\nu s'\beta}} e^{i\mathbf{q}(\mathbf{R}_\nu - \mathbf{R}_\mu)} \tag{2.15}$$

Where s and s' run on atoms, α and β are cartesian components for each atom while $\mathbf{u}_{\mu s\alpha}$ and $\mathbf{u}_{\nu s'\beta}$ are the atomic displacements and $\mathbf{R}_\mu$,$\mathbf{R}_\nu$ indicate the Bravis lattice vectors. To obtain the full dispersion, derivatives of the energy and wave-functions are calculated on a grid of q-points. Detailed expressions can be found in [29].

Chapter 3

Transport Phenomena in solids

In general, all phenomena in which heat, electricity and matter itself are carried through a structure, under the influence of a temperature gradient, an electric field potential or an atomic concentration gradient are considered transport phenomena.
To study transport phenomena we need conservation laws formulated as continuity equations and equations which describe how a certain quantity responds to a perturbation via transport coefficients. An example can be the Fourier's Law of Heat Conduction which describes the response of heat flux to temperature gradients along a certain direction:

$$q_x = -\kappa \frac{dT}{dx} \tag{3.1}$$

Where q is the local heat flux density along x direction, κ is the material thermal conductivity and $\frac{dT}{dx}$ is the temperature gradient through x direction.

Understanding transport phenomena is nowadays a challenge for the discovery and the development

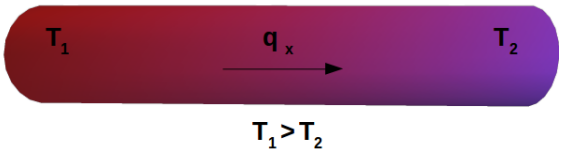

Fig. 3.1 Scheme for 1 dimensional Fourier's Law: the rate of heat flux q_x is proportional to temperature gradient $\Delta T = T_1 - T_2$. The proportionality factor κ is the material thermal conductivity.

of high-performance materials and devices for applications ranging from nanoelectronics to energy conversion technologies, among which we find thermoelectrics. To understand electrical and thermal flows, electrons have been treated as particles. For example, in the classic model, an electron moving with velocity $\vec{v}$ in presence of an electric field $\vec{E}$ after a time t will gain an energy given by:

$$\delta \mathscr{E} = e\vec{v} \cdot \vec{E}t \tag{3.2}$$

Assuming that its motion is governed by a *relaxation time* τ i.e. the time associated with the return to the equilibrium distribution, the probability at the time t that the particle has already lived without being scattered is:

$$P(t) = \exp^{-\frac{t}{\tau}} \tag{3.3}$$

Taking the average over, the extra energy due to electric field is:

$$\overline{\delta\mathscr{E}} = \int_0^\infty e\vec{v}\cdot\vec{E}t\frac{\partial P(t)}{\partial t}dt = e\vec{v}\cdot\vec{E}\tau \tag{3.4}$$

So the average drift velocity (in the case in which velocity and field are parallel) is:

$$\overline{\delta\vec{v}} = \frac{ev\tau}{\partial\mathscr{E}/\partial v}\vec{E} \tag{3.5}$$

Consequently, current density for n electrons per unit of volume is:

$$\vec{J} = ne\overline{\delta\vec{v}} = \frac{ne^2v\tau}{\partial\mathscr{E}/\partial v}\vec{E} \tag{3.6}$$

In the macroscopic form, introducing the electrical conductivity σ, the current density is given by:

$$\vec{J} = \vec{\sigma}\vec{E} \tag{3.7}$$

Where, with the definition of effective mass (m):

$$\sigma = \frac{ne^2\tau}{m} \tag{3.8}$$

On thermal conduction, a gradient of temperature ΔT is established and analogous to electrical conduction, it can be possible to find a relation between the amount of energy due to thermal flow and the particle velocity. The heat current is given by:

$$U = \frac{1}{3}Cv^2\tau\Delta T \tag{3.9}$$

Where the thermal conduction (introducing the mean free path Λ) is:

$$\kappa = \frac{1}{3}Cv\Lambda \tag{3.10}$$

In many metals and semiconductors there exists a coupling between the electrical current and the thermal current. This coupling can be appreciated by observing that when electrons carry thermal current, they are also transporting charge and therefore generating electric fields. Hence, this coupling between the charge transport and heat transport gives rise to thermoelectric phenomena.

3.1 Boltzmann transport equation (BTE)

Thermoelectric properties of materials have been traditionally simulated using Boltzmann Transport Equation (BTE). BTE provides a way to accurately and efficiently approximate the Seebeck coefficient S, the electrical conductivity σ and the electronic contribution to the thermal conductivity κ_e from first principles. BTE is a statistically based method that calculates properties at the nanoscale and larger, close to equilibrium conditions. It is a powerful way to study non-equilibrium systems through the application of properties of an equilibrium system. BTE uses the group velocities of charge carriers (obtained from the electronic structure of materials) combined with an occupational probability and shifting chemical potential to approximate charge transport.
Consider a system with non-uniform particle density and temperature. Within the system there are local regions where particles distributions are given by an equilibrium distribution function, which varies from place to place. A non-equilibrium Boltzmann transport equation expresses the global non-equilibrium distribution in terms of local equilibrium distributions.
Let us consider the distribution function $f(\vec{r},\vec{k},t)$ for a system of randomly moving electrons, which determines the probability of finding an electron at position $\vec{r}$ with a crystal momentum $\vec{k}$ at time t. Changes in the distribution function are due to 3 processes [35]:

- diffusion of particles
- collisions between particles
- effects of external fields

The diffusion process is the movement of electrons (subject to random movement from place to place) from an area of high concentration to an area of low concentration. Collisions between particles may cause loss of kinetic energy and generation of heat and depends on the time between two collisions. External fields are for example a thermal gradient or an external current applied to the system. The general equation can be written as:

$$\frac{df(\vec{r},\vec{k},t)}{dt} = \frac{\partial f(\vec{r},\vec{k},t)}{\partial t}\Big|_{diffusion} + \frac{\partial f(\vec{r},\vec{k},t)}{\partial t}\Big|_{collision} + \frac{\partial f(\vec{r},\vec{k},t)}{\partial t}\Big|_{fields} \tag{3.11}$$

In the steady state there is not net change in the distribution function, meaning that:

$$\frac{df(\vec{r},\vec{k},t)}{dt} = 0$$

It is conventional to write the diffusion process as a continuity equation in the absence of other phenomena:

$$\frac{\partial f(\vec{r},\vec{k},t)}{\partial t}\Big|_{diffusion} = -\vec{v}(\vec{k})\frac{\partial f(\vec{r},\vec{k},t)}{\partial \vec{r}} \tag{3.12}$$

With $\vec{v}(\vec{k})$ the group velocity of particles:

$$\vec{v}(\vec{k}) = \frac{1}{\hbar}\frac{\partial E(\vec{k})}{\partial \vec{k}} \tag{3.13}$$

For the fields by analogy:

$$\frac{\partial f(\vec{r},\vec{k},t)}{\partial t}\Big|_{fields} = -\frac{d\vec{k}}{dt}\frac{\partial f(\vec{r},\vec{k},t)}{\partial \vec{k}} \tag{3.14}$$

Therefore the BTE can be rewritten as:

$$\frac{\partial f(\vec{r},\vec{k},t)}{\partial t} + \vec{v}(\vec{k})\frac{\partial f(\vec{r},\vec{k},t)}{\partial \vec{r}} + \frac{d\vec{k}}{dt}\frac{\partial f(\vec{r},\vec{k},t)}{\partial \vec{k}} = \frac{\partial f(\vec{r},\vec{k},t)}{\partial t}\Big|_{collision} \tag{3.15}$$

The first term gives the explicit time dependence needed in case of time dependent perturbations.
In the case of a weak field, for example a weak electric field $\vec{E}$, the perturbation connected to the external force is assumed to be small enough so that the distribution function can be linearized. In our case, neglecting quadratic terms, the linearized BTE equation is :

$$f(\vec{r},\vec{k}) = f_0(E) + f_1(\vec{r},\vec{k}) \tag{3.16}$$

where: $f_0(E)$ is the equilibrium distribution function (Fermi function for electrons) depending only on the energy of electrons [36][37].

$$f_0(E) = \frac{1}{1+e^{(E-E_F)/K_BT}} \tag{3.17}$$

and $f_1(\vec{r},\vec{k})$ is the perturbation term. More explicitly:

$$\left(\frac{\partial f_0(\vec{r},\vec{k})}{\partial E(\vec{r},\vec{k})}\right)\vec{v}(\vec{r},\vec{k})\left[\frac{E-\mu}{T}\Delta T + e\vec{E}\right] = \left(\frac{\partial f(\vec{r},\vec{k})}{\partial t}\right) \tag{3.18}$$

3.1.1 Relaxation Time Approximation

To simplify this equation, it is often used the constant *relaxation time approximation (RTA)* for the collision contribution term in which the relaxation time is assumed to be independent of position and velocity of the electrons.
Physically, the relaxation time τ represents the time it takes for an electron to relax to the equilibrium from a non-equilibrium state when the external field (or more in general, when an external perturbation) is switched off.

$$\frac{\partial f(\vec{r},\vec{k})}{\partial t} = -\frac{f(\vec{r},\vec{k}) - f_0(\vec{r},\vec{k})}{\tau} \tag{3.19}$$

With this approximation, the BTE equation is solved to obtain the current density $\vec{j}(\vec{r},t)$:

$$\vec{j}(\vec{r},t) = \frac{e}{4\pi^3}\int \vec{v}(\vec{k})\cdot f(\vec{r},\vec{k},t)d^3\vec{k} \tag{3.20}$$

where $d^3\vec{k}$ is the element of 3D wave vector space.
In the next subsections we will present the expressions for the electronic parameters used in thermoelectricity derived from BTE.

3.1.2 Electrical Conductivity

As mentioned at the beginning of this chapter, the electrical conductivity can be derived from the macroscopic relation:

$$\vec{J} = \vec{\sigma}\vec{E} \tag{3.21}$$

Since there are not thermal gradients in the simplest calculation of electrical conductivity, equation 3.18 can be written as:

$$\left(\frac{\partial f_0(\vec{r},\vec{k})}{\partial E(\vec{r},\vec{k})}\right)\vec{v}(\vec{r},\vec{k})e\vec{E} = \left(\frac{\partial f(\vec{r},\vec{k})}{\partial t}\right) \tag{3.22}$$

By using the relaxation time approximation 3.19:

$$f_1(\vec{k}) = -e\tau\vec{v}(\vec{k})\cdot\vec{E}\frac{\partial f_0(E)}{\partial E} \tag{3.23}$$

and the electric current density can be obtained by replacing 3.23 in 3.20:

$$\vec{j} = \frac{e^2\vec{E}}{4\pi^3}\cdot\int \tau\ \vec{v}(\vec{k})\cdot\vec{v}(\vec{k})\cdot\frac{\partial f_0(E)}{\partial E}d^3\vec{k} \tag{3.24}$$

Thus, electrical conductivity is :

$$\vec{\sigma} = \frac{e^2}{4\pi^3}\cdot\int \tau\ \vec{v}(\vec{k})\cdot\vec{v}(\vec{k})\cdot\frac{\partial f_0(E)}{\partial E}d^3\vec{k} \tag{3.25}$$

3.1.3 Electronic thermal conductivity

Because in a lattice heat is carried by electrons as well as vibrating atoms, the thermal conductivity of any material is the sum of the electronic contribution and lattice contribution.

$$\kappa_{tot} = \kappa_e + \kappa_\ell \tag{3.26}$$

Let us consider the calculation of the electronic contribution to the total thermal conductivity.
Applying a thermal gradient to a solid results in a net heat flow. As in the previous case, we can define

a thermal current $\vec{U}$ driven by a difference in energy from the equilibrium $E - E_F$:

$$\vec{U} = \frac{1}{4\pi^3 T}\frac{\partial T}{\partial \vec{r}} \cdot \int \tau\, \vec{v} \cdot \vec{v}(E - E_F)^2 \;\; \frac{\partial f_0(E)}{\partial E} d^3\vec{k} \tag{3.27}$$

Thus, from Fourier's law mentioned at the beginning of this chapter:

$$\kappa_e = \frac{1}{4\pi^3 T} \cdot \int \tau\, \vec{v} \cdot \vec{v}(E - E_F)^2 \;\; \frac{\partial f_0(E)}{\partial E} d^3\vec{k} \tag{3.28}$$

3.1.4 Approximations for conductivities

The equations 3.25 and 3.28 are valid in general, but it can be complicated to deal with. Therefore some approximations are introduced:

1. In the case in which $(E - E_F) << k_B T$, where k_B is the Boltzmann constant, the distribution function is replaced with the classic Maxwell - Boltzmann distribution:

$$f_0(E) = e^{-(E-E_F)/k_B T} \tag{3.29}$$

2. Electronic bands are assumed to be parabolic:

$$E = \frac{\hbar^2 k^2}{2m^*} \tag{3.30}$$

3. Relaxation time τ is assumed to be constant (indipendent of $\vec{k}$ and E). With some mathematical steps, the final expression for σ is:

$$\sigma = \frac{2e^2\tau}{m^*}\left(\frac{m^* k_B T}{2\pi\hbar^2}\right)^{3/2} e^{-E_F/k_B T} \tag{3.31}$$

and

$$\kappa_e = cost \cdot {m^*}^{5/2} T^{5/2} \tau \quad e^{-E_F/k_B T} \tag{3.32}$$

with a numerical constant *cost* containing all the physical constants and numerical quantities. This usual assumption of a constant relaxation time (CRT) is in many cases inadequate for a quantitative comparison with experiment. In paragraph 3.2 a simple analytic energy and temperature-dependent model is explained to go beyond constant relaxation time approximation.

3.1.5 Seebeck coefficient

The Seebeck coefficient S is the characteristic coefficient which governs the Seebeck effect, where a material under a thermal gradient ΔT exhibits an open circuit voltage $\Delta V = -S\Delta T$ under conditions of no current flow. In the application of the Seebeck effect to thermocouple operation, it is usually

measured the difference $S_A - S_B$ between two different materials A and B by measuring the open circuit voltage V_{AB} as shown in Fig. 3.2 . This voltage can be calculated from:

$$V_{AB} = -\int_{T_1}^{T_2} (S_A - S_B) dT \tag{3.33}$$

The simplest formula for Seebeck coefficient is:

$$S = \frac{8\pi^2 k_B^2}{3eh^2} m^* T \left(\frac{\pi}{3n}\right)^{2/3} \tag{3.34}$$

This equation is an approximation as anticipated on Chapter 1, but, for many thermocouples, the $S(T)$ dependence is approximately linear, and for many materials there are only small variations from this relation.

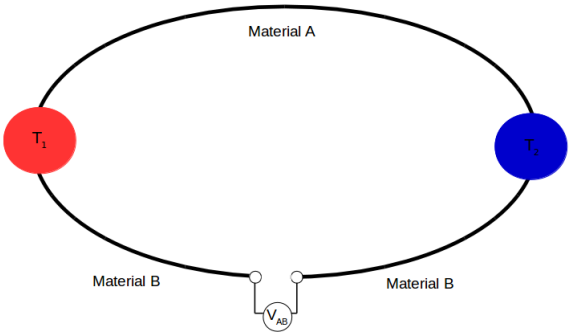

Fig. 3.2 Seebeck effect between two different materials showing the principle of operation of a thermocouple under open circuit conditions.

3.2 Scattering mechanisms for electrons

Transport properties depend on the number of carriers and on the way they can scatter. Electron collisions occur through a variety of mechanisms such as electron-phonon, electron-impurity, electron-defect, and electron-electron scattering processes [33] [34]. Here, principal mechanisms of electron scattering are presented.

3.2.1 Polar-optical scattering

The most important electron scattering mechanism for crystalline semiconductors is electron-phonon scattering, due to electrons scattered by the thermal motion of the lattice. The optical scattering is important only for polar semiconductors where the charge distribution has different signs on neighboring ion sites. In this case, the oscillatory electric field leads to oscillating dipole moments associated with longitudinal optical (LO) modes. This mechanism is important in III-V and II-VI compound semiconductors. According to Ridley formula [38][39], the total rate of the polar optical

scattering is given by:

$$P_{polar}(T,E) = \sum_i \frac{C(T,E,e_i^{LO}) - A(T,E,e_i^{LO}) - B(T,E,e_i^{LO})}{Z(T,E,e_i^{LO})E^{3/2}} \tag{3.35}$$

where the sum runs over all longitudinal-optical phonons, with energy e_i^{LO} the functions A , B , C , and Z are [39] :

$$\begin{aligned} A(E) = [n(\omega_{LO})+1]&\frac{f_0(E+\hbar\omega_{LO})}{f_0(E)} \\ &\times\left\{(2E+\hbar\omega_{LO})sinh^{-1}\left(\frac{E}{\hbar\omega_{LO}}\right)^{1/2} - [E(E+\hbar\omega_{LO})]^{1/2}\right\} \end{aligned} \tag{3.36}$$

$$\begin{aligned} B(E) = n(\omega_{LO})\theta(E-\hbar\omega_{LO})&\frac{f_0(E-\hbar\omega_{LO})}{f_0(E)} \\ &\times\left\{(2E-\hbar\omega_{LO})cosh^{-1}\left(\frac{E}{\hbar\omega_{LO}}\right)^{1/2} - [E(E-\hbar\omega_{LO})]^{1/2}\right\} \end{aligned} \tag{3.37}$$

$$\begin{aligned} C(E) = 2E\Bigg\{&n(\omega_{LO}+1)\frac{f_0(E+\hbar\omega_{LO})}{f_0(E)}sinh^{-1}\left(\frac{E}{\hbar\omega_{LO}}\right)^{1/2} \\ &+n(\omega_{LO})\theta(E-\hbar\omega_{LO})\frac{f_0(E-\hbar\omega_{LO})}{f_0(E)}cosh^{-1}\left(\frac{E}{\hbar\omega_{LO}}\right)^{1/2}\Bigg\} \end{aligned} \tag{3.38}$$

$$Z = \frac{2}{W_0(\hbar\omega_0)^{1/2}} \tag{3.39}$$

Where θ is the step function, ω_{LO} is the LO phonon frequency and $n(\omega_{LO})$ is the phonon occupation factor phonon, while :

$$W_0 = \frac{e^2}{4\pi\hbar}\left(\frac{2m^*\omega_{LO}}{\hbar}\right)^{1/2}\left(\frac{1}{\varepsilon_\infty} - \frac{1}{\varepsilon_s}\right) \tag{3.40}$$

and ε_s and ε_∞ are respectively the low-frequency and the high-frequency permittivities.
The importance of introducing these equations lies in the fact that here it is shown the explicit dependence of polar-optical scattering on phonons energy. The parameters derived from phonon calculations used to obtain the scattering rate, play a decisive role in the determination of transport coefficients, as we will see in the next chapters.

3.2.2 Acoustic phonon scattering

Acoustic phonon mechanism is associated with energy shifts of the energy band extrema caused by the compression and expansion of crystals during acoustic mode vibrations. The deformation potential scattering mechanism is important in crystals with inversion symmetry and with the same species on each site.
While LO optical phonons make a contribution in polar-optical scattering, for acoustic phonon scattering, it is the LA acoustic phonons that are most important. Acoustic phonon scattering is treated

within the elastic deformation potential [1] approach in the long-wavelength acoustic phonon limit, and the scattering rate is:

$$P_{ac}(T,E) = \frac{2\bar{m}^{3/2}k_BTD^2\sqrt{E}}{2\pi\hbar^4\rho v^2} \tag{3.41}$$

where E is the electron energy, D the deformation potential of the band energies calculated at the band extrema, ρ the mass density, v the average sound velocity, $\bar{m}$ the average effective mass.

3.2.3 Impurities scattering

As the temperature is reduced, phonon scattering becomes less important so that in this regime, ionized impurity scattering and other defect scattering mechanisms become prevalent. This scattering mechanism involves the deflection of an electron by the Coulomb field of an ion with charge Z_Ie. Using Brooks-Herring formula:

$$P_{imp}(T,E) = \frac{\pi n_I Z_I^2 e^4 E^{-3/2}}{\sqrt{2\bar{m}}(4\pi\varepsilon_0\varepsilon)^2}\left[log\left(1+\frac{8\bar{m}E}{\hbar^2 q_0^2}\right) - \frac{1}{1+(\frac{\hbar^2 q_0^2}{8\bar{m}E})}\right] \tag{3.42}$$

Where ε_0 and ε are the vacuum permittivity and the relative dielectric constant, Z_Ie is impurity charge, n_I is the ionized impurity concentration and:

$$q_0 = \sqrt{e^2 n_I/\varepsilon_0\varepsilon k_B T}$$

Scattering probabilities for more than one scattering process are additive and therefore the total relaxation time is obtained as the inverse of the total rate:

$$\tau(E,T) = \frac{1}{P_{imp}+P_{polar}+P_{ac}} \tag{3.43}$$

3.3 Lattice thermal conductivity

As mentioned above, total thermal conductivity is the sum of the electronic contribution κ_e and the lattice contribution κ_ℓ. The lattice thermal conductivity is calculated from kinetic theory and is given by:

$$\kappa_\ell = \frac{C_p v_q \Lambda_{ph}}{3} \tag{3.44}$$

where C_p is the heat capacity, v_q is the average phonon velocity that can be derived from the phonon dispersion and Λ_{ph} is the phonon mean free path. In semiconductors, this is the major contribution to thermal conductivity.

The lattice thermal conductivity κ_ℓ, is not directly connected to the other thermoelectric parameters.

[1] The deformation potential D is defined as the effective electric potential experienced by free electrons in a semiconductor or metal resulting from a local deformation in the crystal lattice.

A reduction in κ_ℓ is desirable to increase ZT and may be achieved by phonon scattering. For that reason, in our study, κ_ℓ plays a central role.

3.4 Scattering Processes in Phonons

In the same way that electron scattering is important in electronic transport properties, phonon scattering is important in thermal transport. The major scattering mechanisms for phonons are phonon-phonon scattering (Umklapp collisions), phonon-boundary scattering and isotope scattering, briefly discussed in the following subsections.

3.4.1 Phonon-Phonon scattering

Phonons are scattered by other phonons because of anharmonic terms in the potential acting on them. Two different options:

- a phonon mode $\mathbf{q}j$ scatters by absorbing another mode $\mathbf{q}'j'$ to generate a third phonon mode $\mathbf{q}''j''$
- a phonon mode $\mathbf{q}j$ decays in two modes $\mathbf{q}'j'$ and $\mathbf{q}''j''$

In these anharmonic processes, energy and wavevector conservation is different for normal and umklapp phonons:

- N - process

$$\mathbf{q}j + \mathbf{q}'j' = \mathbf{q}''j'' \tag{3.45}$$

- U - process

$$\mathbf{q}j + \mathbf{q}'j' = \mathbf{q}''j'' + \mathbf{Q} \tag{3.46}$$

where $\mathbf{Q}$ corresponds to a phonon wave vector of magnitude comparable to that of reciprocal lattice vectors. When Q is zero the interaction is called an N-process. When there are umklapp processes [2] the scattered phonon wavevector can be in a direction opposite to the energy flow. For that reason, umklapp processes are important in considering the lattice contribution to the thermal conductivity because they dominate the thermal conductivity at high T for low defect crystals (Fig.3.3) with a 1/T dependence.

[2] The name derives from the German word umklappen (to turn over), because of the behavior of phonons when this phenomenon occurs.

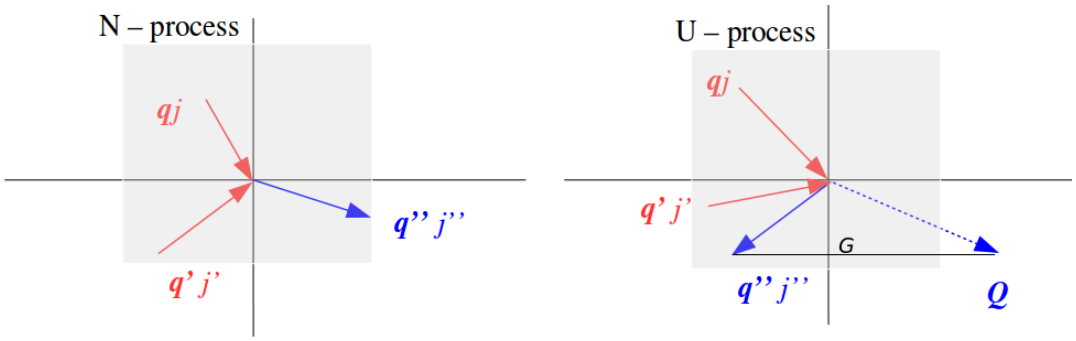

Fig. 3.3 Normal process (N-process) and Umklapp process (U-process). While the N-process conserves total phonon momentum, the U-process changes phonon momentum.

3.4.2 Phonon Boundary Scattering

The border scattering results in a process that describes the reflection of a phonon from a specific state(qj) from the surface. Phonon-boundary scattering is important at low temperatures where the phonon density is low and it is particularly important in low-dimensional nanostructures. In this regime, the scattering time is independent of T. The thermal conductivity in this range is proportional to the phonon density thus to T^3.

3.4.3 Isotope Scattering

Isotope phonon scattering is due to different isotopes of the host constituents. This mass disorder can play a role when calculating the lattice thermal conductivity.

3.4.4 Limit of κ_ℓ

By alloying, as already mentioned in the introduction, the lattice thermal conductivity lowers. The reasons are the scattering phonons processes mentioned above. The short wavelength phonons are scattered by point defects created by substituted atoms as well as impurities. The rate of scattering is determined by the mass of the atoms, hence alloying is a key point for phonons scattering.
Phonons may also be scattered by grain boundaries. Reduction of grain size to maximize the grain boundary area has successfully lowered the thermal conductivity in a number of materials [40] [41].
A lower limit in κ_ℓ can be estimated by using the Einstein model for thermal conductivity. Assuming that the atoms are harmonic oscillators with the Einstein frequency (ω_E) coupled to each other, but the oscillations are not coherently coupled as would be the case in a crystal lattice, the expression for the lower limit (often referred to as the amorphous limit or phonon glass limit) of the thermal conductivity $\kappa_\ell^{\min}$ is :

$$\kappa_\ell^{min} = \left(\frac{\pi}{6}\right)^{1/3} k_B n^{2/3} \sum_i v_i \frac{T}{\theta_i} \int_0^{\frac{\theta_i}{T}} \frac{x^3 e^x}{(e^x-1)^2} dx \tag{3.47}$$

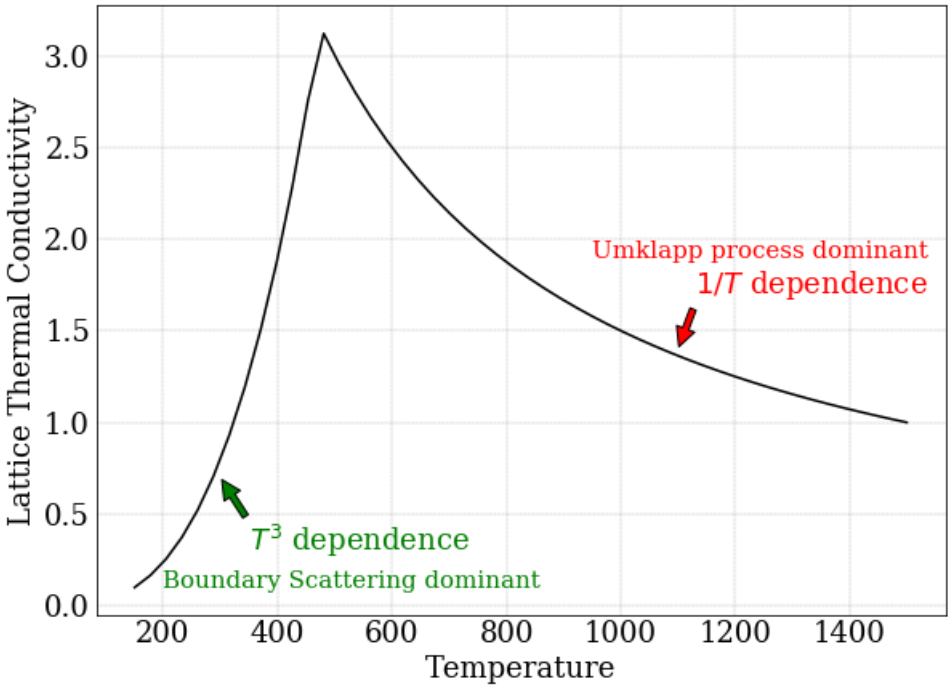

Fig. 3.4 Typical trend in lattice thermal conductivity at increasing temperatures. At low temperatures the conductivity is limited by boundary scattering. At high temperatures it is limited by Umklapp-scattering

where n is the number density of atoms and θ_i is the temperature corresponding to the cutoff frequency for each polarization in Kelvin. The phonon group velocity v_i is assumed to be constant for all modes while sum is taken for the three acoustic modes (two transverse and one longitudinal). This approach has correctly estimated a lower limit for for a large number of compounds [42]. This limit to the thermal conductivity leads to the concept of *Electron-crystal Phonon-glass*, indeed what we need in thermoelectricity is a material with optimal electronic properties like perfect crystals and at the same time a glass behavior to reduce the thermal conductivity.

Chapter 4

Zintl phase Mg_3Sb_2

In the following section I report the work done during my first Ph.D. year. During this time I studied a promising thermoelectric material, the β phase Mg_3Sb_2, both in terms of electronic transport coefficients and lattice thermal conductivity.

4.1 Introduction

As we have already seen in the first chapter, a good thermoelectric material requires the combination of high electrical conductivity (σ), low thermal conductivity (κ), and high thermopower or Seebeck coefficient (S), ultimately resulting in a high figure of merit. Materials that best meet these requirements are typically heavily doped, small band-gap semiconductors or semimetals. Such materials provide a balance between the high Seebeck coefficient of semiconductors and the low electrical resistivity of metals.

4.1.1 Zintl phase

Zintl phase is the product of a reaction between an alkali metal or alkaline earth and any post-transition metal or metalloid. From an electronic point of view, these compounds are defined as valence precise intermetallic phases in which electro-positive cations donate electrons to covalently bonded poly-anions [43]. Complex Zintl antimonides have recently emerged as a new class of promising thermoelectric materials due to their low lattice thermal conductivity and highly favorable electronic properties. However, most of these compounds consist of expensive, rare, and toxic elements, limiting their industrial power generation applications. Among reported thermoelectric Zintl compounds, Mg_3Sb_2 consists of cheap, environmentally friendly, and earth abundant elements. The Zintl β-phase Mg_3Sb_2 crystallizes in the $CaAl_2Si_2$ structure (space group $P\bar{3}m1$, No. 164) with two inequivalent Mg sites, denoted as $Mg_{(I)}$ and $Mg_{(II)}$, occupying the 1b (0, 0, 0.5) and 2d (1/3, 2/3, 0.834) Wyckoff positions, respectively and the Sb atoms at 2d (1/3, 2/3, 0.228). The crystal structures of Mg_3Sb_2 was reported by Zintl and Husemann in 1933 [44].

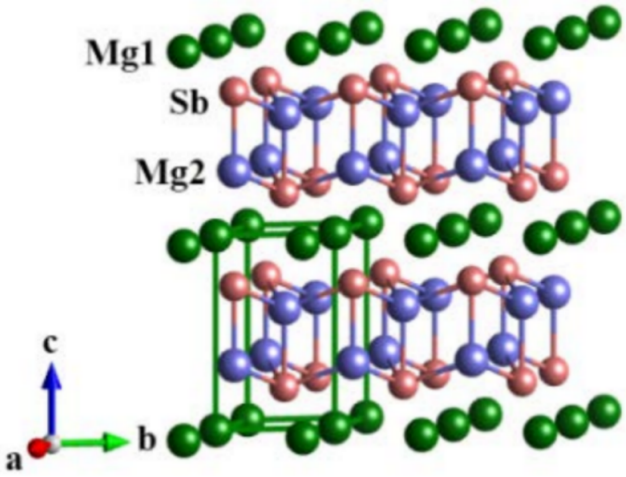

Fig. 4.1 The Zintl β-phase Mg_3Sb_2 crystallizes in the $CaAl_2Si_2$ structure (space group $P\bar{3}m1$, No. 164) with two inequivalent Mg sites, denoted as $Mg_{(I)}$ and $Mg_{(II)}$, occupying the 1b (0, 0, 0.5) and 2d (1/3, 2/3, 0.834) Wyckoff positions, respectively and the Sb atoms at 2d (1/3, 2/3, 0.228)

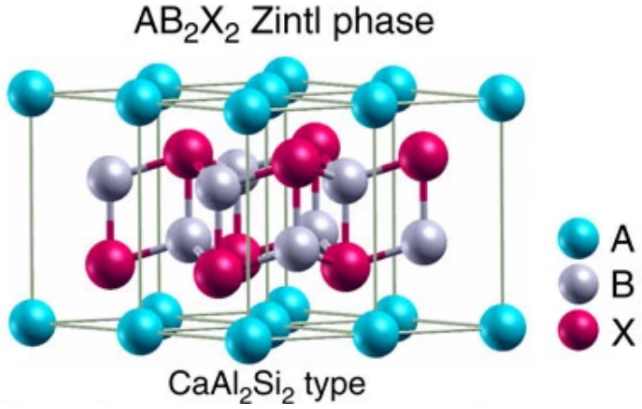

Fig. 4.2 Crystal structure and electronic bands of $CaAl_2Si2$-type Zintl compounds. AB_2X_2 Zintl compounds crystallize in trigonal (space group: Pm1) $CaAl_2Si2$-type structures, where A is an alkaline-earth or a divalent rare-earth element, B is a transition-metal or a main group element, X normally comes from group 15 and 14. Generally, layered AB_2X_2 Zintl compounds can be described as trigonal monolayers of A^{2+} cations in the a-b plane separating $[B_2X_2]^{2-}$ covalently bound slabs. [45]

In this chapter we show a complete study of the electronic transport coefficients and the thermoelectric figure of merit ZT in n-doped Mg_3Sb_2 based on density-functional electronic structure and Bloch-Boltzmann transport theory with an energy- and temperature-dependent relaxation time. Both the lattice and electronic thermal conductivities affect the final ZT significantly, therefore we included the lattice thermal conductivity calculated *ab initio*. Here, the lattice thermal conductivity of Mg_3Sb_2 is studied from first principles, with the inclusion of anharmonic, isotope, and boundary scattering processes, and via an accurate solution of the Boltzmann equation. All the theory used for this calculations can be found on Chapter 3.
This chapter is divided in two sections: in the first one I will present the lattice thermal conductivity calculations, while in the second one I am going to discuss electronic transport calculations.

4.2 Lattice Thermal Conductivity

4.2.1 Computational details

We use the QUANTUM ESPRESSO suite [27][28] to optimize the structure of Mg_3Sb_2 and obtain the phonon spectrum, and the D3Q - THERMAL2 codes [46] [47] for the anharmonic force constants, thermal conductivity, and q-dependent linewidths, including Casimir and isotopic-disorder scattering. We use generalized-gradient approximation (GGA) density-functional theory (DFT) for electron-electron interaction, and Hartwigsen-Goedeker-Hutter [48] norm-conserving pseudopotentials for electron-ion interaction. The plane-wave cutoff is set at 50 Ry, and the k-point grids are $8\times8\times8$ for both structure optimization and phonon dynamical-matrix calculations, $4\times4\times4$ for the third-order force constants, and $10\times10\times10$ for the thermal conductivity. For the lattice thermal conductivity calculation, the "exact" iterative conjugate-gradient solution method of Ref. [47] is used, with δ functions mimicked by Gaussians with a width of 5 cm^{-1} . Tests on grids, cutoff, and widths suggest that the lattice thermal conductivity value is stable to within about 5 %.

4.2.2 Results for lattice thermal conductivity

Here, we take into account different mechanisms of scattering to understand the reason of low κ values and if vibrational properties are responsible for that. Figure 4.3 reports the inverse average of the tensor components: since we are dealing with an hexagonal structure, due to the crystal symmetry , these components are (mildly) anisotropic: they are $\kappa_\ell^{xx} = \kappa_\ell^{yy} \simeq 1.1\kappa_\ell^{zz}$. Starting with only anharmonic scattering, the resulting lattice thermal conductivity is about 10 W/(m· K) at 400 K: that value differs from most experiments for which κ_ℓ is ten times smaller. The blue dashed-dotted curve shows the typical behavior for umklapp phonons processes, with a $1/T$ dependence for κ_ℓ. Including isotopic disorder scattering, due to different isotopes of Mg and Sb, κ_ℓ is slightly reduced but not enough to explain experimental results. Then, considering Casimir boundary scattering, lattice thermal conductivity decreases by 30%. This difference is more marked at low temperatures, where the T^3 dependence of lattice thermal conductivity, typical of boundary scattering, is dominant. That

result is obtained with a length $L = 50$ nm and an isotropic shape. In our calculation a correction factor (F) is present depending on the width to length ratio of the sample (more info in [47][83][84][85]). F is set to 1 and it takes into account grains with rough surface and separated by large disordered regions as found in the real material. That factor plays an important role for κ_ℓ: actually, setting F = 0.5, lattice thermal conductivity decreases by 15 - 20 % (see formula 4.1).

$$P^C_{\mathbf{q},j,\hat{\mathbf{n}}} = \frac{c_{\mathbf{q},j} \cdot \hat{\mathbf{n}}}{FL} n_{\mathbf{q},j}(n_{\mathbf{q},j} + 1) \tag{4.1}$$

with n the equilibrium phonon occupations, L the film thickness, F a correction factor between 0.5 and 1 (we set it to 1), $c_{\mathbf{q},j}$ the group velocity of mode j at wave vector $\mathbf{q}$, and $\hat{\mathbf{n}}$ the normal to the film. The last ingredient considered in our calculation is the polycrystallinity of this compound. The grain

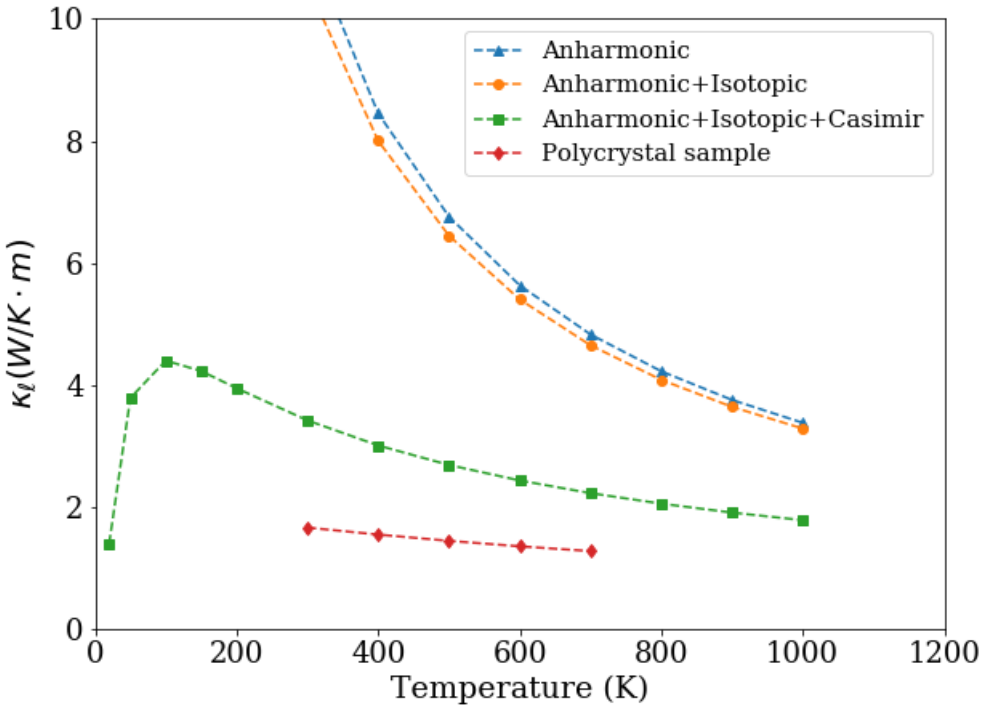

Fig. 4.3 Temperature dependence of lattice thermal conductivity in Mg_3Sb_2 . On the top curve the calculation was done with only anharmonic scattering, then we included anharmonic and isotopes (second curve from the top); anharmonic, isotopes, and Casimir scattering with a length L = 50 nm (third curve). The lowest curve (plotted in red with diamonds) is the average conductivity over an experimental grain-size distribution in Mg_3Sb_2 polycrystals as reported on [49].

size distribution is based on that used by [50] and, first of all, we analyzed the size dependence of κ_ℓ at room T and compared with grain size distribution of figure 3d of [50] finding that grain distribution is localized over about 20 nm in average and at larger values it becomes negligible [63]. Supposing randomly oriented grains with size L and assuming that thermal transport occurs in series, the lattice

thermal conductivity averaged over all grains is:

$$\bar{\kappa}_\ell = 1/\left[\sum_L \frac{n_L}{\kappa_\ell(L)}\right] \tag{4.2}$$

Where n_L is the grain size normalized distribution (Figure 4.4). At room temperature, $\bar{\kappa}_\ell$ is about 1.65 W/(m · K), in agreement with experiments. We can conclude that the major cause of low thermal

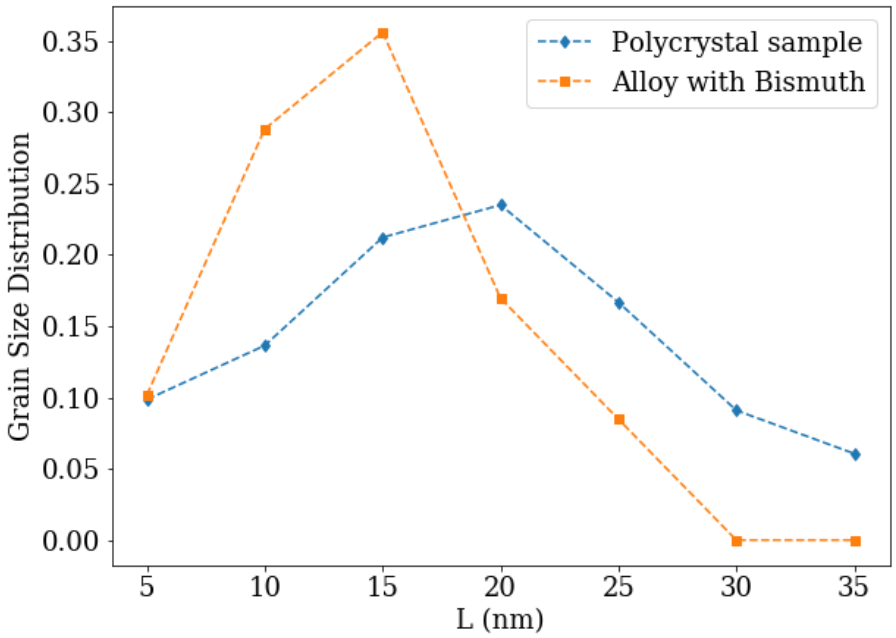

Fig. 4.4 Normalized distributions of grain sizes vs sample length in Mg_3Sb_2 and $Mg_3Sb_{1.8}Bi_{0.2}$(the distribution of grain sizes is taken from [50])

conductivity in Mg_3Sb_2 is due to its polycrystalline behavior. Finally, we consider more in detail the mass disorder in the case in which 10 % of Sb is replaced by Bi as it were a heavy isotope. To reproduce the distribution we follow the composition of that alloy from reference [50]. The resulting thermal conductivity is in good accordance with experiments [49]. The alloying reduces appreciably the value of κ_ℓ and therefore enhances ZT. The largest effect, of course, on ZT comes from the crystallinity or polycrystallinity of the samples (Fig. 4.22).

Indeed, as anticipated in the introduction, the nanostructuring is one of the ways to improve the thermoelectric efficiency via a reduction of lattice thermal conductivity from the value in crystalline samples. We will return to this point in the last section of this chapter.

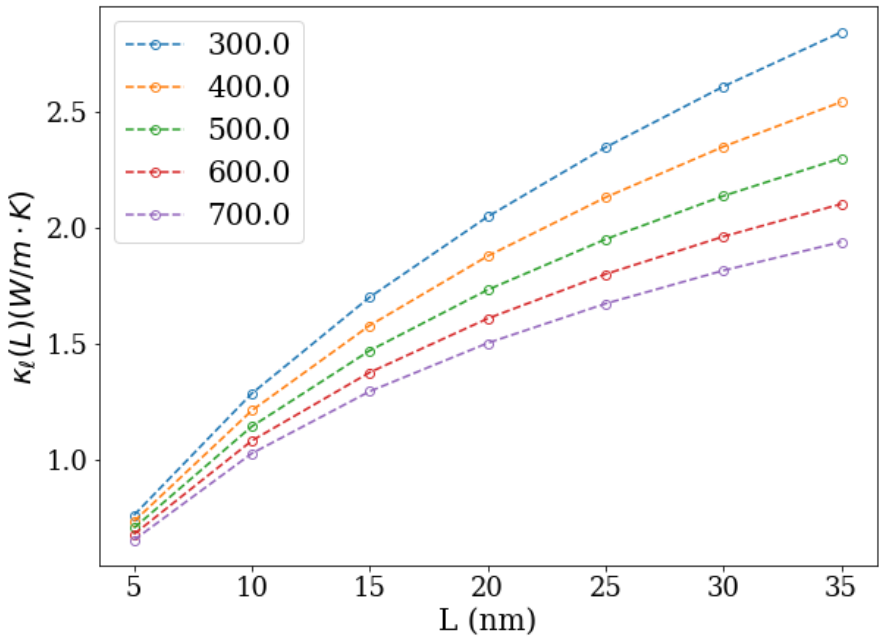

Fig. 4.5 Lattice thermal conductivity as a function of grain size L computed for different temperatures for a sample of Mg_3Sb_2. Temperatures are in Kelvin.

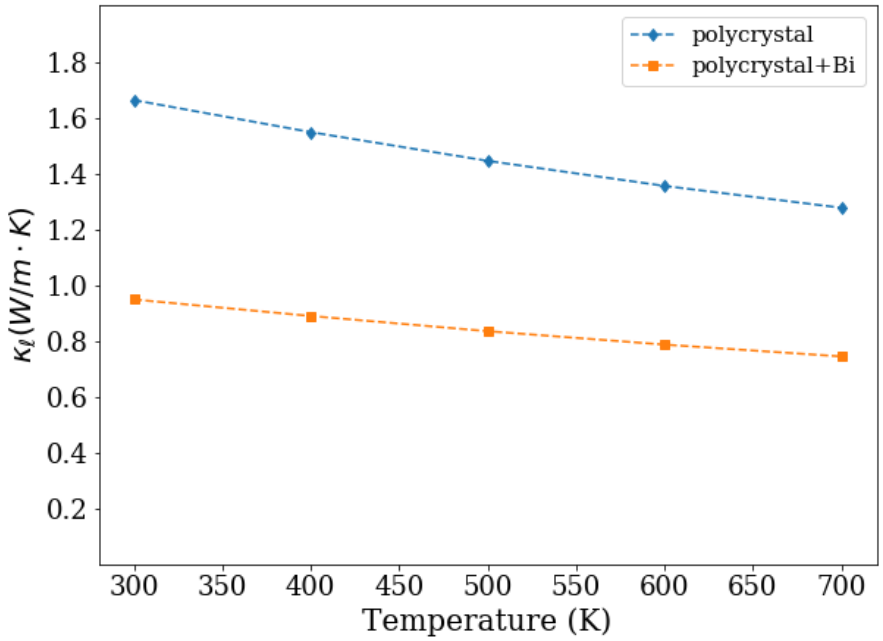

Fig. 4.6 Lattice thermal conductivity with a polycrystal sample of Mg_3Sb_2 and with an alloy with Bismuth given by $Mg_3Sb_{0.8}Bi_{0.2}$ from [49]

Phonons linewidths

In this paragraph, I will briefly discuss the phonon-phonon scattering and the relative phonon linewidth. The energy dependence of phonon linewidth exhibits its largest values in the central region of the spectrum, between 100 and 150 cm^{-1}, we can see the largest values of linewidths (Fig. 4.7). Watching the phonon dispersion considering only anharmonic and isotope scattering, they are much more relevant along the Γ-A-L-M-Γ path. Including Casimir scattering the regions close to A and M points have the most significant scattering 4.8a and 4.8b. This behavior is in agreement with [51].

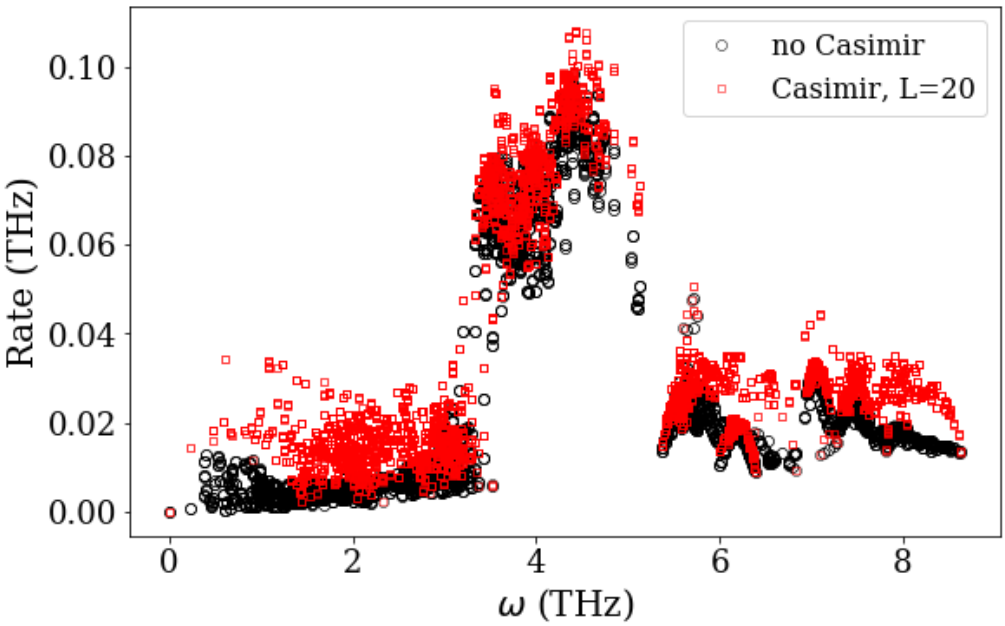

Fig. 4.7 Phonon linewidths as function of energy, with and without Casimir scattering, with a scattering length of L = 20 nm, at 300 K

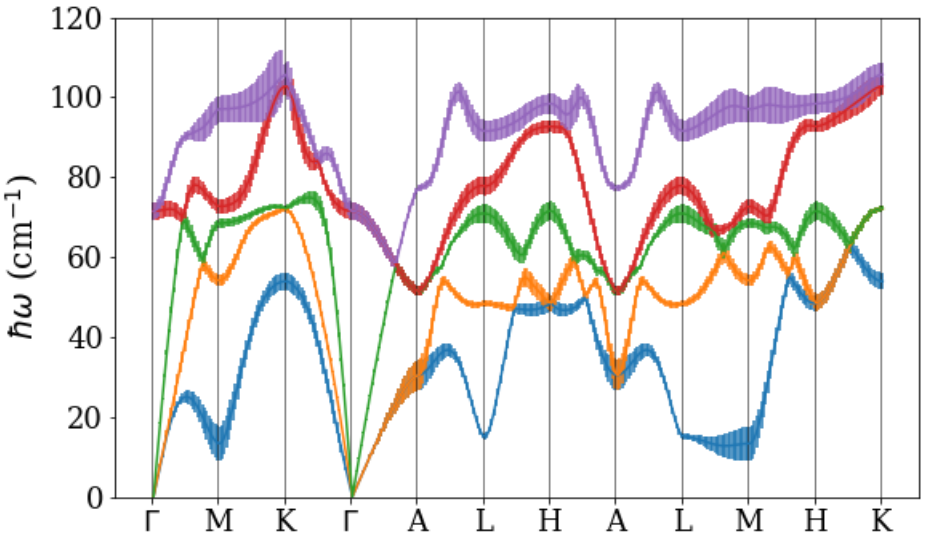

(a) – Phonon linewidths for low-energy phonons including anharmonic and natural-isotope scattering, infinite size of the sample at 300 K.

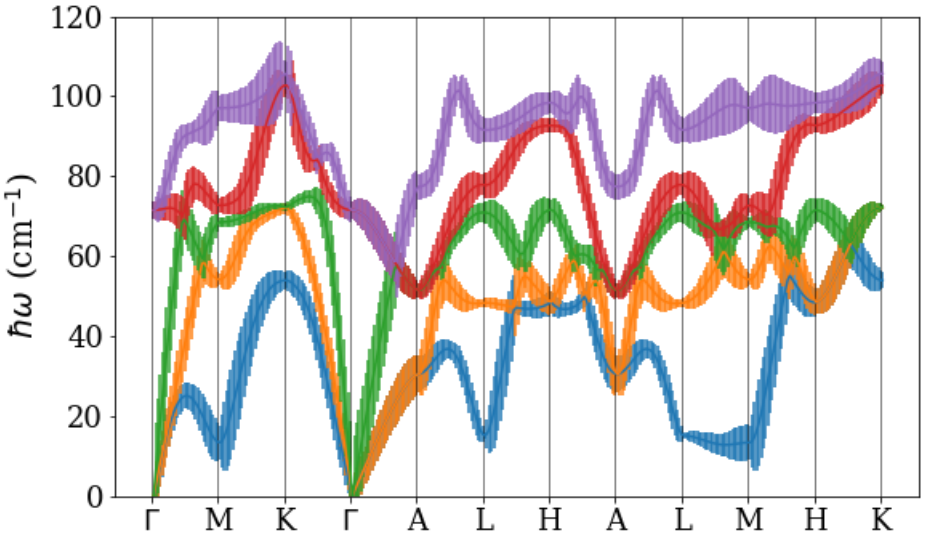

(b) – Phonon linewidths for low-energy phonons including anharmonic and natural-isotope scattering and Casimir scattering, with a length of L = 20 nm and T = 300 K

Fig. 4.8 Phonon linewidths

4.2.3 Comparison with experiments

We now compare our results with experiments and other theoretical investigations of lattice thermal conductivity in Mg_3Sb_2.

Two papers, [54] and [55], give an estimation of $\kappa_\ell \simeq 1.5$ W/(K·m), by using harmonic and anharmonic force constants obtained via a fit to frozen-phonon distortions in real-space supercells to build the relaxation time for use in the Boltzmann equation.

One of the differences from our calculation may be the group velocity estimation: indeed ,in our case, group velocities are directly estimated from interpolated dynamical matrices obtained with a grid of $8\times\ 8\times 6$, while in other works phonon group velocities are computed as finite differences on k grids, based on force constants obtained on relatively coarser equivalent grids. However, in those papers, the method used is not specified, nor is specified whether convergence in k-point in the Boltzmann equation solution is reached.

In addition, Ref. [55] uses single-mode approximation, that may artificially reduce κ_ℓ, an effect mentioned in [47]. By contrast,in our calculation the full iterative solution of Ref. [47] is used and we carefully checked convergence in k-space.

Another paper [52] reports a κ_ℓ of 2.5 W/(K·m) obtained via an expression involving average Grüneisen parameters and sound velocities.

Many experimental papers report low thermal conductivities (1 - 1.5 W/(K · m)) in Mg_3Sb_2-based polycrystals and alloys [55] and are in general agreement with our proposed explanation. Instead [56] reports a κ_ℓ about 1.5 W/(K · m) at room temperature in nominally pure and perfect single crystals[1] as well as in alloys without any explanation of the reason why polycrystals and single crystals would have essentially the same lattice thermal conductivity.

It may of course be the case that the single-crystal unalloyed character of the samples is not as perfect as declared; in general, single crystals are apparently hard to come by (and may in fact be uninteresting technologically), intentional alloying is ubiquitous, and general defectivity and off-stoichiometry are considerable.

Ref. [57] and [58] suggests that, by varying composition, impurity content, preparation of samples, κ_ℓ assumes a wide range of values (6 W/(m·K) in Ref. [57], while in Ref. [58] they go from 2.5 W/(m·K) in hot-pressed pellets to 1.5 W/(m·K) in alloyed materials). If we consider only mass disorder (i.e. isotope disorder) as source of scattering, neglecting Casimir boundary scattering, assuming a composition with a strong mass disorder like $Mg_{2.99}Sb_{1.5}Bi_{0.5}$ taking cues from [55], we find at room T a value for κ_ℓ equal to 1.6 W/(m·K) in agreement with experiments, so we can say that κ_ℓ can be suppressed by polycrystallinity and large mass disorder [2].

We are lead to conclude that the anomalously low observed conductivity is due to grain-boundary scattering of phonons, as we mentioned in the introduction, while the pure anharmonic contribution to the lattice thermal conductivity is an order of magnitude larger. Other mechanism seem to contribute

[1] since κ shows a typical finite-size downturn at low T [57], it is unclear whether this value is representative of macroscopic single crystals

[2] the $x = 2.99$ Mg composition is meant to simulate the effect of Mg vacancies at the 1% concentration level.

significantly to decrease the conductivity. Combining ab initio values vs sample size with measured grain-size distributions, we obtain an estimate of κ_ℓ vs T in nanopolycrystalline material in good agreement with typical experiments, and compute the ZT figure of merit in the various cases, that I will present in the next section.

4.3 Electronic Transport Coefficients

4.3.1 Computational details

The electronic and atomic structure of this compound are calculated within density functional theory in the generalized gradient approximation (GGA) with the projector augmented wave (PAW) as implemented in the VASP code [26]. Mg_3Sb_2 has been relaxed in trigonal symmetry (space group P-3m1 [164]), obtaining a=4.60Å, c=7.28Å as lattice parameters. Standard cut-off is used for the plane wave basis, and the k-point mesh for the bulk material is 24 $\times$24$\times$18. The eigenvalues are then interpolated by a Fourier-Wannier technique [59] over a finer grid including a number of k-points given by the original number of points times an amplification factor, which we choose to be A = 20 (the approximate equivalent grid will be 65$\times$65$\times$48). This setting is enough to converge with a variation for example, for the Seebeck coefficient of about 1% compared with a 12$\times$12$\times$12 ab initio grid, depending on T. *Ab initio* band structure calculation by density functional theory (DFT) for

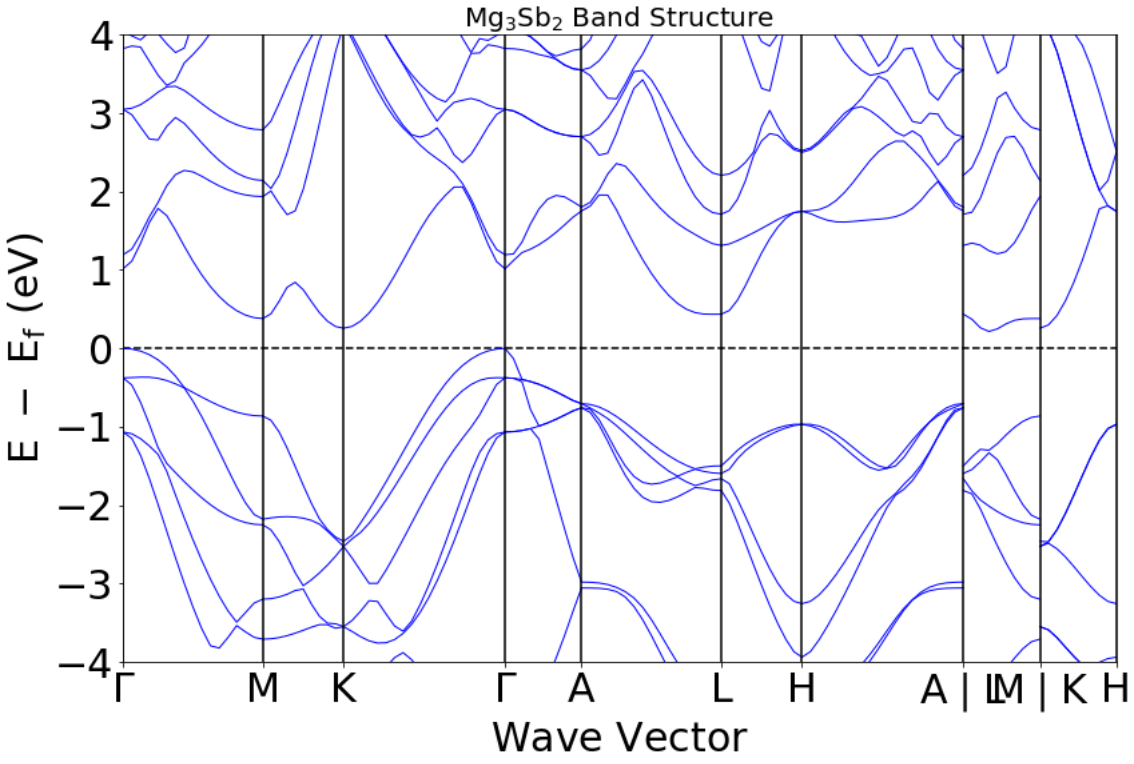

Fig. 4.9 Calculated GGA band structure of Mg_3Sb_2 as obtained from Vasp. The dashed line through energy zero represents the Fermi level. The minimum (indirect) gap is 0.13 eV. Fermi surface of n-type Mg_3Sb_2 exhibits 6 anisotropic carrier pockets along the M-L line and 6 one-third pockets at the K point, whereas p-type Mg_3Sb_2. It possesses only one highly anisotropic carrier pocket at the Γ point

Mg_3Sb_2 along the high-symmetry directions path is presented in Fig. 4.9.

The valence band maximum peak is at the Γ-point (Center of Brillouin Zone), the conduction band

minimum is at the *K*-point and degenerate in energy [3] with the point along the L-M segment of the hexagonal Brillouin zone. Hence, Mg_3Sb_2 is an indirect band-gap semiconductor. The first minimum of conduction band possesses a valley degeneracy of 2 while the minimum along L-M band possesses a valley degeneracy of 6. [49]

Detailed analysis of DOS reveal that the valence bands are spread by about 10 eV and can be broadly divided into two main parts. The first part is the low lying band located at about 9 eV (Fig. 4.10) which mainly comprise the Sb states. The second part is located from -5 eV to the Fermi Energy and are dominated by the Sb with little contribution of the Mg states. The conduction band is composed of the Mg and Sb states. The gap magnitude is estimated to be 0.22 eV, when exchange correlations were treated in the GGA formalism. A more detailed analysis of band structure is presented on Fig. 4.11 where the elements contributions to the overall spectrum are indicated by a color representation. It is also interesting to note the distribution of the Mg and Sb states, according to the fat-band analysis as shown in Fig. 4.11. Mg atoms appear to be insignificant in determination of in the valence band, suggesting they have a ionic character in the system. Interestingly, it is also found that some of the Sb states are distributed in the empty conduction band centered on the Γ-point. It seems to be appropriate suggesting a fully ionic Mg(I) atom with a certain degree of covalency between the Mg(II)-Sb and Sb-Sb bonds [50].

This behavior is typical of Zintl materials. Indeed, for these compounds the mostly ionic cations are

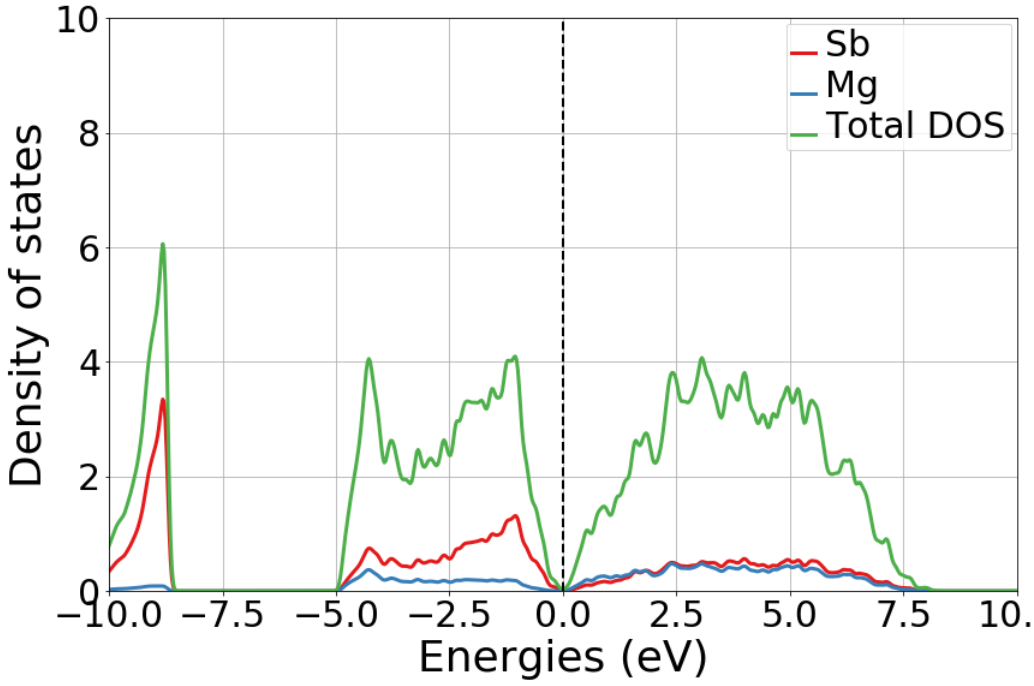

Fig. 4.10 The GGA calculated total and atom-resolved density of states of Mg_3Sb_2. The dashed line through energy zero represents the Fermi level.

[3] The energy difference between these two conduction bands is about 0.02 eV. This is a small energy difference compared with k_BT at room T. Consequently, it might be said that the two conduction bands converged.

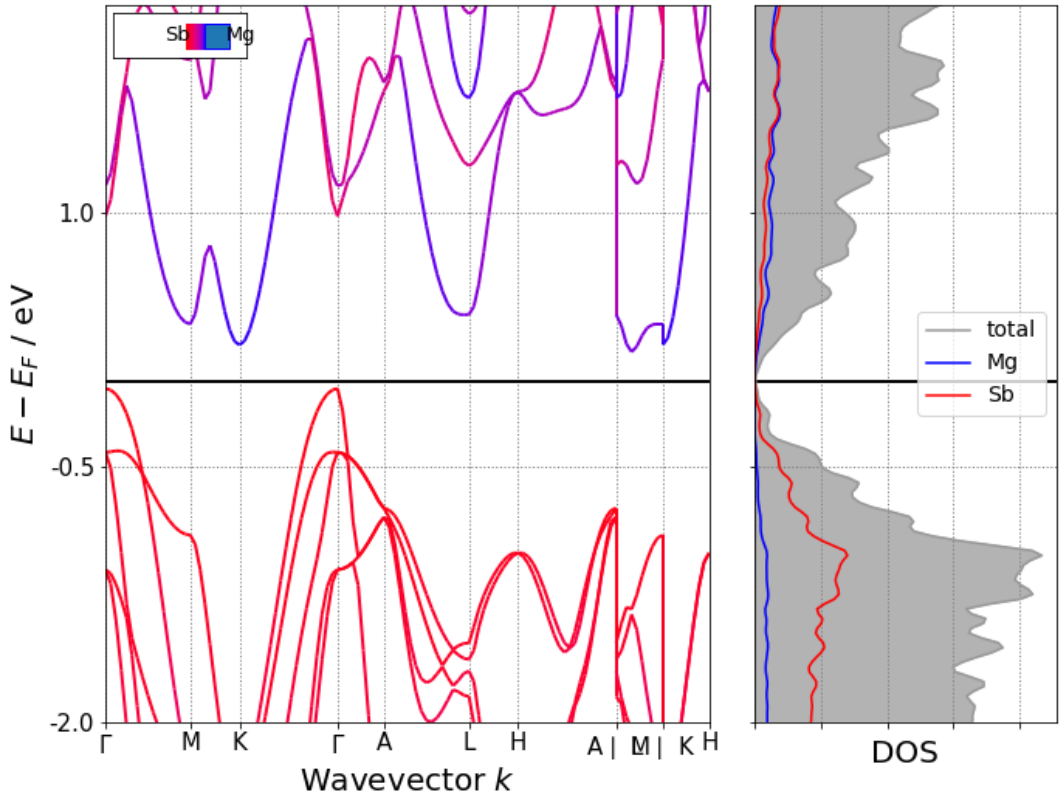

Fig. 4.11 The GGA generated band structure of Mg_3Sb_2 as obtained from Vasp. The red and the blue colors are the representation of the Sb and Mg states, respectively. The black line through energy zero represents the Fermi level. The valence band is dominated by Sb states, while the conduction band is a mixture of Sb and Mg states.

supposed to be electron donors, donating their electrons to the covalently bonded anionic substructures. The covalent bonding in the anionic parts leads to a significant orbital overlap, a light band mass, and thereby, a high carrier mobility, whereas the ionic cations are suitable for doping substitution, with the aim to tune the carrier density without affecting the covalent anionic networks (as it is done with Bismuth for instance). Such bonding features make Zintl compounds, and in particular Mg_3Sb_2 very promising for thermoelectric applications [53]

To compute electronic transport properties we used the BoltzTraP [59] code, obtaining directly from it Seebeck coefficient, electrical conductivity and electronic thermal conductivity under the rigid bands approximation, which assumes that bands do not change with doping or temperature. In the following equations the expressions for these quantities are summarized:

$$\sigma = \mathscr{L}^{(0)} \tag{4.3}$$

$$S = \frac{\mathscr{L}^{(1)}}{eT\mathscr{L}^{(0)}} \tag{4.4}$$

$$\kappa_e = \frac{1}{e^2T}\left(\frac{\mathscr{L}^{(1)}}{\mathscr{L}^{(0)}} - \mathscr{L}^{(2)}\right) \tag{4.5}$$

with e the electronic charge and

$$\mathscr{L}^{(N)} = e^2 \int K(E,T)(E-\mu)^N\left(-\frac{\partial f_F(E,\mu,T)}{\partial E}\right)dE, \tag{4.6}$$

$$K(E,T) = \int \sum_b \mathbf{v}_{b,k} \times \mathbf{v}_{b,k}\tau_{b,k}\delta(E - E_{b,k})\frac{d\mathbf{k}}{8\pi^3} \tag{4.7}$$

where b is the band index, $\mathbf{k}$ is the wavevector, $E_{b,k}$ is the band energy, $\mathbf{v}_{b,k}$ is the band velocity, f_F the Fermi distribution, μ the chemical potential and τ the relaxation time. These equations are exactly the same as I reported in Chapter 3 in a different way.
In our study, major electronic scattering sources are included, namely electronic acoustic phonons, polar-optical phonons and charged impurities scattering. These three rates of scattering have been implemented by our group in BoltzTraP code. The single mechanisms, more in detail, are reported in Chapter 3. As you will see in the next sections, the choice to use a model for relaxation time based on main scattering mechanisms for electrons makes the difference in the calculation of the figure of merit.

Parameters used in calculations

All the material parameters needed in scattering processes are computed via Quantum-Espresso code except for effective masses imported from [49] and [50]. These values are:

- ε_∞ = 14.2
- ε = 26.7
- average sound velocity $\mathbf{v}$ = 2.7 km s^{-1}
- LO-phonon frequencies ω_{LO} = 165 cm^{-1}, 220 cm^{-1}, 250 cm^{-1}
- conduction-band deformation potential D = 6.4 eV
- average effective mass m^* = 0.3 m_e
- constant relaxation time $\tau_0 = 1.34 \cdot 10^{-14}$ s

4.3.2 Results for electronic calculations

Figure 4.12 shows the behavior of $\tau(T,E)$ and its components as function of T at 40 meV above the band edge and, as function of energy at 500 K. As expected in polar semiconductors (see also chapter

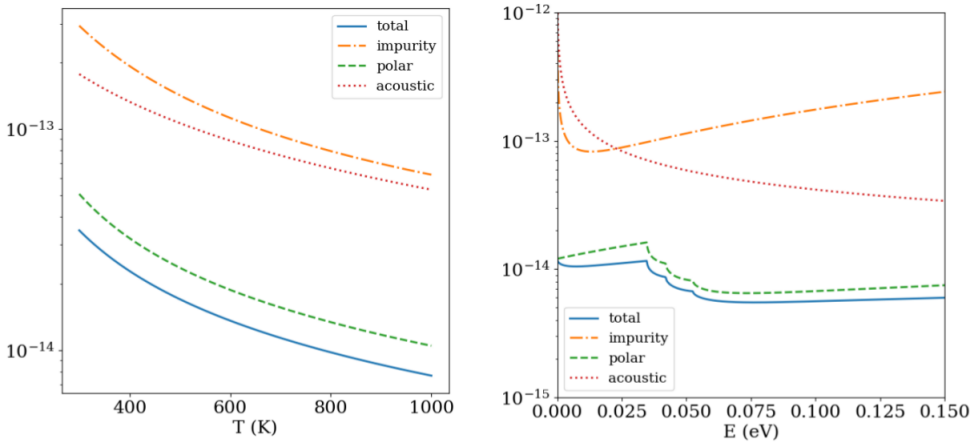

Fig. 4.12 Left: τ vs Temperature at E = 40 meV at optimal doping level. Right: τ vs Energy at T = 500 K at optimal doping level.

3), scattering of carriers by optical phonons is the principal mechanism which determines mobility at room T: since LO phonons energies are low in Mg_3Sb_2 and τ is inversely proportional to them, the total relaxation time is definitely dominated by polar scattering.

Electronic thermal conductivity

In our calculations we use the total thermal conductivity. The electronic thermal conductivity is shown below, while the lattice thermal conductivity was the subject of section 4.2.
All the calculations refer to doping of *n*-type. As it can be seen in Figure 4.13, κ_e has the same order of magnitude as κ_ℓ. Comparing the case of energy-dependent scattering time and constant scattering time at the same level of doping, κ_e rises with T in the constant scattering time model. As can be seen in Fig. 4.14, different scattering models lead to qualitatively different predictions. In the constant-time approximation, κ_e becomes larger than in the energy-dependent case and rises sharply at high temperature, because the constant relaxation time does not take into account the phonon scattering, dominant scattering mechanism for electrons as the temperature increases. This causes a strong increase of the thermal conductivity at high temperature. In the energy-dependent case, instead, the electronic thermal conductivity shows a weak temperature dependence, which is usually the case in experiments (Fig. 4.14). The behavior of the electronic thermal conductivity emphasizes the need for an improved description of scattering over that provided by the simple constant time. Indeed, a constant scattering time model overestimates the electronic contribution to the thermal conductivity, and this leads to a significantly underestimation of the ZT, consequently, it is appropriate to select a refined model, as ours, to obtain a better prediction.

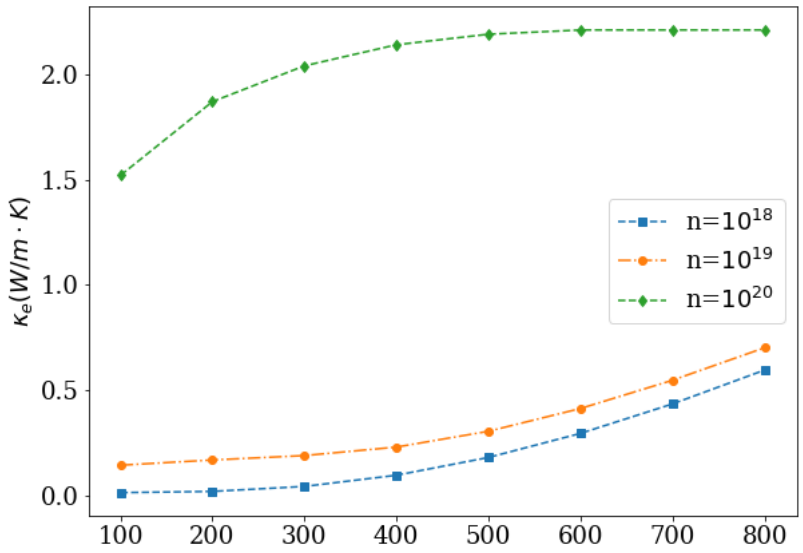

Fig. 4.13 Electronic contribution to the thermal conductiviy at different doping levels. The values above 10^{-19} cm^{-3} indicates a transition from a doped semiconductor to a metal behavior

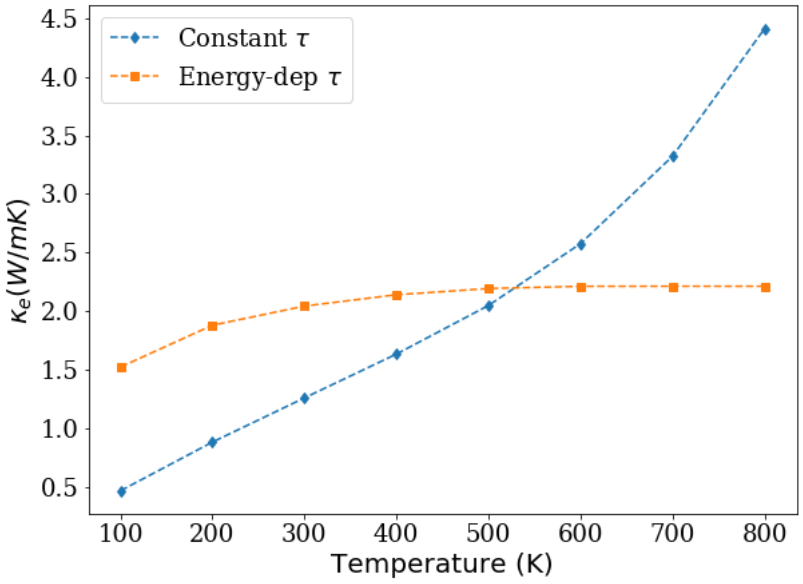

Fig. 4.14 Comparison between constant and energy dependent relaxation time for the electronic contribution to the thermal conductivity due at doping level 10^{20} cm^{-3} for a range of temperatures between 100 and 800 K. In the constant relaxation time approximation, κ_e becomes larger than in the energy-dependent case and rises sharply at high temperature, because of lack of the phonon scattering. In the energy-dependent case, instead, the total thermal conductivity shows a weakly temperature dependence.

Electrical conductivity

Turning now to the electrical conductivity σ, we found that doping values larger than 10^{19} cm^{-3} lead to a transition from semiconductor behavior to metal behavior, in agreement with [49]. This can be seen in Figs 4.15a and 4.15b, whereas the change in σ is a sign of a transition from a doped semiconductor to a degenerate-like behavior. There are several cases of alloyed MgSb samples with the same behavior as the nominal doping increases [49].
Considering a constant scattering time, the electric conductivity increases with temperature at dopings in the range between 10^{18} cm^{-3} and 10^{19} cm^{-3} , while in energy-dependent scattering time model, there is a decrease of σ with T above that doping level.

Seebeck coefficient

Seebeck coefficient is displayed on Fig. 4.16a and Fig. 4.16b for $\tau = \tau_0$ and $\tau = \tau(E,T)$, respectively. Above 10^{19} cm^{-3}, S increases monotonically with T, reaching values in the range of 150-250 μV/K. The values are consistent with previous work ([49], [50]). Considering the case with in the constant time approximation, the Seebeck coefficient is similar only at high doping both in behavior and values, contrary to what is seen for lower doping levels with a net underestimation of S in all the range of temperatures considered.
Again, the choice of a refined scattering model has an high impact on final results. Fig. 4.17 shows the Power Factor σS^2 for three different doping levels. The sharp decrease of electrical conductivity at high dopings (above 10^{19} cm^{-3}) is compensated by the Seebeck coefficient squared. The values for thermopower are poor: the sixfold conduction band bottom makes it possible to have a promising Seebeck coefficient but only a low electrical conductivity.

4.3.3 Figure of merit

In Fig. 4.18 ZT is plotted for different doping levels in the range of temperature between 100 and 800 K for the thermal conductivity given by the sum of electronic contribution and lattice contribution for the polycrystal material. The relaxation time τ used is the one shown in Fig. 4.12. From these data, we estimate the doping at which ZT is a maximum to be around 5×10^{19} cm^{-3} over all the considered temperature range. This is a typical doping level for electric applications (see Chapter 1) and relatively simple to get experimentally. In Fig. 4.19 is shown the figure of merit and its T dependence in the case of n-doped polycrystal which, as we will see, is the main reason of low κ_ℓ if we compare it with the case of a perfect crystal. For the same doping levels, the figure of merit assumes higher values in the polycrystal sample due to the lower κ_ℓ in this case. Looking at the same doping, 10^{19} cm^{-3} for example (filled circles for polycrystal, empty circles for crystal), ZT $\simeq$ 1.5 at T = 700 K: three times larger than in the crystal sample. The nanostructuring plays a decisive role in improving figure of merit. In Fig 4.20 it is shown ZT calculated neglecting the electronic thermal conductivity (red

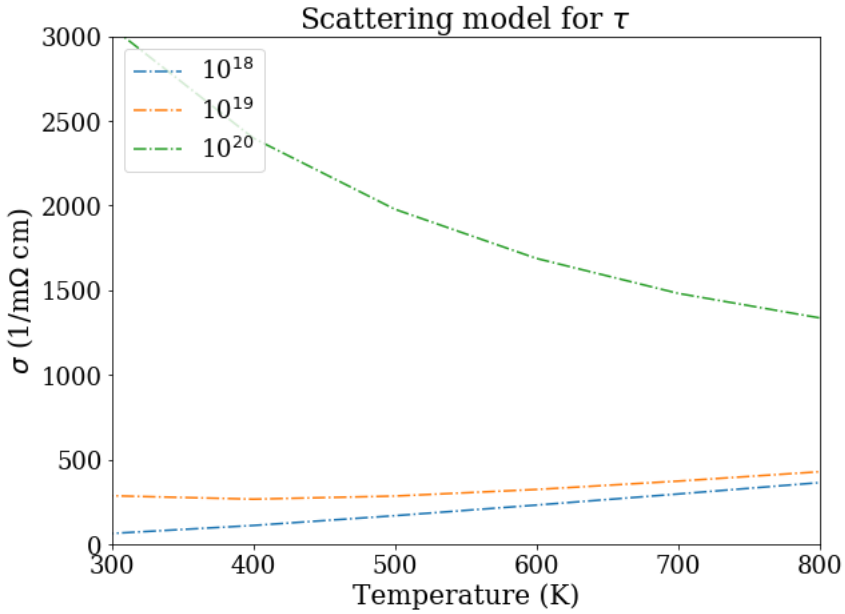

(a) – Electrical conductivity computed with energy-dependent scattering time. The doping level is indicated in labels in cm^{-3}.

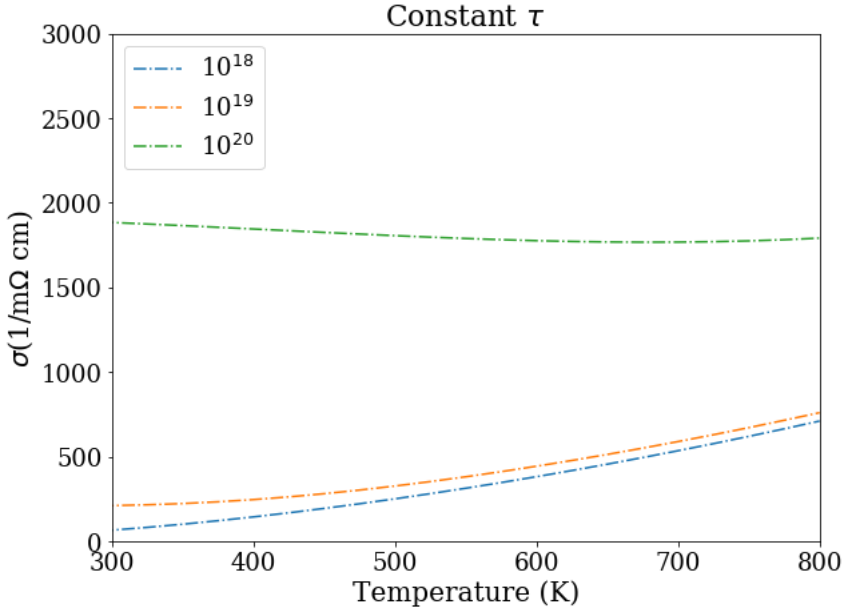

(b) – Electrical conductivity computed with constant scattering time. The doping level is indicated in labels in cm^{-3}.

Fig. 4.15 Electrical conductivity σ

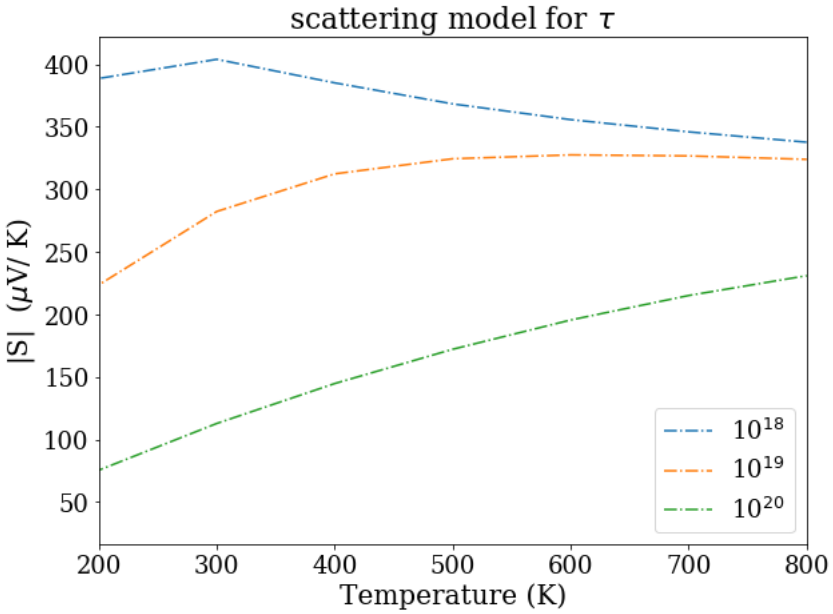

(a) – Absolute value of the Seebeck coefficient computed with energy-dependent. The doping level is indicated in the labels.

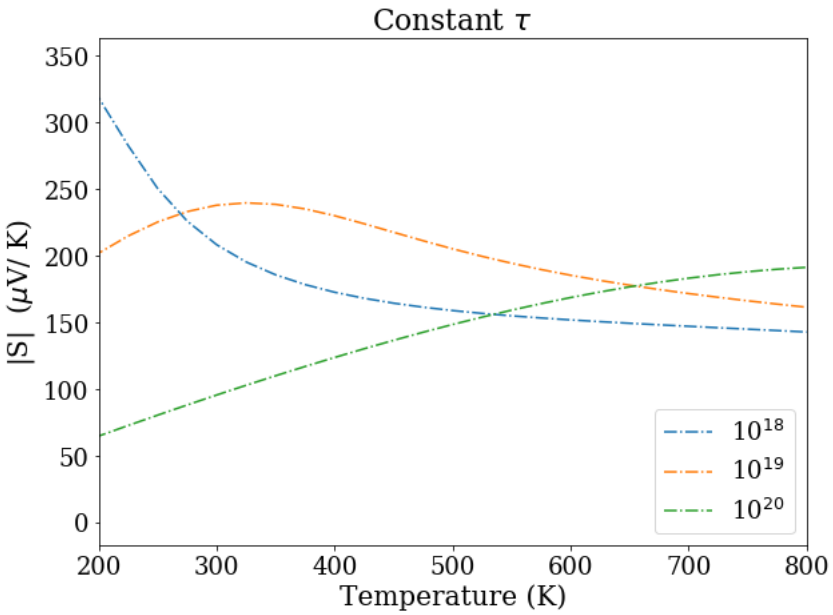

(b) – Absolute value of the Seebeck coefficient computed with constant scattering time. The doping is indicated in the labels. Seebeck coefficient is significantly lower than in the previous case especially at doping levels in the range between 10^{18} cm^{-3} and 10^{19} cm^{-3}. On the contrary, above this nominal doping, the chosen model for τ does not affect the Seebeck coefficient.

Fig. 4.16 Seebeck coefficient S

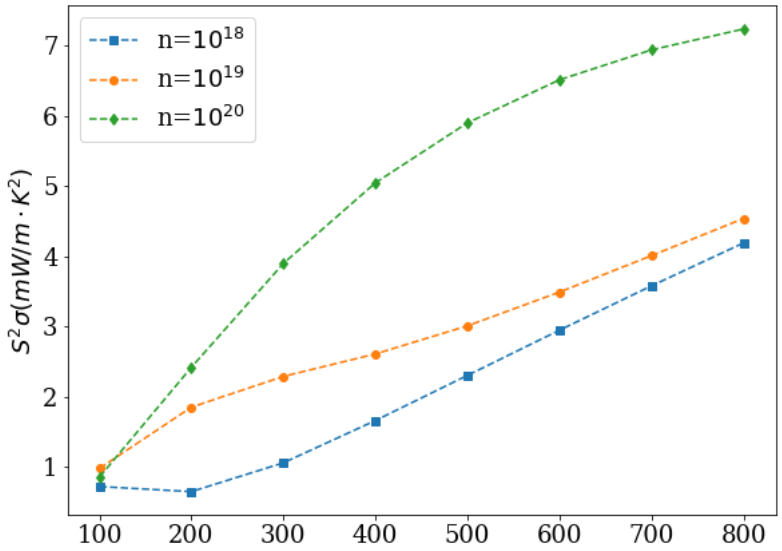

Fig. 4.17 Power Factor $S^2\sigma$ for different dopings (given in the labels) expressed in cm^{-3}.

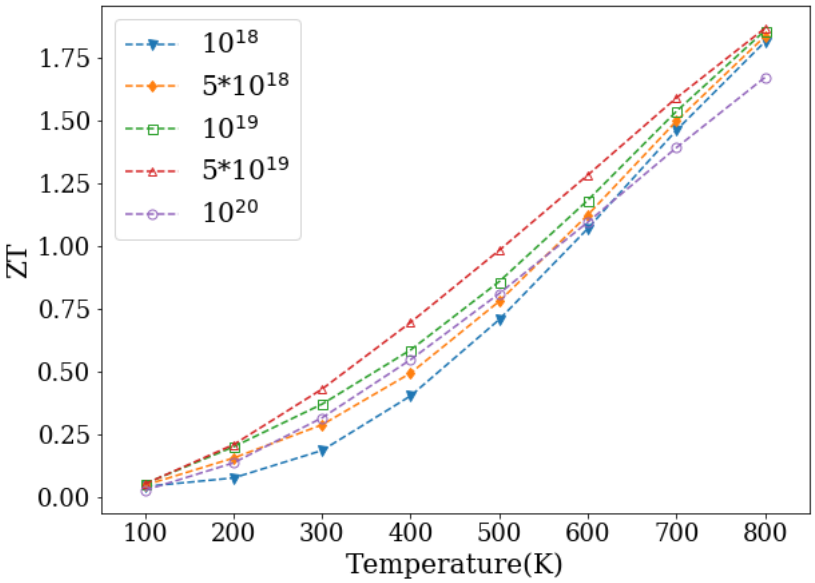

Fig. 4.18 Figure of merit at different doping levels for the range of temperature between 100 and 800 K. The thermal conductivity is estimated taking into account both the electronic and lattice contribution. The latter by considering the polycrystal sample. The n-doping level is indicated in the plot (units are in cm^{-3}). The maximum value for ZT is estimated to be about $5 \cdot 10^{19}$ cm^{-3} for each of temperautes considered.

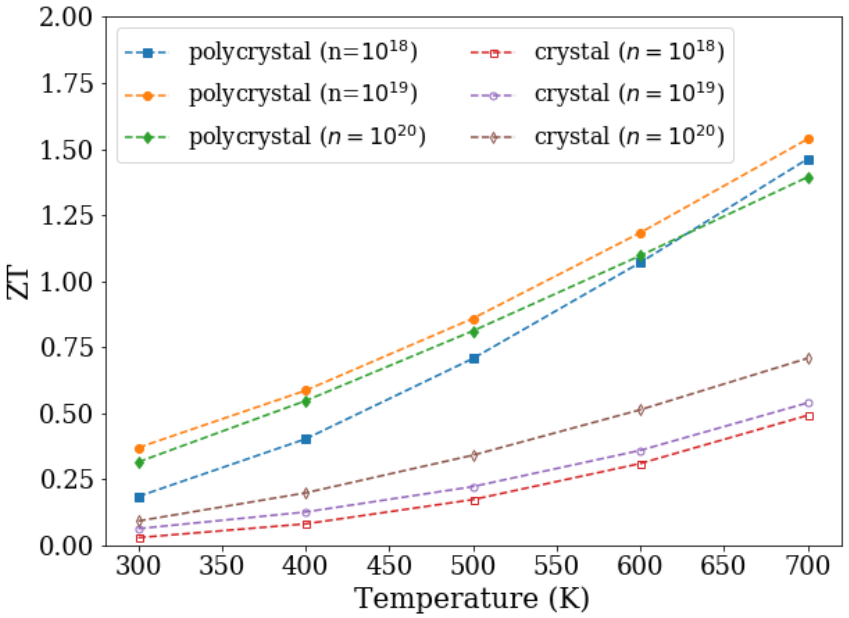

Fig. 4.19 ZT vs temperature for n-doping both in the polycrystal sample (indicated with filled symbols) and the single crystal (empty symbols) at different dopong levels. The value for the polycrystal material are larger as expected taking into account the difference on thermal conductivity in the two cases.

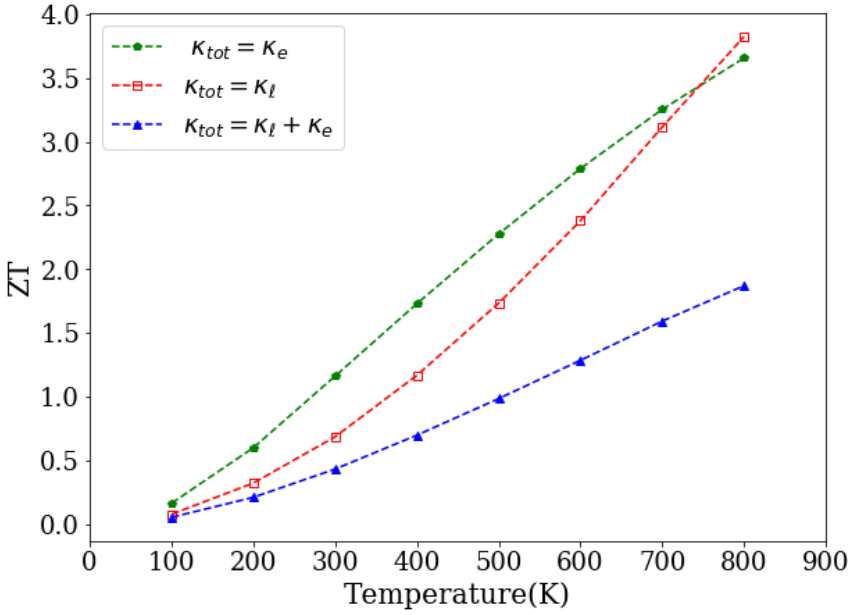

Fig. 4.20 Figure of merit ZT at optimal doping of $5 \cdot 10^{19}$ cm^{-3} taking into account only one of the two components of thermal conductivity. Neglecting one of the two contributions enhances artificially ZT, reaching values over 3 for T = 800 K.

empty squares), neglecting the lattice contribution (green circles) and considering both of them (in blue). The red dashed line explains the overly optimistic values of 2.5-3 reported in recent work [52], where electronic thermal conductivity was not included. Clearly, both the contributions to thermal conductivity have an impact on the ZT: neglecting one of them means overestimate figure of merit by more than a factor 2.

In any case, that is not the only important point to consider: the chosen scattering model has an equal relevance. In particular, the full ZT with a energy and temperature-dependent relaxation time approximation is compared with ZT in constant time approximation on figure 4.21. ZT reaches values around 1.6 in the considered range of temperatures, showing a good agreement with experiments for that material (figure 1(a) of [49]). The constant τ_0 case is about a factor of 2 smaller for high temperatures, mainly due to the larger increase in κ_e as temperature increases. This is not true in general. Depending on the material and on the choice of τ_0, the ZT for constant relaxation time can also be larger than with E-dependent τ (e.g. in the next Chapter). Finally, we compare our results

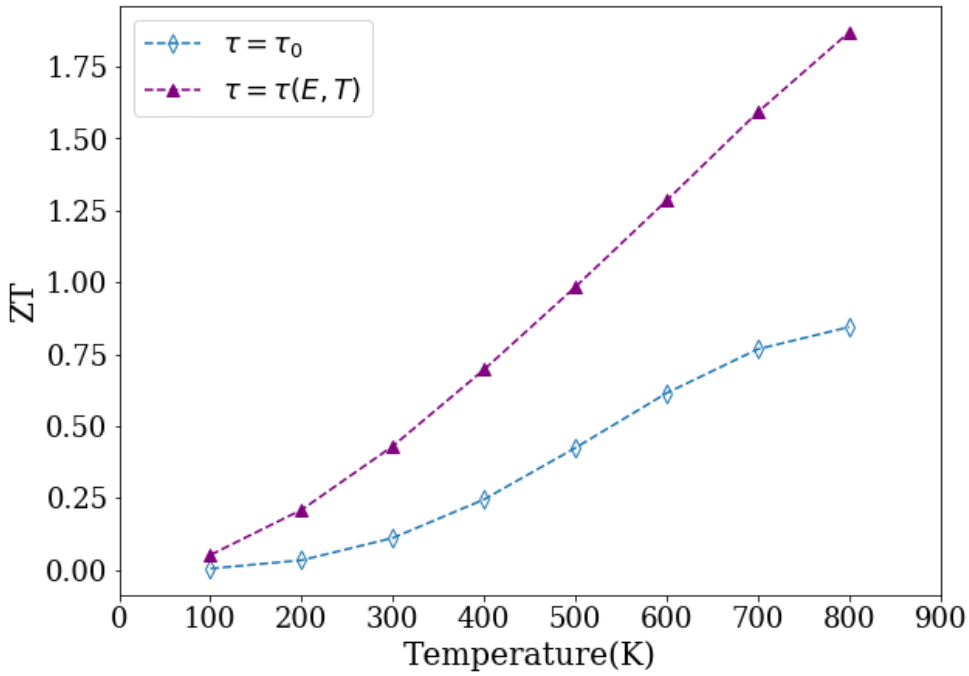

Fig. 4.21 Figure of merit for constant $\tau = \tau_0$ and for energy-dependent $\tau = \tau(E,T)$. The constant τ_0 case is about a factor of 2 smaller, and has a clear maximum in T , mainly due to the larger increase in κ_e with T in that case.

with experiment data from [49] in Fig. 4.22, to evaluate our model's consistency with experiment. Since the actual experimental doping level is not available, we compared experiments with three different calculations at three different nominal doping values. Our calculation underestimates ZT at low temperature and overestimates it at high temperatures [64] [65]. The value reached are in general good agreement with the experiments, and the ZT is in line with typical thermoelectric materials available today.

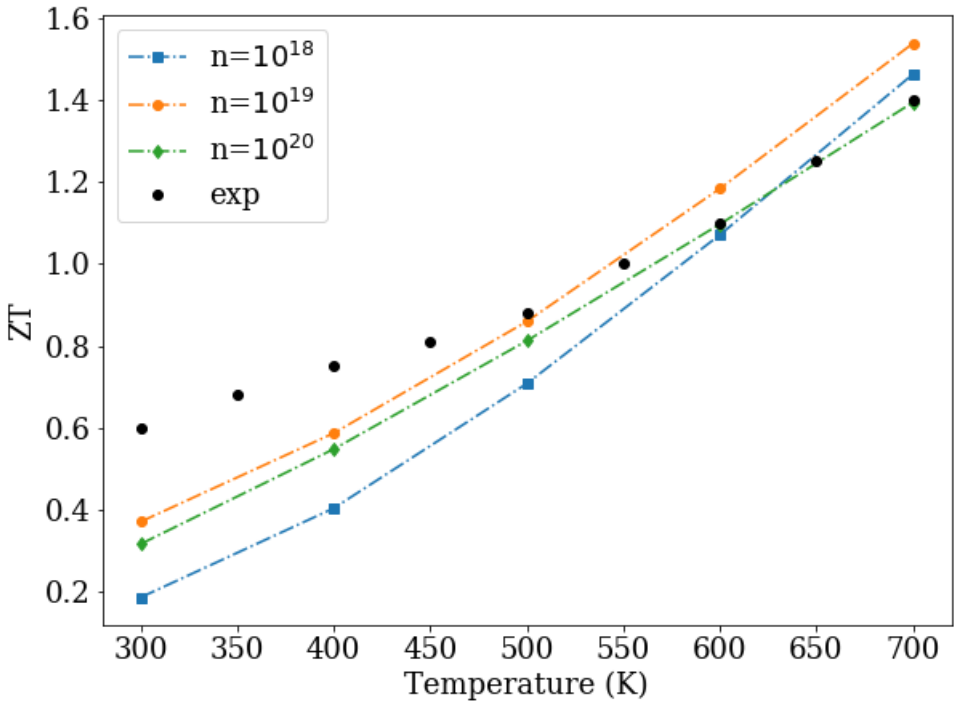

Fig. 4.22 Comparison of our calculated ZT with the values measured in Ref [49]. Since the doping level considered in the experiment is unknown, we cannot make the comparison with the exact doping. The values indicate a good agreement with experimental results with an overestimation of ZT at high temperatures and an underestimation at low temperature compared with experimental results.

4.3.4 Comparison between Vasp and QuantumEspresso electronic structure

Throughout the previous discussion, some doubts might arise on why two different codes (VASP and Quantum Espresso (QE)) are used in the calculations, and if their results may be mixed to compute the thermoelectric figure of merit. The answer is not simple, but the reasons behind this choice can be found on the different approaches and tool that VASP and QE offer.
Theoretically, it would be possible to compute phonons with VASP and to derive all anharmonic terms, instead of using QE; however, this would make the procedure very complicated for two reasons: firstly, QE tools that we used to calculate phonons and third-order derivatives are interfaced directly with QuantumEspresso outputs (dynamical matrix format), greatly reducing the time needed for post-production of data and, secondly, VASP derives phonons from finite differences calculations [4] and can compute only zone-center (Γ-point) frequencies [5]. In Quantum Espresso, Density Functional Perturbation Theory is implemented and the whole phonon spectrum can be easily computed.
At the same time, we could have calculated both electronic and lattice properties with QE. In this second case, the decision derives from a greater knowledge of VASP and the possibility to use BoltzTraP code as modified by our research group, directly using the EIGENVAL file from VASP calculations, thus, avoiding file format conversion from QE.
To ensure our method reliability, we compare results for electronic structures as the results of VASP (Fig. 4.23) and QE (Fig.4.24). Both the structures are relaxed in a trigonal P-3m1 space-group 164 structure. The optimized lattice parameters are:

Lattice Parameter	a (Å)	c (Å)
VASP	4.601	7.281
QuantumEspresso	4.587	7.273

Pseudopotentials: from VASP Pseudopotentials Repository:

Mg :	PAW_PBE Mg (2001)
Sb :	PAW_ PBE Sb (2000)

From Pslibrary - QuantumEspresso repository [66]:

Mg :	Mg.pbe-hgh.UPF
Sb :	Sb.pbe-hgh.UPF

Vasp and QE electronic band strcutures show remarkable agreement between them, allowing us to build confidence in our method. In addition, the lattice parameters differ only for 0.2 % despite different pseudopotentials employed in the calculation.

[4] Finite-difference methods (FDM) are a class of numerical techniques for solving differential equations by approximating derivatives with finite differences.
[5] https://www.vasp.at/wiki/index.php/Phonons_from_finite_differences

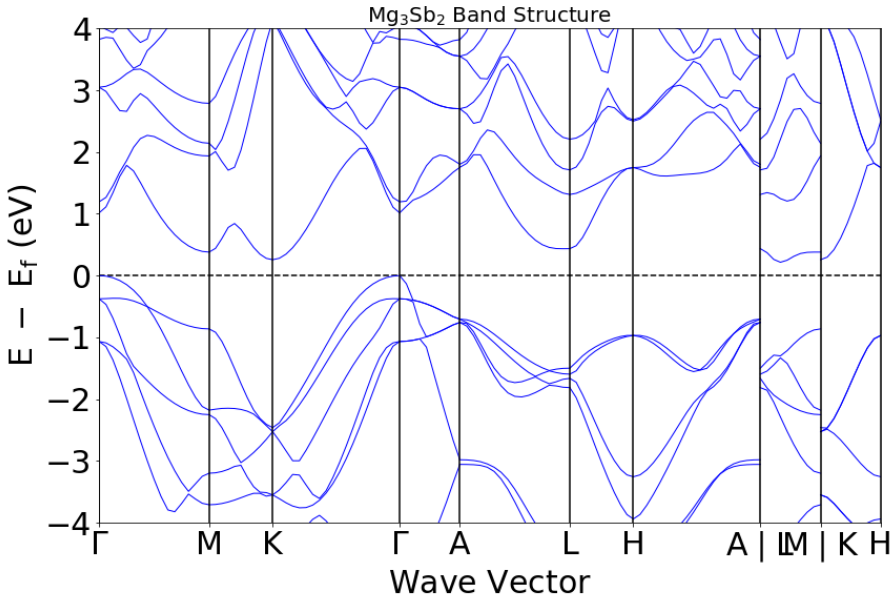

Fig. 4.23 Calculated GGA electronic band structure of Mg_3Sb_2 as obtained from Vasp. The dashed line through energy zero represents the Fermi level. The band structure is obtained by using the Python Library Pymatgen [93]

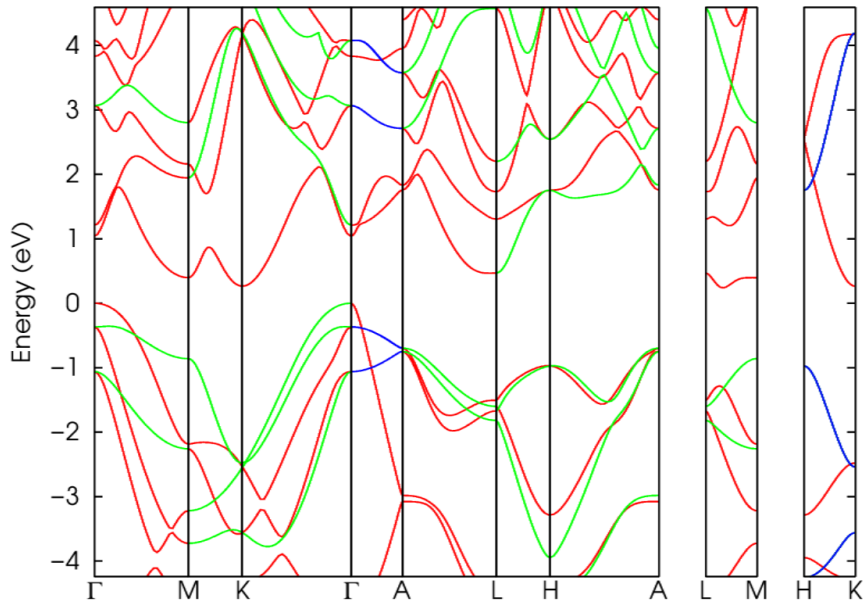

Fig. 4.24 Calculated GGA electronic band structure of Mg_3Sb_2 as obtained from Quantum Espresso. The band structure is obtained from thermo_pw [97] software.

Chapter 5

Layered perovskite $La_2Ti_2O_7$

In this chapter I report an *ab initio* study on layered perovskite $La_2Ti_2O_7$ belonging to the family of layered perovskite oxides $A_nB_nO_{3n+2}$. As in the previous chapter, we report the calculations for the electronic trasport coefficients as well as for the lattice thermal conductivity.

5.1 Perovskites

Materials with layered perovskite-related structures display several structural, chemical and physical properties [78]. Perovskite structures are adopted by many oxides that have the chemical formula $A_nB_nO_{3n}$. The idealized form is a cubic structure (Pm3m) which is rarely encountered. Barium titanate is an example of a perovskite which can take on the rhombohedral (R3m), orthorhombic, tetragonal and cubic forms depending on temperature (Fig. 5.1). Several compounds with the formula

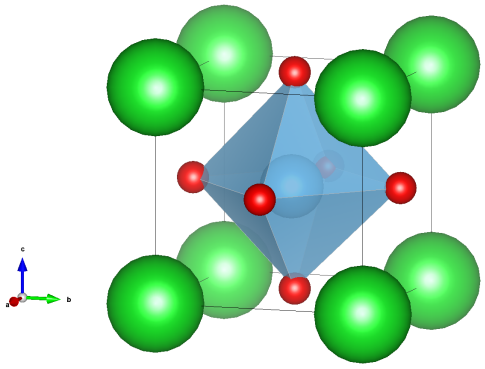

Fig. 5.1 Structure of rhombohedral (R3m) $BaTiO_3$. The red spheres are oxide centres, blue is the Ti^{4+} cation, and the green spheres are Ba^{2+}. The solid exists in one of four polymorphs depending on temperature. From high to low temperature, these crystal symmetries of the four polymorphs are cubic, tetragonal, orthorhombic, and rhombohedral crystal structure, respectively.

$A_nB_nO_{3n+2}$, such as $La_2Ti_2O_7$, do not form the expected isometric pyrochlore structure, as is typical for many of the heavy-rare earths and transition metal oxides, but rather form a layered structure comprised of slabs of the ABO_3 perovskite structure [71] [72] [73].

5.2 Crystal structure of Lanthanum titanate

The layered perovskite $La_2Ti_2O_7$ belongs to the homologous series $A_nB_nO_{3n+2}$ with $n = 4$. Fig. 5.2 shows the schematic crystal structure of $La_2Ti_2O_7$ projected along the [100] direction. The perovskite "slab" contains four layers of corner-sharing TiO_6 octahedra. The octahedra in different slabs are separated by layers of A-site cations, in our case made up of La.
Despite other doped perovskites having ZT at most 0.3 at high T [62], the layered variant LTO looks very promising for thermoelectric efficiency. One of the reasons is the conduction band behavior which leads to a rapidly rising density of states and, according to the Mott-Cutler formula [61], should produce a significant Seebeck coefficient. Moreover, the layered structure of peroskite blocks consisting of four perovskite octahedral units stacked along *a* [110] direction in cubic perovskite axes, as sketched in Fig.5.2, may be expected to avoid phonon propagation, much as a multi-interface structure, and lead to a reduced lattice thermal conductivity compared to normal perovskites. Recently, $La_2Ti_2O_7$ and other layered perovskites have received considerable attention because of their potential applications in fuel cell and other energy conversion technologies [75][76][78].

5.2.1 Methods

For the electronic coefficients (electrical and electronic thermal conductivity and Seebeck coefficient) we calculate the electronic band structure from first principles within density functional theory in the generalized gradient approximation, and then, use it to calculate the coefficients as functions of temperature and doping, in the relaxation-time approximation to the linearized Boltzmann transport equation, known as Bloch-Boltzmann theory [36][37][59][60]. We, then, use a T-dependent relaxation time to obtain ZT (Section 5.4). The lattice thermal conductivity is estimated with the Boltzmann equation applied to phonons which includes ab initio third-order anharmonic scattering, isotopic scattering, and Casimir finite-size boundary scattering (Section 5.3) as in the case of Mg_3Sb_2 as described in [47].

5.3 Lattice thermal conductivity

Lattice thermal conductivity, as we have already discussed in previous chapters, is an important ingredient to compute ZT. In the case of $La_2Ti_2O_7$ we chose to fix κ_ℓ to the value of 1.2 W/(m $\cdot$ K) and this value is T independent as observed in [82]. That choice can be justified considering the small and weakly T-dependent κ_ℓ.
Because a direct calculation of phonons and third-order dynamical matrices for this large unit-cell material is prohibitively costly, we computed the *ab initio* κ_ℓ of $BaTiO_3$ in a geometrically fixed configuration for the bulk material and for a 1.5 nm thick film, in such a way to have the individual perovskite block thickness of $La_2Ti_2O_7$. The choice to use this model is due to different reasons:

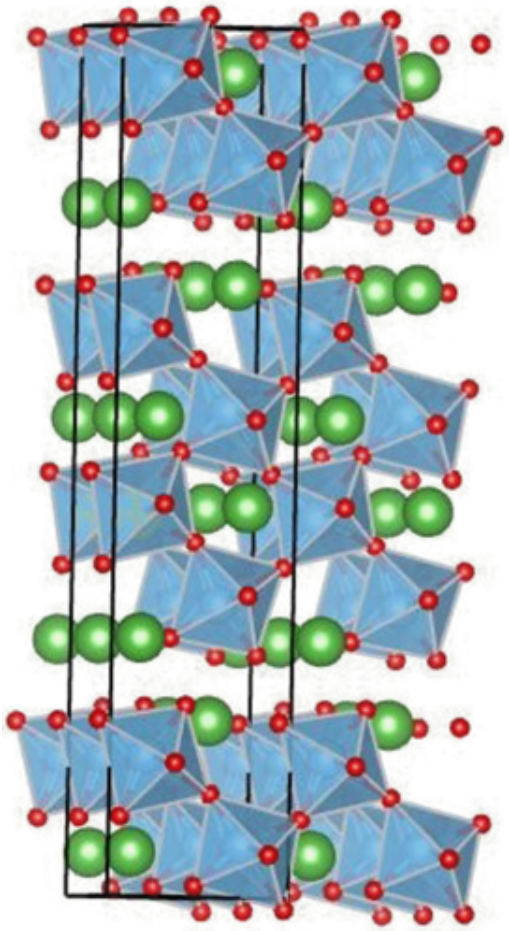

Fig. 5.2 Schematic crystal structure of $La_2Ti_2O_7$ projected along the [100] direction. The *a* axis points into the page, the *b* axis vertically, and the *c* axis from left to right. The primitive cell is outlined. The perovskite "slab" contains four layers of corner-sharing TO_6 octahedra. The octahedra in different slabs are separated by layers of La.

i Ba is mass-wise the closest element to La in the periodic table (excluding rare earths).

ii The local structure of both $BaTiO_3$ and $La_2Ti_2O_7$ are made up of TiO octahedra, and therefore most likely share the main vibrational features. In addition $La_2Ti_2O_7$ has internal interfaces which are modeled by Casimir term (Fig 5.1).

We have included anharmonic scattering, isotope-disorder scattering and Casimir boundary scattering in our calculation. The latter is:

$$P^{C}_{\mathbf{q},j,\mathbf{n}} = \frac{c_{\mathbf{q},j} \cdot \mathbf{n}}{F \cdot L} n_{\mathbf{q}j}(n_{\mathbf{q}j} + 1) \tag{5.1}$$

with n the equilibrium phonon occupations, L the film thickness and the correction factor F takes into account the width to length ratio of the sample. In our study, this value is put equal to 1. $c_{\mathbf{q},j}$ is the group velocity of mode j at wave vector $\mathbf{q}$ and $\mathbf{n}$ is the normal to the film [47] [83] [84] [85].
Thus, the anisotropy of the material is accounted for by projecting each phonon velocity along the short direction. Indeed, phonons traveling orthogonal to the plane of the film are scattered more then others, in fact they should be scattered proportionally to the projection wave vector and, at the same time, those in the plane of the film are not scattered at all.
The possible occurrence of mass disorder, which can be an important source of thermal conductivity reduction as already discussed in previous chapters, is not considered in this work because it does not appear to be significant in the high-quality material of Ref. [82]. Moreover, a similar κ_ℓ value has been found in the layered perovskite $Sr_2Nb_2O_7$ which is isostructural at $La_2Ti_2O_7$ [79] reinforcing the theory that the small value of thermal conductivity is due to a geometric cause.

5.3.1 Computational details for κ_ℓ

Similarly to previous Mg_3Sb_2, we employed the Quantum Espresso suite [27] [28] and its extensions [46] [47] to obtain κ_ℓ. Furthermore we did calculations with optimized pseudopotentials from PseudoDojo [87], the generalized gradient approximation [17] to density functional theory and a plane-wave basis cutoff of 100 Ry. We obtained the relaxed configuration in the ground state rhombohedral phase with an ($8 \times 8 \times 8$) k-points grid, D3Q [46] for the third-order anharmonic force constants on a ($4\times4\times4$) grid and TK code [47] for the phonon Boltzmann equation with a ($12\times12\times12$) grid and a δ-function width of 5 cm^{-1}. The isotope abundance is taken from NIST database [88]. Finally $BaTiO_3$ is assumed to have a low-T rhombohedral structure.

5.3.2 Results for κ_ℓ

I show in Figure 5.3 the inverse average of the κ_ℓ tensor for bulk $BaTiO_3$ and for a film with thickness 1.5 nm, given by considering the Casimir scattering for phonons in a single block of $BaTiO_3$. As you can see, the finite size causes a sharp decrease in κ_ℓ and largely suppresses its T dependence, with a value between 0.5 and 0.8 W/(m $\cdot$ K) throughout the temperature range. The value of the lattice

contribution to the thermal conductivity is remarkably low and, more importantly, the size reduction has an effect even in the plane, since the κ_ℓ tensor is essentially isotropic.
But, on the other hand, the literature reports a κ_ℓ for $BaTiO_3$ of 5 W/(m · K) at room T [77]. This suggests the presence of a systematic error of about 30% - 40 %, as in fact our estimation for the bulk of $BaTiO_3$ is underestimated by about 30% - 40 %. To overcome this problem, we have set κ_ℓ = 1.2 W/(m · K).
This is in fair agreement with experiment, and supports the idea that the low lattice thermal conductivity of $La_2Ti_2O_7$ is due to the effective confinement of phonons within the stacked blocks of the layered structure. If we used our theoretical κ_ℓ , ZT could be slightly higher at high temperature, due to the slight decrease of κ_ℓ with T.

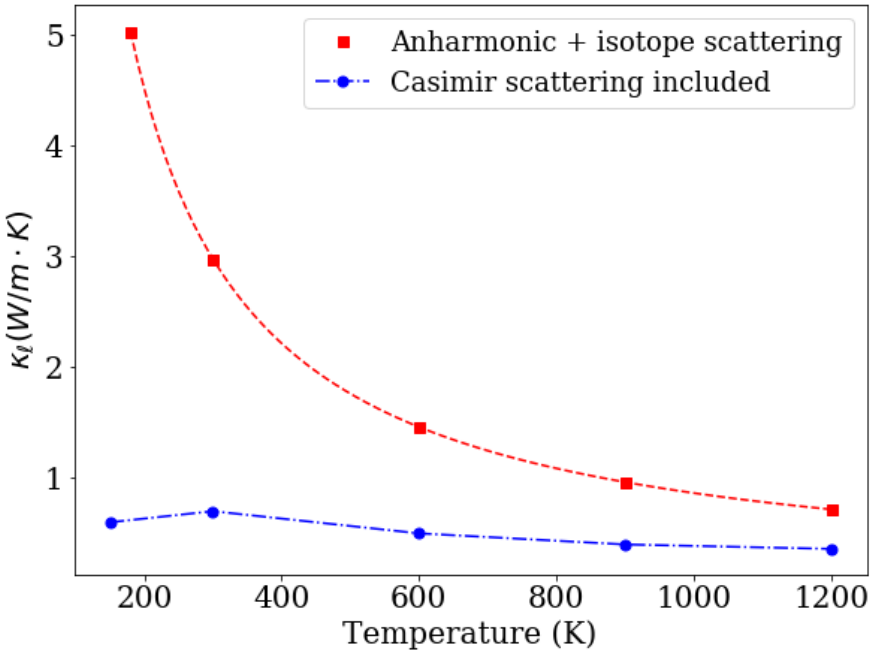

Fig. 5.3 Average of the κ_ℓ tensor for bulk $BaTiO_3$ and for film like $BaTiO_3$ with thickness 1.5 nm (i.e. the thickness of a perovskite block in $La_2Ti_2O_7$). The finite size causes a sharp decrease in κ_ℓ, and largely suppresses its T dependence.

5.4 Electronic parameters

5.4.1 Computational details

Ab initio calculations are performed within the generalized gradient approximation using the VASP code and the projector augmented-wave (PAW) method, with the maximum suggested cutoff and the PAW data sets for La, Ti_{pv} and O_s .
The structure of the orthorhombic phase of $La_2Ti_2O_7$ with spacegroup $Cmc2_1$ is optimized following quantum forces and stress. The computed lattice constants are:

a (Å)	b (Å)	c (Å)
3.915	25.851	5.643

The electronic eigenvalues are calculated ab initio on a (24×48×16) k-points grid.
Fig. 5.4 reports the electronic density of states for $La_2Ti_2O_7$ from -10 eV to 10 eV around the Fermi level, while in Figure 5.5a and 5.5b I reported the electronic band structure (in blue the La states, in green O states and in red the Ti states). The conduction band minimum is at the Γ-point, while the valence band maximum is along the X-Γ direction (0.167,0,0). The minimum gap (indirect band gap) in GGA is 2.85 eV and becomes about 4.1 eV by applying the correction of Ref. [67]. In any case, the energy gap is not important for the purpose of our calculations according to Bloch-Boltzmann model which depends only (or mainly) on the band where Fermi level lies [1].
The contribution to the conduction band is dominated by Ti states, while the oxygen dominates the valence band. The La states are not relevant for the electronic behavior. This suggests us that $La_2Ti_2O_7$ could be used in alloys with other compounds with the same electronic properties, as for example $Sr_2Nb_2O_7$, recently emerged to be a promising thermoelectric material [68].
Electronic coefficients are calculated with the BoltzTrap2 [59] [60] code. We assumed the ab initio bands are not changing with doping or temperature, in the so-called rigid bands approximation [2]. Then bands are interpolated by a Fourier-Wannier technique over a number of k-points given by the original number of points times an amplification factor, which we choose to be A = 64, approximately equivalent to a much finer (96×32×64) grid.

5.4.2 T-dependent relaxation time

ZT must be obtained from the various coefficients under some hypothesis for the relaxation time. Figure 5.6 shows the relaxation time as a function of energy (at fixed T = 300 K) and temperature (at fixed E = 0.043 meV).
The energy and temperature relaxation time is obtained from the rates of impurity, acoustic phonon,

[1] More specifically, it is true that, at high temperatures, states across small gaps can be involved in the transport coefficients, but this is not relevant here given the large gap.

[2] In rigid band approximation (RBA) it is assumed that doping a system does not change the band structure, only the chemical potential changes with doping concentration. This model is valid when low doping concentrations n are considered, namely $n < 10^{21}$ cm^{-3}.

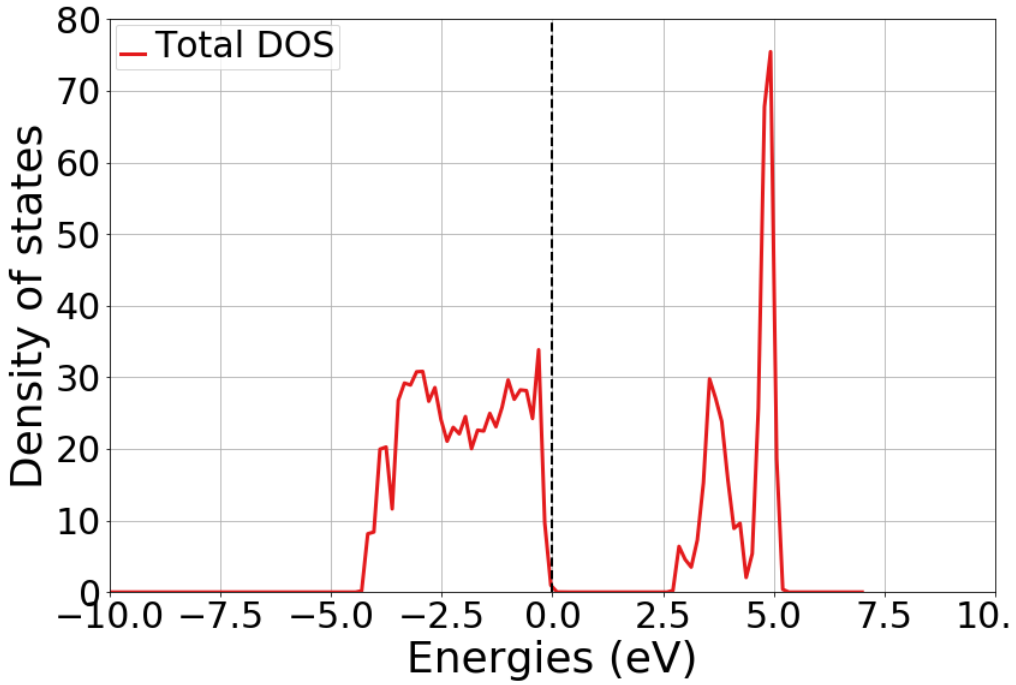

Fig. 5.4 Density of States (DOS) as a result of a GGA calculation with Vasp. The dashed line through energy zero represents the Fermi level. Band-gap is estimated to be 2.87 eV.

and polar phonon scattering:

$$\tau(E,T) = \frac{1}{P_{ac} + P_{imp} + P_{polar}} \tag{5.2}$$

where the rates are given by equations in chapter 3.

Actually, if lattice thermal conductivity was equal to zero, since electrical and electronic thermal conductivity can be determined as: $\sigma_0 = \sigma/\tau_0$ and $\kappa_{e,0} = \kappa_e/\tau_0$, ZT would be independent of relaxation time. But this is not our case, so we should estimate ZT as:

$$ZT_0 = \frac{S^2\sigma T}{\kappa_e + \kappa_\ell} = \frac{S^2\sigma_0\tau_0 T}{\kappa_{e,0}\tau_0 + \kappa_l} \tag{5.3}$$

which depends strongly on the choice of τ_0. Here, a fixed relaxation time neglects the physically relevant temperature dependences due to phonon occupation changes and energy averaging. To obviate this shortcoming, we calculate:

$$ZT_{ave} = \frac{S^2\sigma_0\tau_{ave}T}{\kappa_{e,0}\tau_{ave} + \kappa_\ell} \tag{5.4}$$

with an average relaxation time given by [69]:

$$\tau_{ave} = \frac{\int_0^\infty \tau(E,T)E^{3/2}(-\frac{\partial f_F(T,E)}{\partial E})dE}{\int_0^\infty E^{1/2} f_F(T,E)dE} \tag{5.5}$$

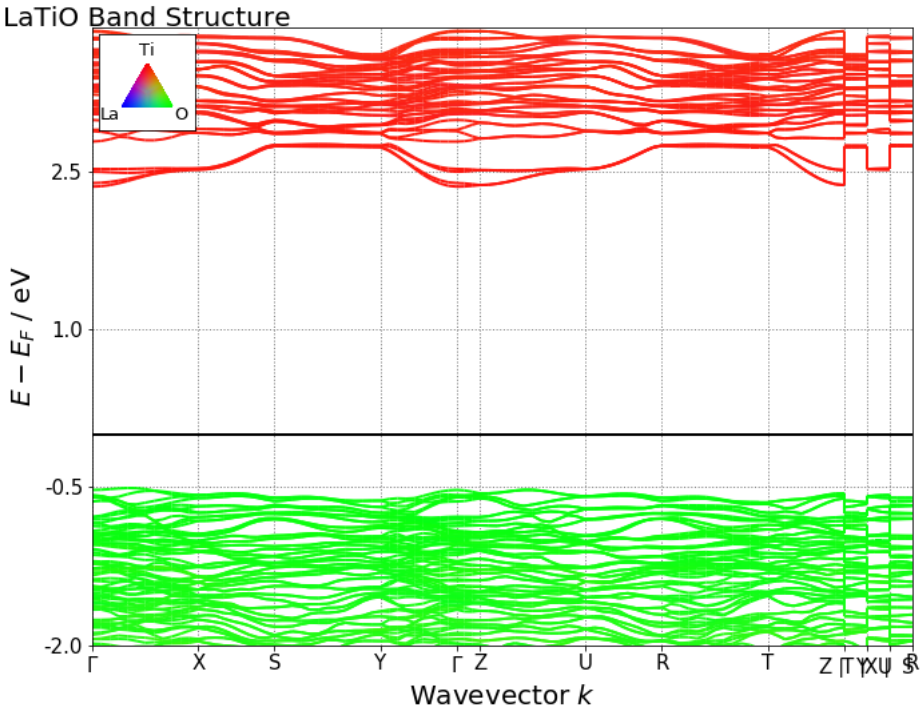

(a) – The GGA generated band structure of $La_2Ti_2O_7$ near the Fermi level highlighted in black.

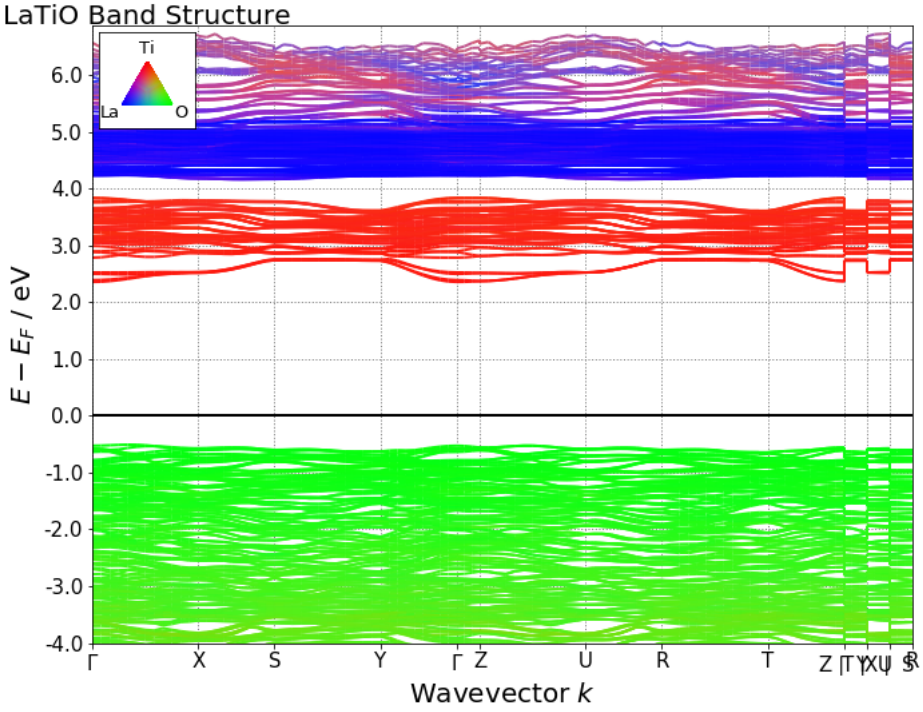

(b) – The GGA generated band structure of $La_2Ti_2O_7$ as obtained from Vasp calculation. The black line through energy zero represents the Fermi level.

Fig. 5.5 Bandstructure of $La_2Ti_2O_7$

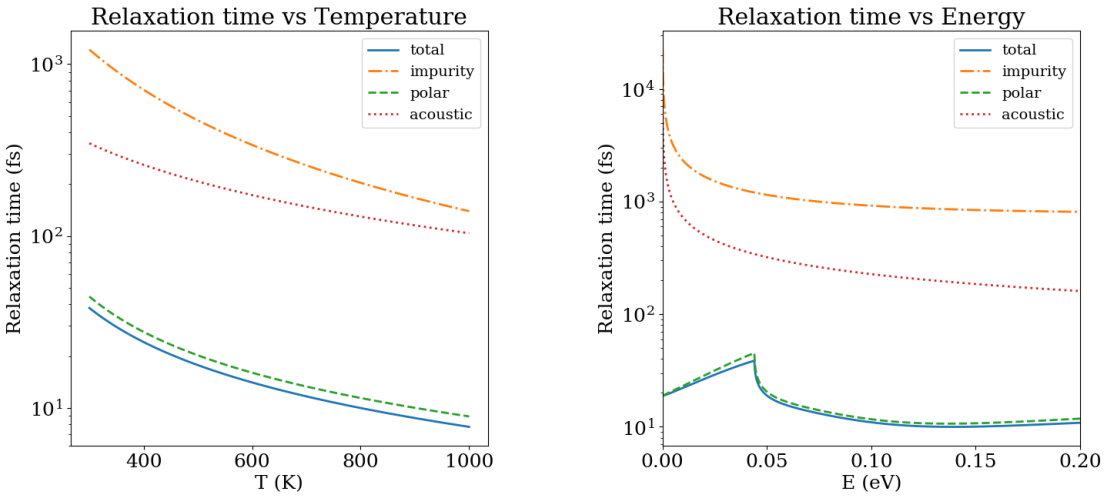

(a) **(b)**

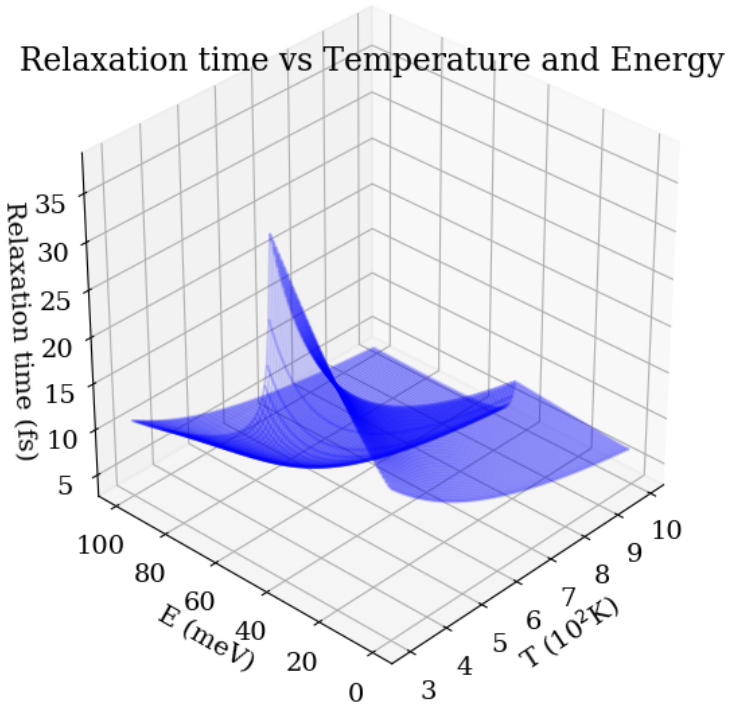

(c)

Fig. 5.6 The relaxation time behavior vs temperature and energy considering different scattering mechanisms described in chapter 3 and the total relaxation time given by formula 5.2. **(a)** Relaxation time in function of temperature at fixed energy of: 0.043 eV. **(b)**Relaxation time in function of energy computed at T = 300 K. **(c)** Total $\tau = \tau(E,T)$

The $\tau(T)$ behavior for the averaged energy is shown in Figure 5.7. This average is obtained in a parabolic band approximation, but can be generalized easily.

By using an energy-averaged time we are assuming that τ does not vary with E; since typical electron

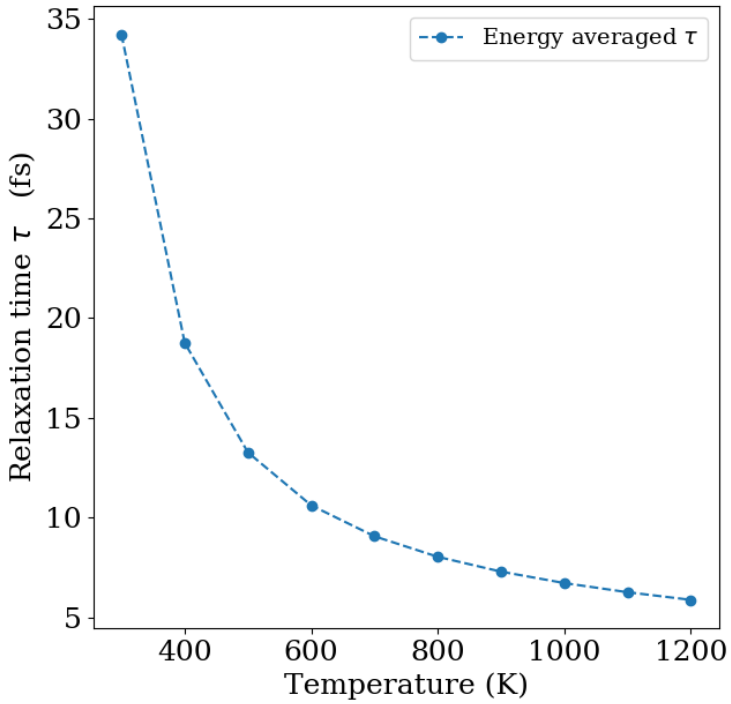

Fig. 5.7 Energy-averaged scattering time versus temperature obtained in a parabolic band approximation.

energies are in the low-energy region, below 30-40 meV from the band edge where $\tau(T,E)$ is large, our averaging over all energies will tends to underestimate the relaxation time and consequently gives a smaller estimates of ZT. Although this procedure represents an improvement over the constant-time approximation: indeed, using a constant relaxation time means that Seebeck coefficient does not depend on τ , which is not generally true: to convince yourself of this, it is enough just to take a look at Chapter 4 and the trend for S obtained with a constant τ and compare it with the values for $\tau(E,T)$ [3]. To compare our results with constant relaxation-time results, various quantities are recalculated with a constant time chosen to be equal to the energy-average time at room T (34 fs as shown in figure 5.7).

[3]Despite being a much better approximation that a constant-relaxation time, a T-dependent but E-independent relaxation time will still factor out of the Seebeck coefficient, which will therefore not depend on τ. This is not generally true, as was shown in Chapter 4.

5.4.3 Parameters used in calculations

Since the most interesting feature is the thermoelectric transport along the *a* direction because it results to be the most efficient one, let us put our attention on it.
Before starting the analysis it is relevant doing two considerations: the spontaneous polarization points along the *c*-axis so any field coming from that source does not affect the transport along *a* direction. Moreover, the matrix element of piezoelectric electron-phonon scattering is proportional to the *a* component of dielectric displacement as reported in [38], but is zero by simmetry [70] [72] [73].
To compute our calculations, we imported some parameters from previews experiments:

- high-frequency dielectric constant[4] : $\varepsilon_\infty = 5$.
- lattice dielectric constant : $\varepsilon^{ii}_{lattice} = (62, 44, 65)$ found on [75]
- average sound velocity : $v = 5.2\ km/s$ found on [79]
- density : 5879 kg/m^3 found on [80]
- effective conduction mass: $m^*_c = 0.2m_e$ and valence mass $m^*_v \approx m_e$.
- dominant longitudinal optic (LO)-phonon frequencies obtained from the estimation of zone-center transverse optical (TO) frequencies via a frozen-phonon VASP calculation, and thence the LO frequencies by the Lyddane-Sachs-Teller relation with the T = 0 theoretical [75] lattice dielectric constants. We include in the scattering rate only the lowest LO mode with polarization along the *a* axis, which affects transport in the *a* direction [5]: $\hbar\omega_{LO} = 58meV$.

5.4.4 Results for *n*-doping

We concentrate on n-type doping, compared with less efficient p-doping shown below in Figure 5.13. As previously said, because the largest ZT tensor component is given by *a* component of various tensors, while the others are much smaller, since they produce a much smaller ZT, we concentrate our analysis on it. In our T range, which we chose to be 300-1200 K, to avoid getting too close to the ferroelectric transition at 1770 K for this material, the lattice thermal conductivity is only about 1 W/(K · m) and almost T-independent. As a result, we find that the figure of merit increases monotonically from over 0.7 at room temperature to over 2.5 at 1200 K within a T-dependent scattering-time approximation; the results are summarized in Figure 5.8.
The interesting ZT is obviously the result of combined factors: a large value of Seebeck coefficient, a

[4] Authors on [74] report $\varepsilon_\infty = 6 - 6.5$ for titanates with similar electronic structures and gaps. For $La_2Ti_2O_7$ no measurements seem to be available, so we conservatively pick a lower value, as due to effective phonon confinement within the overestimate polar phonon scattering, and produce slightly lower ZT.

[5] Lyddane-Sachs-Teller relation [81]:

$$\frac{\omega^2_{TO}}{\omega^2_{LO}} = \frac{\varepsilon_0}{\varepsilon_\infty}$$

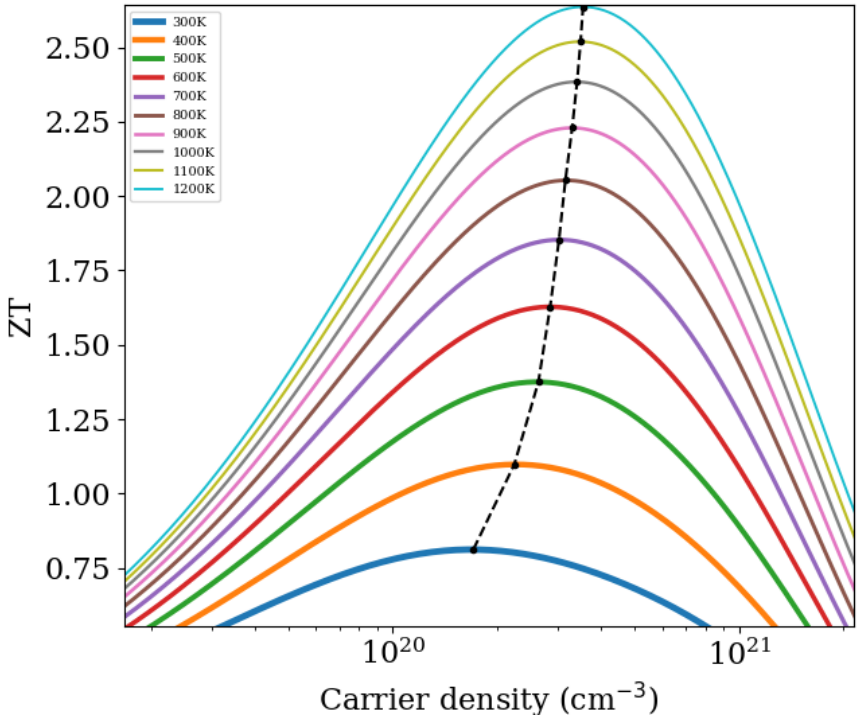

Fig. 5.8 The *a* component of the ZT vs n-type carrier density for temperature between 300 and 1250 K (line thickness increases as temperatures decreases) in steps of 100 K. The dashed-line extends to the whole temperature range and indicates maximum values of ZT at each T. The optimal doping level is about 3×10^{21} cm^{-3}.)

low thermal conductivity given by the combination of the electronic and the lattice contributions, and a significant electrical conductivity. Let us discuss now those single quantities.
All computed quantities, i.e. Seebeck coefficient in absolute value, eletrical and thermal conductivities, are displayed as function of excess *n*-type carrier density as solid lines.
To represent the different temperatures, the line thickness decreases as T increases in step of 100 K. For each temperature, dashed-dotted lines indicate the value of each quantity at the optimal doping, or, in other words, the value at which ZT is maximum, hence the maximum theoretical efficiency in a thermocouple is assumed to be at that doping level.
The optimal carrier density is by definition the density at which the maxima of ZT occur. Optimal doping is clearly between 1 and $3 \cdot 10^{20}$ cm^{-3} ; of course it remains to be seen if such doping densities can be achieved experimentally.
The Seebeck coefficient is between about 200 and 300 μV/K. In that regard, it is interesting to note that the Seebeck coefficient can achieve much larger values at lower doping, in particular, over 400 μV/K at 10^{19} cm^{-3} at room T; increasing T, Seebeck reaches even larger values (Fig. 5.9a). This is clearly interesting for applications requiring just a large S, as this relatively low doping should be fairly easy to achieve.
For the electrical conductivity (Figure 5.9b), we obtained values in the range of 40-100 kS/m which results in a resistivity about 10-25 $\mu\Omega$m.
Passing finally to the electronic thermal conductivity, figure 5.9c shows an almost T -independent total thermal conductivity with a value lower than 1 W/(m K) in the range of temperatues considered. It is interesting to note that this happens despite the strong decrease in relaxation time with temperature. With these results for the electronic contribution, total thermal conductivity reaches values of about 2 W/(m· K), very acceptable values for thermoelectric applications.
In figures 5.10a, 5.10b, 5.10c I represented the various components for Seebeck, electrical and electronic thermal conductivity as a function of temperature at optimal doping level, provided from data plotted in Fig. 5.8.
As it can be seen, *a* component is much larger than the others. In the case of Seebeck, around 20 %, but for conductivity along *a* appears to be of an order of magnitudo larger than conductivity along *b* and *c*. This is due, precisely, to the layered structure of our perovskite.
In figure 5.11 is shown the comparison between ZT computed with a constant relaxation time and a T-dependent relaxation time. As it can be seen, since $\tau(T)$ decreases monotonically with T, by using a constant relaxation time, the dominant component of ZT is much larger at high temperature for the constant relaxation time approximation, reaching 5 at 1200 K, while ZT$_a$ computed with $\tau(T)$ approaches 2.5 at 1200 K. Once again we can see the inadequacy of a constant τ to evaluate ZT and the need for a more refined scattering model.
In our calculation, the T dependence of the phonon frequencies and the increase of static dielectric constant with temperature were not taken into account thereby causing underestimation of longitudinal optical frequencies. That results in a possible over-estimation of relaxation time used. As a result, ZT$_a$ could be lower than the real value at high temperatures [86]. Moreover, phonons with polarization

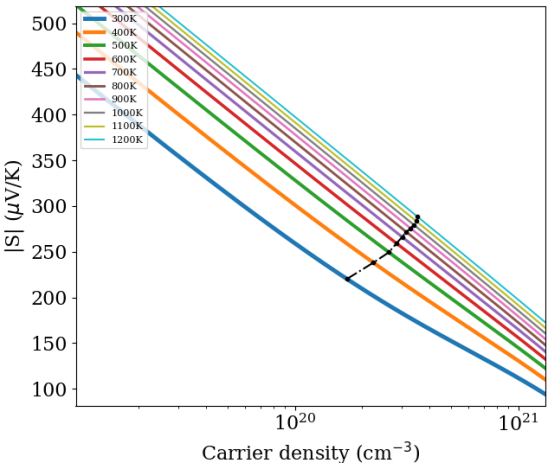

(a) – Seebeck coefficient as function of doping level for different temperature between 300 and 1200 K. $|S|$ between roughly 200 and 300 μV/K at optimal doping.

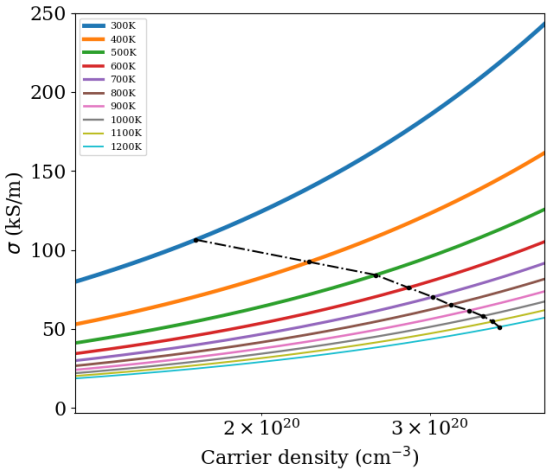

(b) – σ as function of doping level for different temperature between 300 and 1200 K. Significant conductivity of roughly 40 - 100 kS/m.

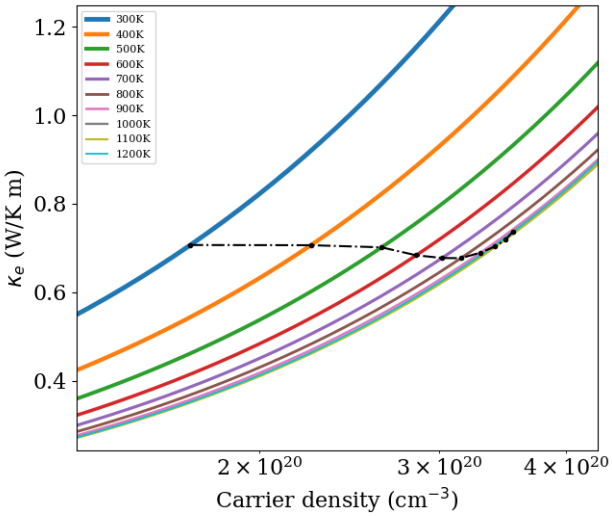

(c) – κ_e as function of doping level for different temperature between 300 and 1200 K. It is broadly constant with doping.

Fig. 5.9 Transport coefficients vs Temperature and doping.

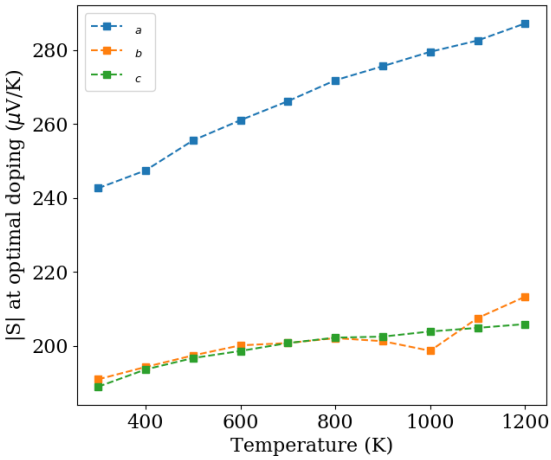

(a) – Absolute value of Seebeck coefficient vs temperature at optimal n doping for each T in the range between 300-1200 K. The a-component is the component which stacking occurs.

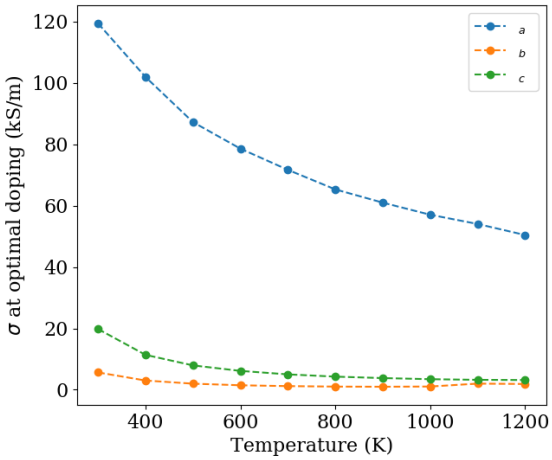

(b) – Electrical conductivity σ vs temperature at optimal n doping for each temperature. The a-component is 6 times larger than the other two components for the range of temperatures considered.

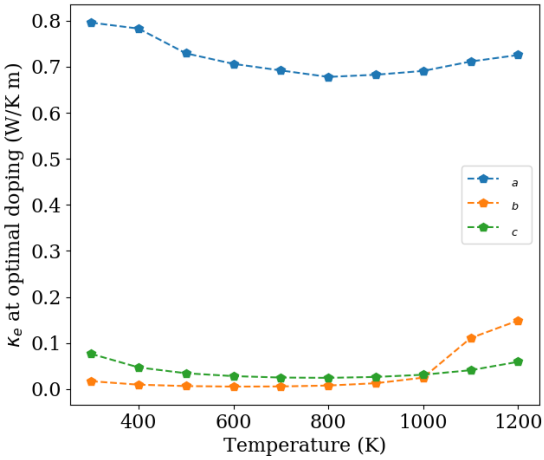

(c) – Electronic thermal conductivity κ_e vs temperature at optimal n - doping for each temperature. Although the component along stacking direction is considerably larger than b- and c-components, the values reached are low: between 0.7 and 0.8 W/(m · K).

Fig. 5.10 Transport coefficients vs Temperature at optimal n-doping

along b or c are slightly lower in energy, and will reduce further the b and c components of ZT , which in any case are small.

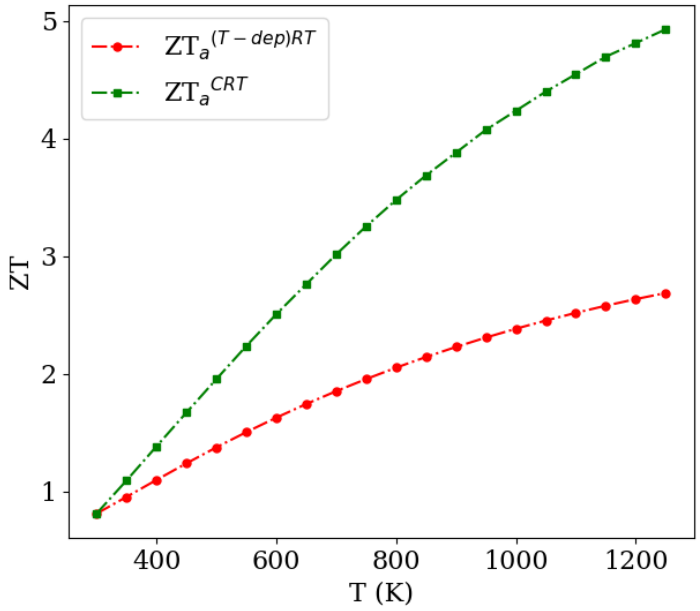

Fig. 5.11 Comparison between ZT_a (dominant component) computed with a constant relaxation time (CRT) and a T-dependent relaxation time at optimal doping level. With CRT we obtain values 2 times larger than in the case of $\tau(T)$.

5.4.5 Results for *p*-doping

The potential of LTO in the p-type case is less remarkable than in the n-type case. In fact ZT only reaches about 0.7 in the best instance (against we find that the figure of merit increases monotonically from over 1 at room temperature to over 2.5 at 1200 K within a T-dependent scattering-time approximation for n-doping as we have already seen). Moreover the optimal doping is higher for p type: the a component requires carrier densities in the high 10^{20} cm^{-3} range, and the other components requires carrier densities in the mid of 10^{21} cm^{-3}.
Anyway, the practical feasibility of p doping remains to be ascertained.

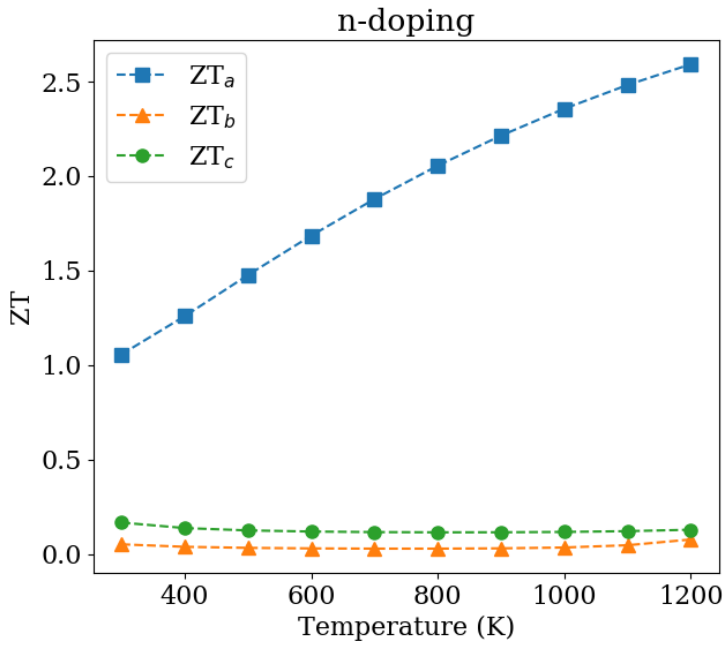

Fig. 5.12 ZTs components versus temperature at optimal n- doping. The *a* component requires carrier densities around 3×10^{20} cm^{-3}, slightly higher for *b* and *c* components which are negligible when compared with *a* component.

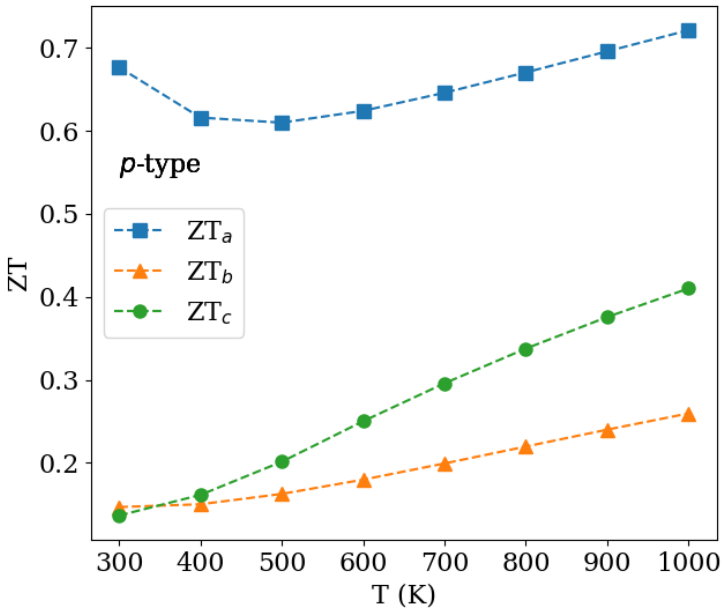

Fig. 5.13 ZTs components versus temperature at optimal p- doping. The *a* component requires carrier densities in the high 10^{20} cm^{-3} range, while the optimal doping level is about 5×10^{21} cm^{-3} for *b* and *c* components. Values are significantly lower than in n-type $La_2Ti_2O_7$.

Chapter 6

LaSO

6.1 High-Throughput

Obtaining materials with properties that are optimized for a particular application is at the core of materials science. However, materials development traditionally relies on time-consuming and expensive experimental work and theoretical support, though extremely valuable, can be sometimes unproductive due to the sheer size of the parameter space to be explored. High-throughput materials prediction has emerged as a tool for screening large databases of materials, to identify candidate materials that may have optimized properties for subsequent experimental evaluation.
High-throughput screening (HTS) is a method for scientific experimentation especially used in drug discovery and relevant to the fields of biology and chemistry. This idea is really starting to catch on material science in order to find new promising materials: using data processing/control software, high-throughput screening allows a researcher to quickly conduct millions of tests on almost any kind of material. Through this process one can rapidly identify compounds with a particular desired property. The results of these tests provide starting points for material discovery [91].
Computational power has enabled materials design to evolve from trial-and-error towards more systematic methodologies that require large amounts of both experimentally and computationally derived data, consequently, reseachers developed designed and developed tools and their underlying databases in order to facilitate modern-day high-throughput computational methods.
Moreover modern high-performance computing has allowed the simulation of crystalline materials and their properties on a huge scale, allowing the construction of large computational materials databases. One of these, Materials Project [92], contains more than 86,000 inorganic materials.
In this work, we used HT methodologies applied to thermoelectricity: we derived from MP Database material parameters that are helpful to predict the promise of a material for use in a thermoelectric device. A recent paper [89] has proposed a synthetic figure of merit to asses the promise of a potential thermoelectric based on computed or measure properties more easily accessible than those entering the actual ZT figure of merit. Specifically, for typical semiconductor transport with a scattering rate given by acoustic phonons in the so called deformation potential scattering, the thermoelectric quality

factor B is:

$$B = \frac{2k_B^2 \hbar N_v}{3\pi m_c^*} \frac{C_l}{\kappa_\ell \Xi^2} T \tag{6.1}$$

Here, k_B is the Boltzmann constant, $\hbar$ the reduced Planck constant, N_v the number of degenerated valleys for the band, m_c^* the conductivity effective mass while Ξ the deformation potential coefficient which is by definition the change of band energy (ΔE) per relative volume change (ΔV) of the crystal. Finally the average longitudinal elastic modulus C_l is equal to:

$$C_l = \frac{1}{5}(3C_{11} + 2C_{12} + 4C_{44})$$

taking into account that C_{ij} is the matrix of the elastic moduli tensor.
Some of these materials properties showed up here are the conductivity effective mass and the valley degeneracy. As already mentioned in the previous chapters, electrical conductivity can be approximated in the simplest way as:

$$\sigma = \frac{ne^2\tau}{m^*}$$

and hence, the smaller the conduction effective mass, the larger the electrical conductivity.
Furthermore:

$$\sigma \sim \frac{1}{N_v}$$

due to electron-electron scattering. Thus, considering Eq. 6.1 for S [1], we would expect the power factor to grow approximately linearly with N_v.
But many of the best thermoelectric materials have been recognized to have high valley degeneracy, including lead and tin chalcogenides [89] and Zintl phases [54]. This leads to the strategy to obtain high ZT materials by having a large number of band valleys N_v and a low and anisotropic effective mass m_c^*.

6.2 Complexity Factor

A way to achieve this goal with a trade-off between the various parameters was proposed by [90]. They consider an inertial mass m_c^* from the electrical conductivity and a density of states (DOS) mass m_S^* obtained from the Seebeck coefficient and carrier concentration. The ratio of these two masses gives the the Fermi Surface complexity factor:

$$N_v K = \left(\frac{m_s^*}{m_c^*}\right)^{3/2} \tag{6.2}$$

[1] $S \sim N_v$, consequently: $S^2\sigma \sim N_v$

related to the valley degeneracy and the carrier pocket anisotropy factor K. They derived the two effective masses directly from the BoltzTraP code.
From this large-scale machine-learning study of many different systems, it was found that the power factor σS^2 increases with $N_v K$ (see Fig. 3 of [90]) following a power law with exponent approximately 0.6, for about 2300 cubic compounds.

In our calculation we considered a database containing hundreds of materials properties calculated with high-throughput methods and we have selected on the basis of the Complexity Factor C given by:

$$C = N_v K \tag{6.3}$$

which, assuming the band energy vs $\mathbf{k}$ has a quadratic dependence near the relevant extremum, K can be written as:

$$K = \left[\frac{m_g}{m_h}\right]^{\frac{3}{2}} = \left[\frac{\sqrt[3]{m_1 m_2 m_3}}{\frac{m_1 m_2 m_3}{m_1 m_2 + m_1 m_3 + m_2 m_3}}\right]^{\frac{3}{2}} \tag{6.4}$$

where m_g and m_h are the geometric and harmonic averages of the locally diagonal mass tensor elements m_1, m_2 and m_3. It can be easily seen that $K = 1$ for isotropic case, making no contribution to complexity factor C [2].

6.2.1 Screening

We consider over than 800 compounds screened for:

- symmetry;
- band-gap;
- valley degeneracy N_v;
- mass anisotropy K;
- stability;

Using the large database of DFT computed electronic structures, Material Project [92], and the results for all compounds, we are considering only orthorhombic semiconductors with a band-gap between 1 eV and 1.6 eV as computed from Vasp in the GGA approximation and listed in the database.
For the valley degeneracy, in the database they have listed all the minima of conduction band and maxima of valence band by using a open-source Python library for materials analysis, Pymatgen (Python Materials Genomics) [93]. With this tool, all pockets of all bands are classified in a way easy to read. With these data it can be possible to consider minima of 2 different bands with a small

[2] Generally, it turns out that the complexity factor is much more sensitive to N_v that to the masses, or put otherwise K is usually not much larger than 1 even for quite anisotropic mass tensors.

energy difference (we selected $\Delta E \leq 0.01$ eV), hence many valleys available to conduction in a small energy range. We considered only the cases with a valley multiplicity $N_v \geq 4$ within the energy range considered.
For the mass anisotropy, we consider only material with a large K_v from the three effective mass components (m_x^*,m_y^*,m_z^*).
Finally, the stability of the structure depends on the energy above hull (E_{ah}), the energy of decomposition of this material into the set of most stable materials for this chemical composition, in eV/atom. A positive E above hull indicates that this material is unstable with respect to decomposition. A zero E above hull indicates that this is the most stable material at its composition. For this reason we set the value at 0 eV.
Our search identified a few materials of interest; in particular, based on the aforementioned criteria, we have found six potential materials for extended analyses:

- $FeBiSbS_4$
- DyB_4Mo
- PPdS
- YB_4Mo
- LaSO
- $CaPtO_3$

We excluded $FeBiSbS_4$ and $CaPtO_3$ because they decompose to more stable compounds. Then, Palladium-phosphide-sulphide PPdS has been already studied in literature for thermoelectric purposes [94]. They found a high anisotropic thermoelectric effect in PPdS due to its layered structure. The lattice thermal conductivity, for the same reason, is anisotropic in the three crystallographic directions, and the bulk value goes from 10 $W/(\mathrm{m} \cdot \mathrm{K})$ to 4 $W/(\mathrm{m} \cdot \mathrm{K})$ in the temperature range between 300-700 K. YB_4Mo and DyB_4Mo have similar structures, consequently we decided to study only one of them. The analysis is still ongoing and it will therefore not be subject of our discussion. Here we concentrate just on the especially promising lanthanum sulfoxide LaSO.

6.3 LaSO

6.3.1 Structure

The structure of the orthorombic phase of LaSO (Fig. 6.1), a layered material with space group *Cmca* and point group *mmm*, is optimized following quantum forces and stress in a conventional cell containing 8 formula units. The material is orthorhombic, and made up of bonded La-O planes intercalated in the a direction by molecular-crystal-like layers of S dimers. The resulting computed lattice constants are: $a = 13.323$ Å, $b = 5.950$ Å, $c = 5.945$ Å.

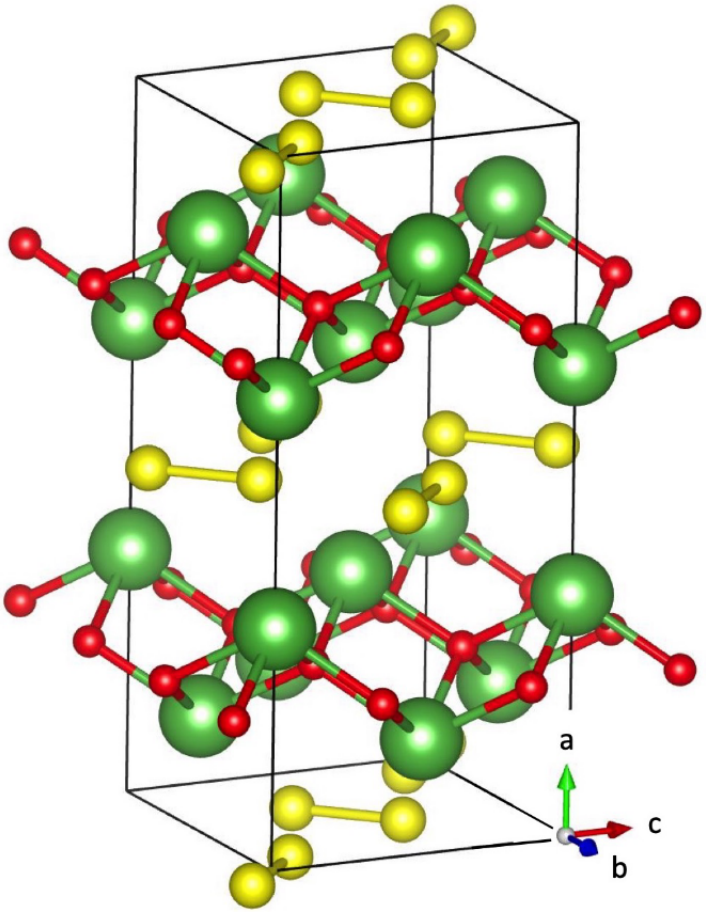

Fig. 6.1 Sketch of the structure of orthorhombic phase of LaSO. The conventional cell used is outlined. It is made up of bonded La-O planes intercalated along a direction by molecular-crystal-like layers of S dimers. La atoms in green, S atoms in yellow and O atoms in red. After the optimization of the cell, the resulting computed lattice constants are: $a = 13.323$ Å,$b = 5.950$ Å, $c = 5.945$ Å.

6.3.2 Lattice thermal conductivity

The lattice thermal conductivity κ_ℓ for LaSO has been derived from the phonon spectrum and the Grüneisen parameters[3]. The phonons dispersion curve is shown in Fig. 6.2. The calculations presented are carried out using DFT as implemented in the Quantum ESPRESSO package [27]. The exchange and correlation functionals approximated by the generalized gradient approximation and employing the projector augmented wave (PAW)-method and a plane waves basis set with pseudopotentials [24] from PseudoDojo. [87]. The cutoff for the wave functions was 100 Ry, the one for the charge density 400 Ry, and the k-points mesh was 4×4×4. Density functional perturbation theory (DFPT) [29] was used to calculate the dynamical matrices on an 4×4×4 q-points grid. These calculations are done automatically by the *thermo_pw* program [97]. For the Grüneisen spectrum, we used 9 reference geometries with lattice constants separated from each other by $\Delta a = 0.05$ a.u. The total spectrum of Grüneisen is shown in Fig. 6.3. The overall Grüneisen parameter is defined as:

$$\gamma = \frac{\sum_i \int \frac{d\mathbf{q}}{8\pi^3} \gamma_{i\mathbf{q}} C_{i\mathbf{q}}}{\sum_i \int \frac{d\mathbf{q}}{8\pi^3} C_{i\mathbf{q}}} \tag{6.5}$$

Our calculation predicts $\gamma = 0.8$.

Our prediction for lattice thermal conductivity is estimated from the model suggested on [95]. Considering the definition of the lattice thermal conductivity:

$$\kappa_\ell = \frac{1}{3} \sum_i \int \frac{d\mathbf{q}}{8\pi^3} \tau_{i\mathbf{q}} v_{i\mathbf{q}}^2 C_{i\mathbf{q}} \tag{6.6}$$

where the sum is over all phonon bands; the integral is over all q points in the first Brillouin zone; $v_{i\mathbf{q}}^2$ is the group velocity of a given phonon mode; $\tau_{i\mathbf{q}}$ is the mode relaxation time; and $C_{i\mathbf{q}}$ is the mode heat capacity depending only on the mode frequency and the temperature, they computed the relaxation time τ for phonons as:

$$\tau^{-1} = p\omega^2 \frac{T}{\theta_D} e^{-\theta_D/3T} \tag{6.7}$$

with:

$$p = \frac{1 - 0.514\gamma^{-1} + 0.288\gamma^{-2}}{0.0948} \frac{\hbar^2 \gamma^2}{k_B M V^{1/3} v_s} \tag{6.8}$$

[3]The Grüneisen parameter, γ, describes the effect that changing the volume of a crystal lattice has on its vibrational properties, and, as a consequence, the effect that changing temperature has on the size or dynamics of the crystal lattice. When the restoring force acting on an atom displaced from its equilibrium position is non-linear in the atom displacement, the phonon frequencies ω_i change with the volume V. The Grüneisen parameter of an individual vibrational mode i can then be defined as the negative of the logarithmic derivative of the corresponding frequency[98]

$$\gamma_i = -\frac{V}{\omega_i} \frac{\partial \omega_i}{\partial V}$$

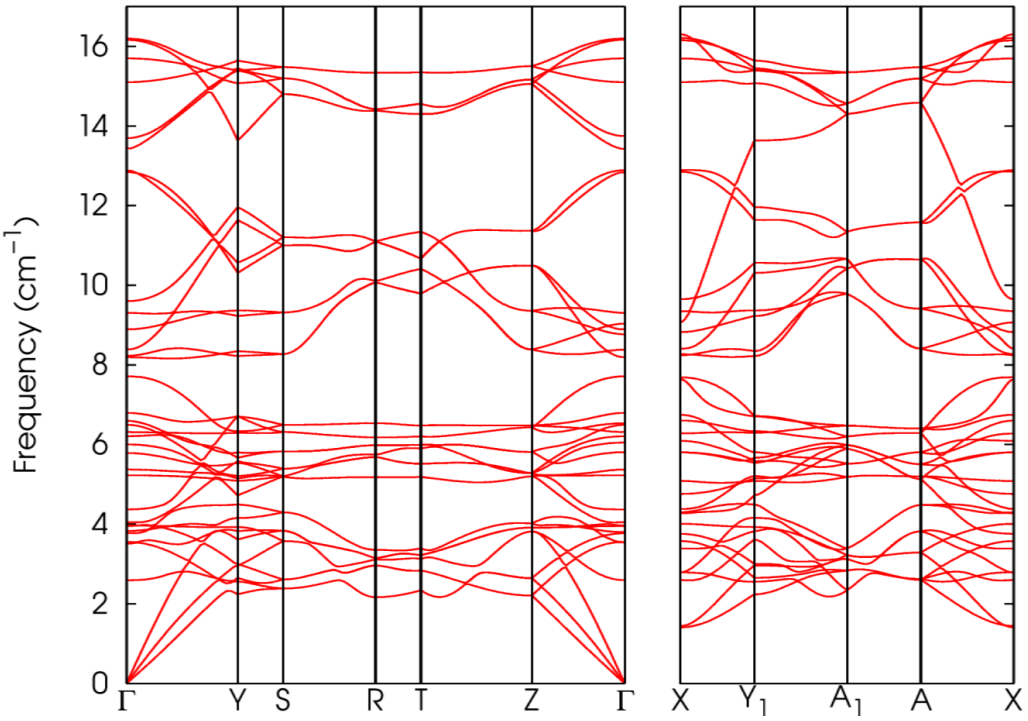

Fig. 6.2 Phonon dispersion for LaSO along selected high symmetric k-point paths in the first Brillouin zone.

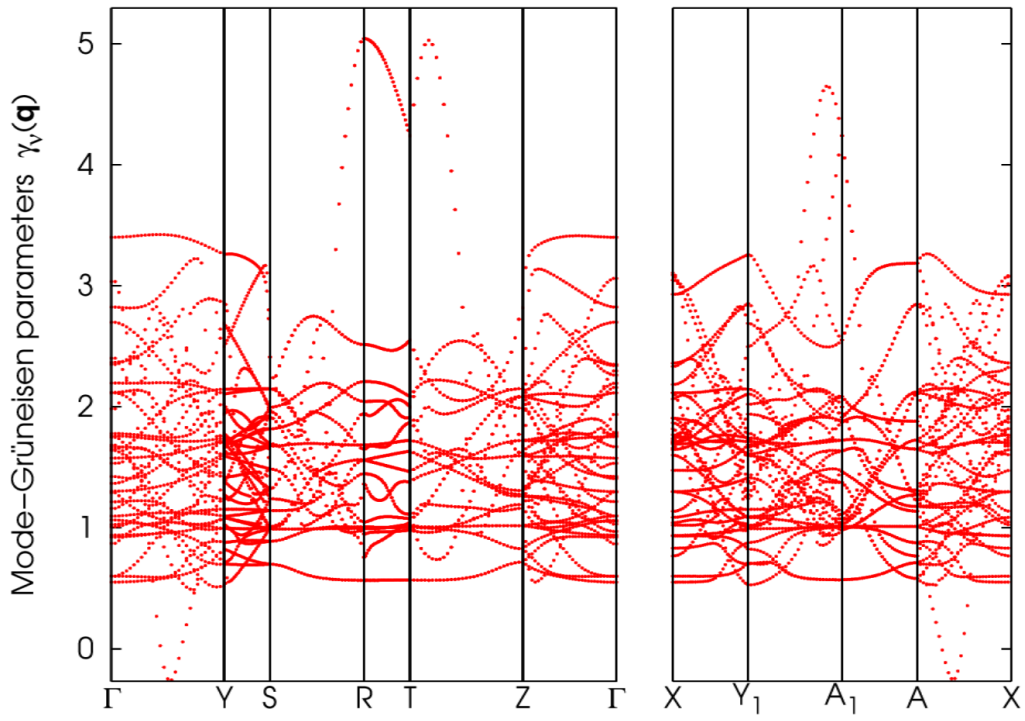

Fig. 6.3 Mode-Grüneisen parameters for LaSO calculated along selected high symmetry lines in the Brillouin zone with the method described in [97]

where γ is the Grüneisen parameter, V is the unit cell volume and M is the average atomic mass, v_s is the sound speed [4] and θ_D is the Debye temperature [5]. Besides phonon-phonon scattering (Equation 6.7), Casimir boundary scattering and mass disorder scattering can be easily introduced with a resistive relaxation time sum as already done for electron scattering as shown in Equation 6.9.

$$\tau^{-1} = \tau_{ph}^{-1} + \tau_C^{-1} + \tau_M^{-1} \tag{6.9}$$

For a crystal with shortest dimension L, it is normally assumed that the boundary scattering relaxation time is:

$$\tau_C^{-1} = v_S/L \tag{6.10}$$

While a mass disorder may be due in our case by a vacancy which depends on the mass of the missing atom, M_v, the vacancy concentration n_V, the average mass of the crystal M_{ave}, the number of atoms in the unit cell n_a and the sound velocity v_s (Equation 6.11):

$$\tau_M^{-1} = n_V \left(\frac{M_v}{M_{ave}} + 2 \right)^2 \frac{V\omega^4}{(4\pi n_a v_s^3)} \tag{6.11}$$

The Debye temperature is computed by considering the definition from [95] and [99]:

$$\theta_D^S = n^{-1/3} \sqrt{\left(\frac{5\hbar^2}{3k_B^2} \frac{\int_0^\infty \omega^2 g(\omega) d\omega}{\int_0^\infty g(\omega) d\omega} \right)} \tag{6.12}$$

obtained from the second moment of the whole phonon spectrum with n the density of LaSO. The density of states used in our calculation is shown in Fig. 6.4.

Since the definition of Debye temperature strongly affects the lattice conductivity because of the phonon-phonon scattering time exponential dependence, we compared the results obtained from the definition in Eq. 6.12 with that of [96] :

$$\theta_D^P = \frac{\hbar}{k_B} \frac{\int_0^\infty \omega \cdot g(\omega) d\omega}{\int_0^\infty g(\omega) d\omega} \tag{6.13}$$

The two definitions lead to two different results reported in tab 6.1 for three temperatures.
κ_ℓ are plotted with the two definitions in a temperature range between 100 K and 1100 K. With the latter method proposed, κ_ℓ is larger by roughly a factor two than in the former (Fig. 6.5).

In the following we will compare results obtained with the different scattering mechanisms. Mass disorder and micron-sized-crystallite Casimir scattering contribute to reduce the lattice thermal conductivity and that is more evident in the model with θ_D^P. But the choice of θ_D is what makes a difference.

[4] In our calculation, sound velocity is assumed to be constant and is cut off to zero above the Debye energy $k_B\theta_D$

[5] Note that an energy-dependent Grüneisen parameter (obtained as q integral of γ_{iq}) could be used in Eq.6.8. These changes leads to relatively minor changes in the present case.

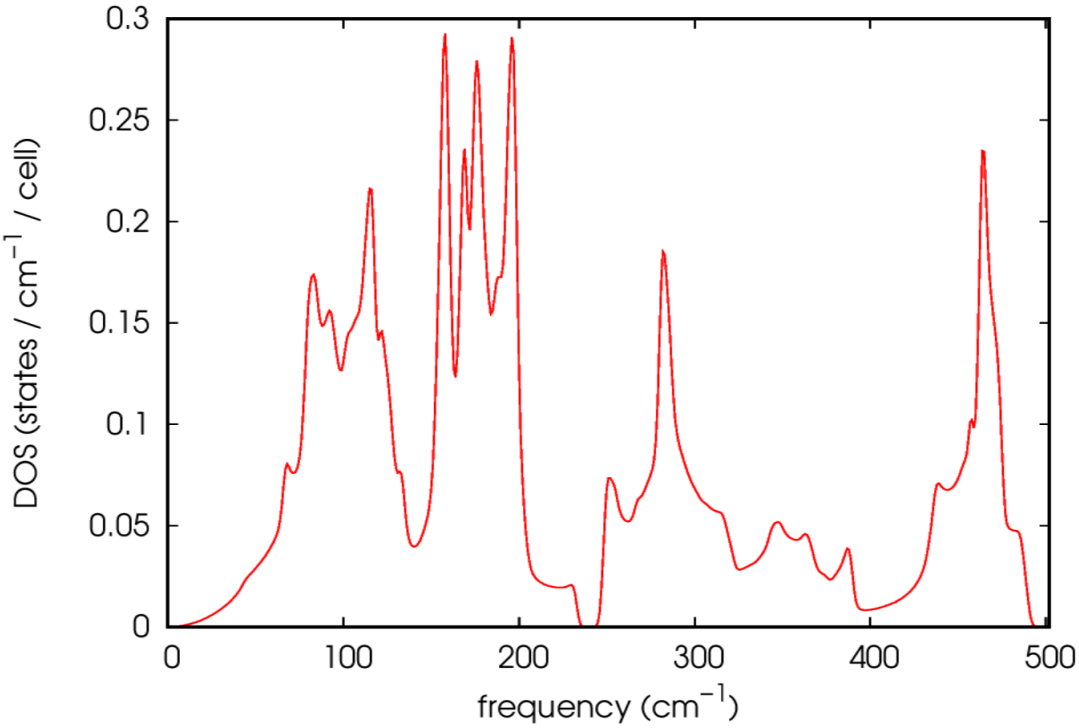

Fig. 6.4 Density of states for LaSO obtained using thermo_pw [97] software.

Table 6.1 Debye Temperature computed with the two definitions.

Debye Temperature	κ_ℓ **at 300 K**	κ_ℓ **at 700 K**	κ_ℓ **at 1000 K**
$\theta_D^S = 215$ (K)	1.7 [W/(K·m)]	0.82 [W/(K·m)]	0.6 [W/(K·m)]
$\theta_D^P = 335$ (K)	3.4 [W/(K·m)]	1.87 [W/(K·m)]	1.4 [W/(K·m)]

6.3.3 Computation details

Ab initio density functional structure optimization and band-structure calculations are performed with the generalized-gradient approximation (GGA) and the projector augmented wave method (PAW) using the VASP code, with the *La*, *S*, and O_s PAW datasets at the maximum suggested cutoff.
The electronic transport coefficients are computed from the ab initio density functional band structure as function of temperature and doping in the relaxation time approximation by using the linearized Boltzmann equation [36] [60].
We used the same model for the temperature- and energy-dependent relaxation time.
The electronic states are calculated on a (12 $\times$24 $\times$24) k-points grid. The minimum gap in GGA is 1.5 eV, so *n*-type thermoelectric coefficients are essentially unaffected by valence states.

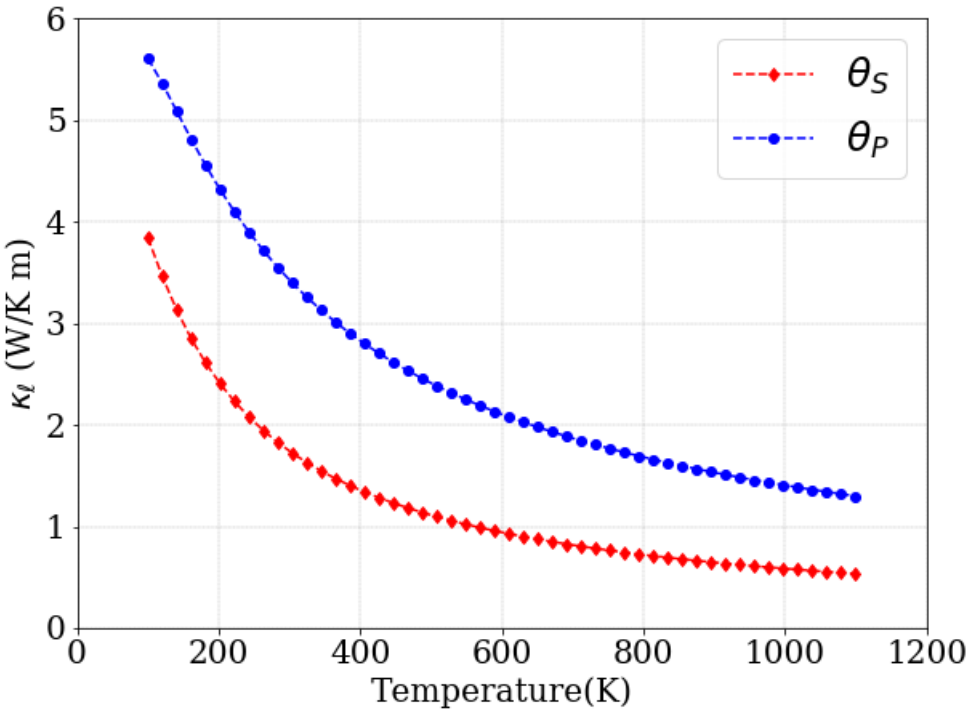

Fig. 6.5 Calculated lattice thermal conductivity κ_ℓ with two different definition of Debye temperature T_D: Passler at al.[96] Debye temperature θ_P and Debye temperature θ_S from the Slack [99] definition in the enhanced form proposed by [95]

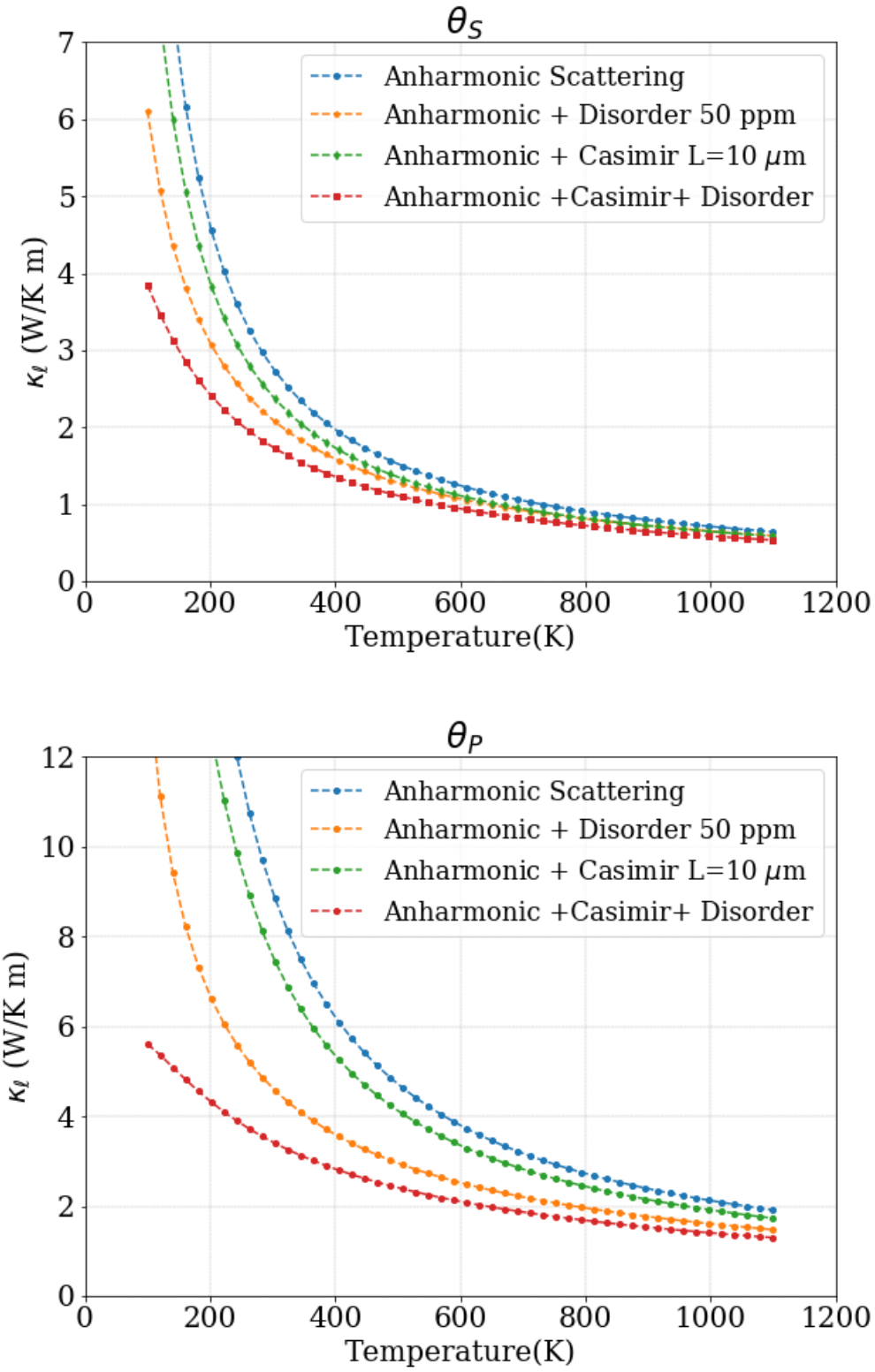

Fig. 6.6 Lattice thermal conductivity of LaSO for the perfect crystal including only anharmonic phonon-phonon scattering (blue curve), for anharmonic scattering and atomic disorder at 50 ppm i.e. 10^{18} cm^{-3} (orange dotted-dashed line), for anharmonic scattering and finite size of 10 μm (green dotted-dashed line), and finally for all the mechanisms included (red curve). The two plots correspond to two different definitions of the Debye temperature [95] [96]

Since our search was focused on conduction band behavior, we concentrate our attention on *n*-type doping, although *p*-doping also seems to have interesting values.

6.3.4 Transport coefficients

The transport coefficients accounting for energy- and temperature-dependent relaxation time are computed with BoltzTrap2 [60] transport code, allowing for the energy- and T-dependence of scattering times discussed in Chapter 3. The ab initio bands (with the rigid band approximation) are interpolated by a Fourier-Wannier technique over a finer grid with 64 times more points, equivalent to a (96 $\times$ 192 $\times$192) grid. As already discussed in previous chapters, a constant τ= τ_0 neglects important contribution on transport contributions. Hence, relaxation time used is temperature- and energy-dependent in our calculations. Details already presented in Chapter 3.

Parameters for the calculation

For the scattering mechanisms we computed:

- Conduction-band deformation potential D = 2.1 eV. We estimated it from the minimum of conduction band for the relaxed structure and for the strained structure, with an isotropic strain of 2% of the volume.
- density ρ = 5270 $\text{kg} \cdot \text{m}^{-3}$
- effective conduction band $m_c^* = 0.1 m_e$ where m_e.
- Sound velocity given as harmonic average over the acoustic branches is v_s = 3134 m/s. From linear-response phonon calculations
- Dielectric constants from linear-response phonon calculations: $\varepsilon_\infty = 6.23$ and $\varepsilon_{static} = 18.73$ as harmonic averages of the *b* and *c* components.
- The LO phonon energies are obtained via the Lyddane-Sachs-Teller relation from calculated TO phonons; for polarization along the *b* axis the first few energies are 17.6 meV, 34.2 meV, and 41.6 meV, those along *c* are 12.0 meV, 24.5 meV, and 33.7 meV, those along *a* are 30.6 meV and 46.9 meV. Since LO phonons only scatter electrons moving parallel to their polarization vector, this would entail a direction-dependent polar-phonon τ . However, the other uncertainties in the calculations, especially the choice of the lattice thermal conductivity, are much larger than any difference that might result from this distinction; thus, we elect to use a set of effective LO energies for all directions, namely 15 meV, 29 meV, and 38 meV.

In Fig. 6.7 the electronic band structure is plotted as a result of Vasp calculation. The indirect band gap is estimated to be 1.54 eV, with the maximum of the valence band in Y and the minimum of the conduction band in the point with coordinates: (−0.300, 0.700, 0.136) in the reciprocal space.

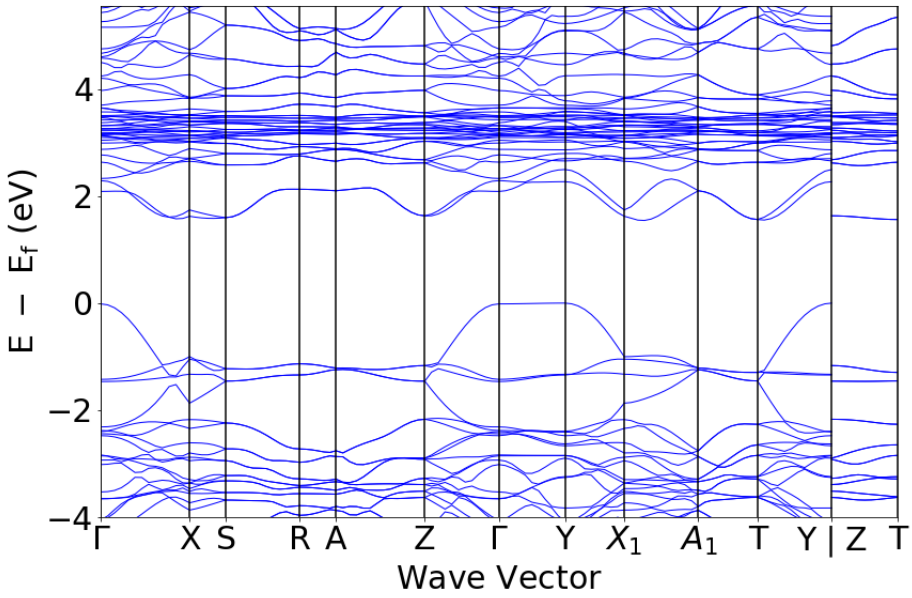

Fig. 6.7 Electronic band structure from DFT with Vasp in the GGA approximation calculated along high symmetry path in the Brillouin zone

Relaxation time

The behavior of $\tau(E,T)$ is shown as a function of energy in 6.8. As typical of polar insulators, the polar-phonon scattering dominates. In this case, it seems to be the only relavant contribution in the total relaxation time.

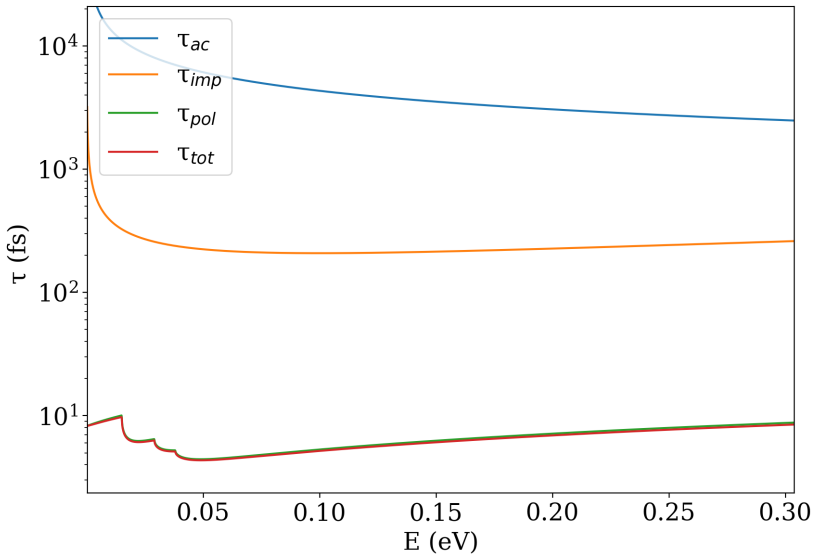

Fig. 6.8 Relaxation time vs E at T = 600 K. τ_{ac} is acoustic-phonon scattering, τ_i is due to impurity scattering, τ_{pol} stays for polar-optical phonon scattering while τ_{tot} is the total relaxation time. The major contribution is due to polar optical phonons, as typical of large gap semiconductors.

6.3.5 Electronic transport parameters

Fig. 6.9 reports the Seebeck coefficient, the electrical conductivity, the electronic thermal conductivity, and the power factor as a function of T at optimal doping. The *b* and *c* are the in-plane components. The large conductivity and Seebeck result in a sizable power factor for the in-plane transport and a negligible power factor in the *a*-direction, in line with the values anticipated by our database search. Fig.6.10 report the Seebeck coefficient, the electrical conductivity, the electronic thermal conductivity, and the power factor, respectively, as a function of doping and parametrized by temperature, each line represents a different temperature from 200 to 1100 K in step of 100 K and and the line thickness is proportional to temperature. Since *b* and *c* components are very close and *a* component gives a rather small power factor contribution, only the *b* component is plotted in in Fig. 6.10.
Our results for the power factor confirm that high valley multiplicity is conducive to large electronic parameters.

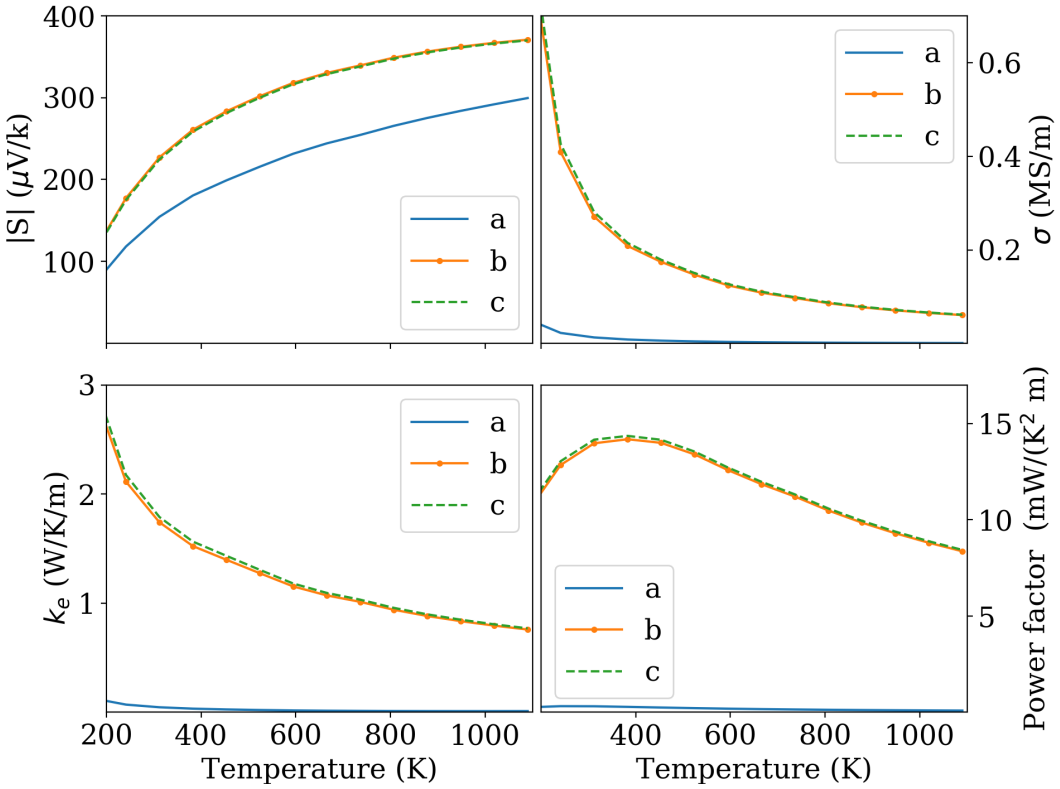

Fig. 6.9 Seebeck coefficient *S*, electrical conductivity σ, electronic thermal conductivity κ_e, and power factor vs T at optimal doping level (the level at which the maximum in ZT occurs.

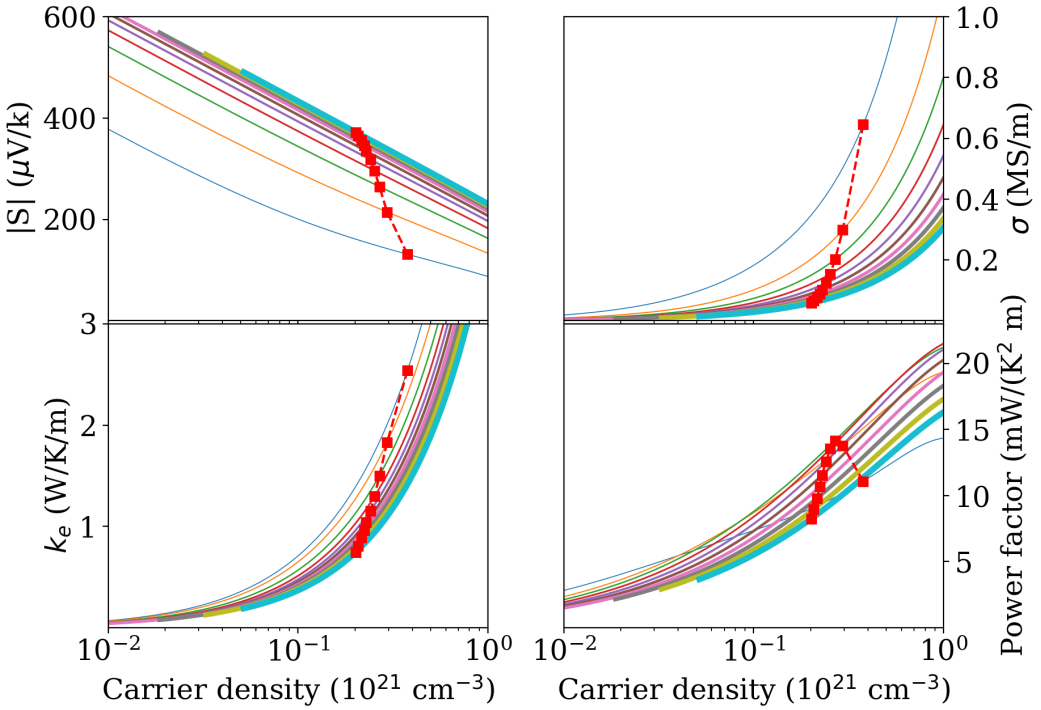

Fig. 6.10 Seebeck, conductivity, electronic thermal conductivity, and power factor vs doping at different T from 200 to 1100 K in step of 100 K, the line thickness is proportional to temperature. Red squares indicate values at optimal doping.

6.3.6 Complexity factor and valley multiplicity in LaSO

One of the reasons why this material is promising, lies in the high complexity factor. Results from the database search are summarized in Table 6.2.

From a more meticulous analysis of the band structure and the Fermi Surface, we can get a clearer

Table 6.2 Complexity Factor from Database

N_v	K	m_1^*	m_2^*	m_3^*
8	18.3	0.044	0.105	2.069

idea of the electronic properties leading to a high power factor and hence ZT. Fig. 6.11 reports the conduction-band Fermi surface of doped LaSO at several chemical potentials, as well as the Brillouin zone (BZ) with a reference path. The first four conduction bands, marked in different colors (1st in

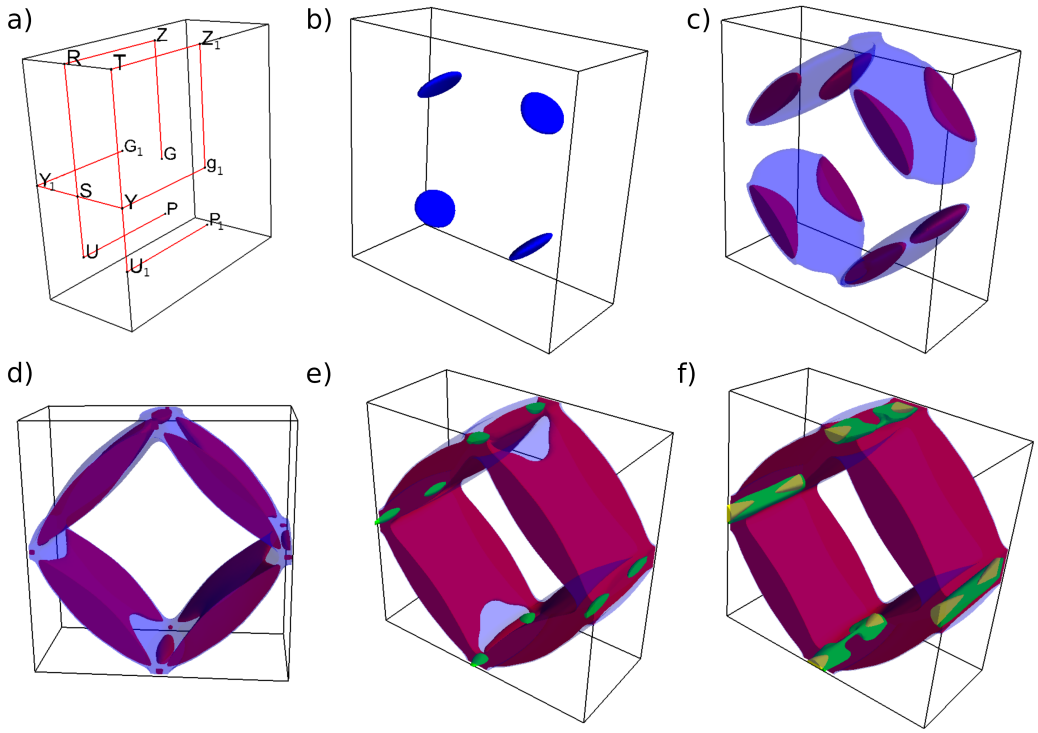

Fig. 6.11 a) Brillouin zone with the high symmetry points path used for calculations.
b) Fermi surfaces of the 1st conduction band in blue at 0.01 eV above the conduction edge,
c) 1st (in blue) and 2nd (in red) conduction bands at 0.07 eV above the conduction edge,
d) 1st and 2nd conduction bands at 0.1 eV above the conduction edge,
e) 1st, 2nd, 3rd and 4th conduction bands in blue, red, green and yellow, respectively at 0.11 eV
f)1st, 2nd, 3rd and 4th conduction bands at 0.13 eV above the conduction edge.

blue, 2nd in red, 3rd in green and 4th in yellow), provide at least 16 available valleys within 130 meV. In particular, four valleys are internal to the BZ from the first band; eight valleys come from the second band on the square faces, consequently with weight 1/2 because shared with adjacent BZs.

Eight valleys from the third band on the segments Z-Z_1 and S-Y/S-Y_1 of the BZ path with weight 1/2, and eight valleys from the fourth band on the same segment with weight 1/2. The same can be obtained counting the 16 bands available for conduction within about 130 meV. The carrier density vs. energy in Fig.6.12, central panel, shows that all these bands will be occupied at the chemical potentials and temperatures of our interest (μ near the lowest conduction edge, and temperatures in the range of 30 to 900 K). Accordingly, all the bands just mentioned may be considered active, so that the effective total multiplicity of the occupied valleys is N_v = 16 (see Table 6.3 for more details). From Fig. 6.12 we can also infer at this stage that the optimal doping level, namely the doping at which ZT is maximal for a given T, will probably fall in the mid 10^{20} cm^{-3} , and that the Seebeck coefficient may be interesting due to the fast rise of the density of states near the band edge.

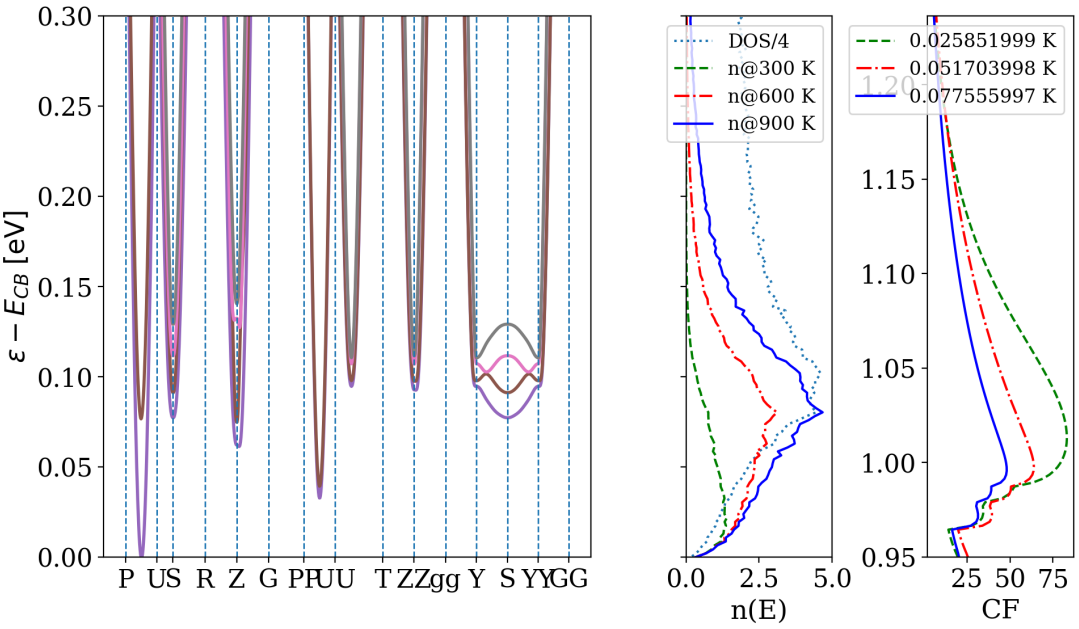

Fig. 6.12 Left: conduction bands of LaSO along the paths marked in Fig. 6.11 a). Center: the density of states and carrier density (i.e. the Fermi distribution times the conduction density of states), both in units of 10^{21} cm^{-3} eV^{-1} as a function of energy. Right: complexity factor for the *b* direction (*c* is similar, *a* is about zero) vs energy. In the center and right panel, μ=0 and T =300, 600, 900 K

Table 6.3 Valley multiplicity N_v for each valley of the first four conduction bands and their correspondent energy

Band 1	**Valley**			
	1	**2**	**3**	**4**
N_v	4	1	-	-
Energy	0.0 eV	0.08 eV	-	-
Band 2	**Valley**			
	1	**2**	**3**	**4**
N_v	4	1	1	2
Energy	0.05 eV	0.08 eV	0.095 eV	0.101 eV
Band 3	**Valley**			
	1	**2**	**3**	**4**
N_v	4	-	-	-
Energy	0.11 eV	-	-	-
Band 4	**Valley**			
	1	**2**	**3**	**4**
N_v	2	-	-	-
Energy	0.12 eV	-	-	-

6.3.7 Figure of merit of LaSO

Finally, in Fig. 6.13 we show the ZT tensor for the two instances of lattice thermal conductivity. The left panels report the diagonal components of ZT as function of T at optimal doping (i.e. the doping at which ZT is a maximum at a given temperature), and the right panels the *b* component as function of doping and for a number of temperatures. All is drawn on the same scale to ease comparison. The *b* and *c* components deviate by only a fraction of 1% , and the *a* component is small and thus, it can be neglected. ZT is very large, 3.5 and 6.5 at high temperature for the two version of the lattice thermal conductivity and the optimal doping level is around 2.5×10^{20} cm^{-3} and the optimal doping at each temperature is roughly the same. These values make it very promising the future of thermoelectricity. The reason of this large ZT is to be found in the large power factor due to the high valley multiplicity, and that confirms the potential of the method used to identify materials with a large thermoelectric efficiency. LaSO, in particular, could be the future of thermoelectricity with its great efficiency: further theoretical studies and experiments could confirm our findings.

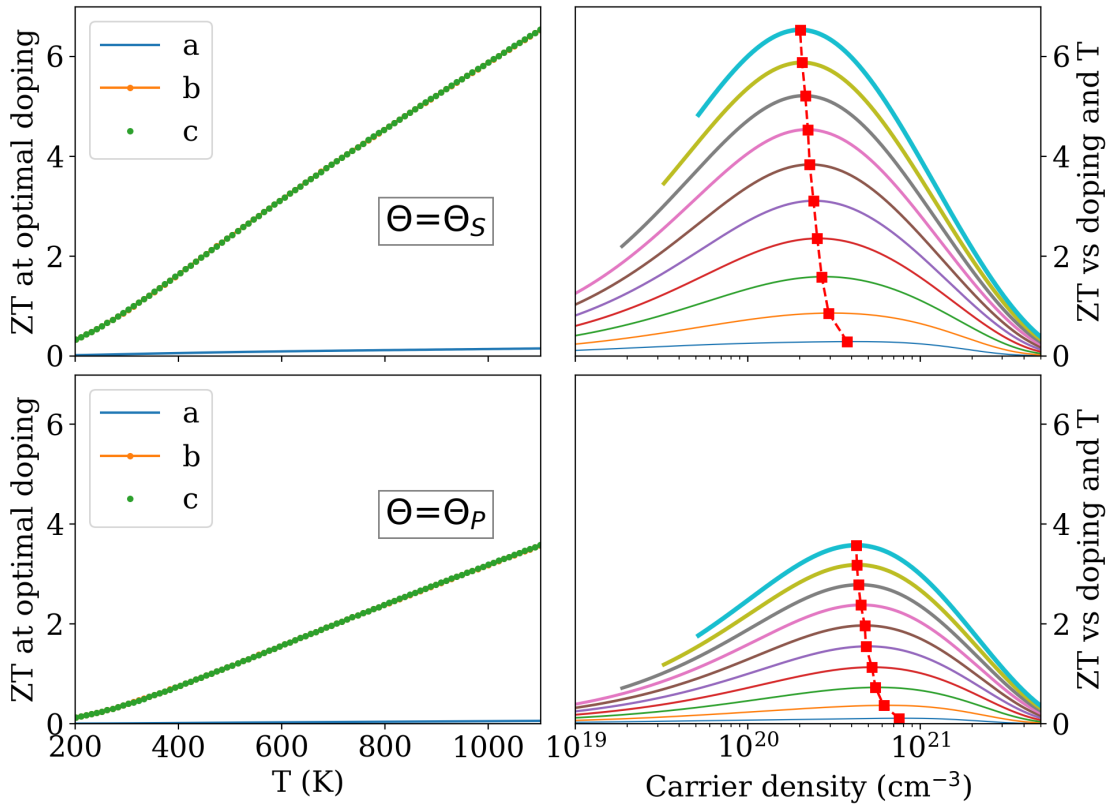

Fig. 6.13 ZT of LaSO. Top row is for lattice thermal conductivity calculated with $\theta_D = \theta_D^S$ and bottom row for $\theta_D = \theta_D^P$. Left column: ZT vs T at optimal doping; right column, ZT_b vs doping and for various temperatures. Temperatures in the right panels are 200 to 1100 K, line thickness proportional to T . All quantities drawn on identical scales for easier comparison.

Conclusions

In this concluding section, all main outcomes of my research will be summarized.

Density functional theory was used in conjunction with Boltzmann transport theory to examine the thermoelectric properties of layered semiconductors. The thermoelectric efficiency dependence on lattice thermal conductivity was explored in all the calculations for the different materials. It would prove to be one of the aspects to deepen, as it represents a key factor in improving figure of merit. The second key factor is the scattering model choice for relaxation time. Hence, this work explores various models for τ.

In Chapter 4, it was found that Mg_3Sb_2 demonstrates an improvement in thermoelectric efficiency in the polycrystal sample due to its low lattice thermal conductivity of around 1.5 W/(m·K) for the temperatures considered. The reason for that small lattice thermal conductivity is not due to intrinsic reasons, but rather because of Casimir grain-boundary scattering. While the bulk thermal conductivity is around 10 W/(K·m) at room temperature, it drops to about 1.5 W/(m· K) or less for a typical experimental distribution of grain sizes. Taking into account also alloys with Bismuth and consequentely a strong mass disorder, κ_ℓ is found to be considerably reduced up to the value of 0.8 W/(m·K).

Added to this lattice thermal conductivity, it is the relaxation time used for the electronic part. We have calculated the thermoelectric coefficients and figure of merit ZT in Mg_3Sb_2 using a temperature- and energy-dependent relaxation time.

The effects of this improved approximation are significant, especially for the electrical and the electronic thermal conductivity. The electronic component of thermal conductivity is found to be reduced by at least 60 % of the value obtained with a constant relaxation time. While the electrical conductivity temperature dependence changes by introducing the scattering model, especially at high doping levels, reaching 3×10^3 (1/(m Ω· cm)) against 2×10^3 (1/(mΩ· cm)) for the constant relaxation time calculation at room temperature. Where applicable, our results are in good agreement with experiments.

Consequently, this work represents a good proof to validate the reliability of our scattering model for electrons and our choice of relaxation time τ. ZT increases monotonically in the temperature range we consider; on the other hand, it has a maximum as a function of doping: our estimate of the peak-ZT optimal n -doping of Mg_3Sb_2 is about 5×10^{19} cm^{-3}, over all the 300-700 K range.

However the increase in ZT with our study is not significant enough to make Mg_3Sb_2 viable alternative to present technologies with a maximum value for ZT around 1.5 at optimal doping of 5×10^{19} cm^{-3}.
In Chapter 5, a study of the orthorhombic phase of perovskite $La_2Ti_2La_7$ has been reported. Much of the potential of this material is due to its small and almost T -independent lattice thermal conductivity; using a model based on ab initio anharmonicity calculations, we explain this low value as due to effective phonon confinement within the layered-structure blocks.
We have predicted a thermoelectric figure of merit between 1 and 2.6 in the T range of 300-1200 K under *n*-doping and *p*-doping via calculations of the electronic structure, transport coefficients, and thermal conductivity. The optimal carrier density for *n*-doping is found to be in the low-10^{20} cm^{-3} range. At that density, the Seebeck thermopower coefficient is between 200 and 300 μV/K; it can, however, reach nearly 1 mV/K at lower doping.
The largest ZT is obtained along the *a* crystal axis, while the other components are one to two orders of magnitude smaller. On the contrary, the maximum ZT in *p*-type conditions is a factor of 2- 4 smaller than in *n*-type, and it requires carrier densities about an order of magnitude higher. Much of the potential of this material is due to its small lattice thermal conductivity; using a model based on ab initio anharmonicity calculations, we explain this low value as due to effective phonon confinement within the layered-structure blocks.
In Chapter 6, I have reported an on-going investigation about lanthanum oxysulphate (LaSO).
As in the previous cases, the orthorhombic phase of LaSO is a layered structure. We predicted a giant thermoelectric figure of merit in this high-valley-multiplicity material. The lattice thermal conductivity, obtained by using the ab-initio-computed phonon dispersion and Grüneisen parameters, and the Debye temperature is found to be 1.7 and 3.4 W/(m· K) for the [95] and [96] model, respectevely. For the perfect crystal, ZT is linear in temperature and at 1100 K reaches a value between 3.5 and 6.5 depending on the model choice for the lattice thermal conductivity. The optimal doping is almost temperature independent, and in the $2-3 \times 10^{20}$ cm^3 range. Our results for the power factor confirm earlier suggestions [90] that high valley multiplicity is conductive to large power factors and therefore large ZT.
This study has been developed in collaboration with Dr. Francesco Ricci from Institute of Condensed Matter and Nanosciences (IMCN), at Université Catholique de Louvain (Belgium).
Further investigations of the electronic band structure and Fermi surface could explain the exceptional values found for ZT.

Outlook

In the last decades we have witnessed important enhancements in the field of thermoeletrics. The most challenging goal is finding materials with large power factor and low κ at the same time, following the idea of *phonon glass electron crystal*.
In this thesis, we have presented a method to analyze thermoeletric properties starting from density functional theory and a Boltzmann Transport Equation using a energy- and temperature- dependent relaxation time and including many important scattering contributions for the evaluation of κ_ℓ. The study carried out here has the potential to drive future research using the same protocol: work presented in chapters 4 and 5 of this thesis is published in peer reviewed scientific journals.
Moreover, this work has revealed that the screening method used in the last chapter could speed up the search of new promising thermoelectrics. This screening is already used for the large search of thermoelectrics, as described on reference [90] for cubic compounds. Our work confirms the validity of that previous work and opens up the possibility for future study on other interesting materials, among them YB_4Mo, the other compound identified by our screening.

References

[1] T. M. Tritt, Recent Trends in Thermoelectric Materials Research, Semiconductors and Semimetals, Vols. 69-71, Elsiever, R.K. Willardson and E. Weber, Academic Press, New York (2000).

[2] D. D. Abelson, in *Thermoelectrics Handbook: Macro to Nano*, ed. by D.M. Rowe (CRC Taylor and Francis, Boca Raton, 2006), pp. 56-1

[3] https://solarsystem.nasa.gov/missions/cassini/radioisotope-thermoelectric-generator/

[4] http://thermoelectrics.matsci.northwestern.edu/thermoelectrics

[5] T. J. Seebeck, *Ueber den magnetismus der galvenische kette*, Abh. K. Akad. Wiss. (Berlin, 1823) p. 265.

[6] G. J. Snyder, E. S. Toberer, Complex thermoelectric materials. *Nature Materials 7*, 105-114 (2008); https://doi.org/10.1038/nmat2090

[7] M. Cutler, J. F. Leavy, R. L. Fitzpatrick, Electronic transport in semimetallic cerium sulfide. *Phys. Rev.* ***133***, A1143-A1152 (1964); https://doi.org/10.1103/PhysRev.133.A1143.

[8] Ran He et al., Thermoelectric properties of silicon and recycled silicon sawing waste, *Journal of Materiomics*, 10.1016 (2018); https://doi.org/10.1016/j.jmat.2018.11.004

[9] I. T. Witting et al., The Thermoelectric Properties of Bismuth Telluride, 10.1002 (2019), *Advanced Electronic Materials*; https://doi.org/10.1002/aelm.201800904

[10] A. F. Ioffe, Semiconductor Thermoelements and Thermoelectric Cooling, *Physics Today 12*, 5, 42 (1959); https://doi.org/10.1063/1.3060810

[11] G. A. Slack, CRC Handbook of Thermoelectrics, ed. by D. M. Rowe, Boca Raton , pp. 407 - 440 (1995)

[12] J. He, M. G. Kanatzidis, V. P. David, High performance bulk thermoelectrics via a panoscopic approach, *Materials Today, 16(5)*, pp. 166-176 (2013)

[13] J. P. Heremans, M. S. Dresselhaus, L. E. Bell, D. T. Morelli, *Nature Nanotechnology 8*, pp. 471 - 473 (2013)

[14] Hohenberg, P., and W. Kohn, *Phys. Rev. 136*, B864, (1964)

[15] Kohn, W., and L. J. Sham, *Phys. Rev. 140*, A1133 (1965)

[16] R. M. Martin, Electronic Structure: basic theory and applications, Cambridge University Press, (2004)

[17] J. P. Perdew, K. Burke, M. Ernzerhof, *Phys. Rev. Lett. 77*, 3865 (1996); https://doi.org/10.1063/1.478401

[18] P. Ziesche and H. Eschrig. Electronic structure of solids 91, (1991)

[19] A. Dal Corso et al.; Generalized-gradient approximations to density-functional theory: A comparative study for atoms and solids, *Phys Rev B* (1996)

[20] N. D. Woods et al., *J. Phys.: Condens. Matter 31* 453001 (2019)

[21] D. R. Hartree, Math. Proc. Camb. Phil. Soc. 24 111132 (1928); https://doi.org/10.1017/S0305004100015954

[22] D. R. Hamann, M. Schlüter, C. Chiang, "Norm-Conserving Pseudopotentials", *Phys Rev Lett **43*** (1979)

[23] G. Kresse, and D. Joubert, *Phys. Rev. B* **59**, 1758 (1999); https://doi.org/10.1103/PhysRevB.59.1758

[24] P.E. Blöchl, *Phys. Rev. B* **50**, 17953 (1994); https://doi.org/10.1103/PhysRevB.50.17953

[25] X. Gonze et al., First-principles computation of material properties: The ABINIT software project, *Computational Materials Science* **25**, 478-492 (2002) https://doi.org/10.1016/s0927-0256(02)00325-7

[26] G. Kresse and J. Furthmüller, *Phys. Rev. B* **54**, 11169 (1996); http://dx.doi.org/10.1016/0927-0256(96)00008-0

[27] P. Giannozzi et al., *J. Phys.: Condens. Matter* **21**, 395502 (2009)

[28] P. Giannozzi et al., *J. Phys.: Condens. Matter* **29**, 465901 (2017)

[29] Baroni et al., *Rev. Mod. Phys.*, Vol. **73**, No. 2, (2001); https://doi.org/10.1103/RevModPhys.73.515

[30] J.M. Ziman, Electrons and Phonons, The theory of transport phenomena in solids (OUP, USA, 1960)

[31] S. Baroni, P. Giannozzi, and A. Testa, *Phys. Rev. Lett.* **58**, 1861 (1987)

[32] X. Gonze, *Phys. Rev. A* **52**, 1086 (1995)

[33] N. W. Ashcroft and D. N. Mermin, Solid State Physics, Holt, Rinehart and Winston (1976)

[34] C. Kittel, Introduction to Solid State Physics, 6th Ed., Wiley (1986)

[35] M. S. Dresselhaus, Solid State Physics, Transport Properties of Solids (2001)

[36] P. B. Allen, *Phys. Rev. B* **17**,3725 (1978)

[37] P. B. Allen, W. E.Pickett, and H. Krakauer, *Phys. Rev. B* **37**, 7482 (1988)

[38] B. K. Ridley, Quantum Processes in Semiconductors (Clarendon, Oxford, UK, 1988)

[39] B. K. Ridley, *J. Phys.: Condens. Matter* **10**, 6717 (1998)

[40] G. Joshi et al., Enhanced Thermoelectric Figure-of-Merit in Nanostructured p-type Silicon Germanium Bulk Alloys. *Nano Letters*, **8**(12) 4670 - 4674 (2008); https://doi.org/10.1021/nl8026795

[41] X. W. Wang et al., Enhanced thermoelectric figure of merit in nanostructured n-type silicon germanium bulk alloy. *Applied Physics Letters*, **93** (19) : 193121 (November 2008); https://doi.org/10.1063/1.3027060

[42] D. G. Cahill, S. K. Watson, and R. O. Pohl, Lower limit to the thermal conductivity of disordered crystals, *Phys. Rev. B*, **46**(10) : 6131 - 6140, (1992); https://doi.org/10.1103/PhysRevB.46.6131

[43] S. M. Kauzlarich, A. Zevalkink, E. Toberer and G. J. Snyder, *Zintl Phases: Recent Developments in Thermoelectrics and Future Outlook*, Thermoelectric Materials and Devices, pp 1 - 26; https://doi.org/10.1039/9781782624042-00001

[44] E. Zintl, E. and Husemann, Bindungsart und gitterbau binärer magnesiumverbindungen. *Phys. Chem.* **21**B, 138-155 (1933)

[45] J. Zhang, et al. Designing high-performance layered thermoelectric materials through orbital engineering, *Nat Commun* **7**, 10892 (2016); https://doi.org/10.1038/ncomms10892

[46] L. Paulatto, F. Mauri, and M. Lazzeri, *Phys. Rev. B* **87**, 214303 (2013); https://doi.org/10.1103/PhysRevB.87.214303

[47] G. Fugallo, M. Lazzeri, L. Paulatto, and F. Mauri, *Phys. Rev. B* **88**, 045430 (2013); https://doi.org/10.1103/PhysRevB.88.045430

[48] C. Hartwigsen, S. Goedecker, and J. Hutter, *Phys. Rev. B* **58**, 3641 (1998) https://doi.org/10.1103/PhysRevB.58.3641

[49] J. Zhang , L. Song , S. Hindborg Pedersen,H. Yin , L. T. Hung and B. Brummerstedt Iversen, *Nat. Commun.* **8** 13901 (2017)

[50] A. Bhardwaj , N. S. Chauhan and D. K. Misra. *J. Mater. Chem. A* **3**, 10777-10786 (2015)

[51] W. Peng, G. Petretto, G.-M. Rignanese, G. Hautier, and A. Zevalkink, *Joule* **2**, 1879-1893 (2018) ; https://doi.org/10.1016/j.joule.2018.06.014

[52] J. Li, S. Zheng ,T. Fang , L. Yue , S. Zhang and G. Lu, *Phys. Chem. Chem. Phys.* **20**, 7686-7693 (2018); https://doi.org/10.1039/C7CP08680F

[53] J. Zhang, L. Song, and B.B. Iversen, Insights into the design of thermoelectric Mg_3Sb_2 and its analogs by combining theory and experiment, *npj Comput Mater* **5**, 76 https://doi.org/10.1038/s41524-019-0215-y (2019)

[54] J. Zhang, L. Song, M. Sist, K. Tolborg, and B. Brummerstedt Iversen, *Nat. Commun.* **9**, 4716 (2018).

[55] H. Tamaki, H. K. Sato, and T. Kanno, *Adv. Mater.* **28**, 10182 (2016); https://doi.org/10.1002/adma.201603955

[56] S. H. Kim et al., *J. Mater. Chem. A* **2**, 12311 (2014).

[57] C. L. Condron, S. M. Kauzlarich, F. Gascoin, and G. J. Snyder, *J. Solid State Chem.* **179**, 2252 (2006); https://doi.org/10.1016/j.jssc.2006.01.034

[58] F. Ahmadpoura, T. Kolodiazhnyi, and Y. Mozharivskyja, *J. Solid State Chem.* **180**, 2420 (2007)

[59] G. K. H. Madsen and D. J. Singh, *Comput. Phys. Commun.* **175** 67 (2006); https://doi.org/10.1016/j.cpc.2006.03.007

[60] G. K. H. Madsen, J. Carrete, and M. J. Verstraete, *Computer Physics Communications* **231**,140 (2018); https://doi.org/10.1016/10.1016/j.cpc.2018.05.010

[61] M. Cutler and N. F. Mott, *Phys. Rev.* **181**, 1336 (1969)

[62] W. Tingjun and G. Peng, *Materials* **11**,999 (2018)

[63] M. B. Maccioni, R. Farris, and V. Fiorentini *Phys. Rev. B* **98**, 220301(R) (2018); https://doi.org/10.1103/PhysRevB.98.220301

[64] R. Farris, M. B. Maccioni, A. Filippetti, V. Fiorentini; *J. Phys.: Condens. Matter* **31** (6), 065702 (2019); https://doi.org/10.1088/1361-648X/aaf364

[65] R. Farris et al.; *J. Phys.: Conf. Ser.* **1226** 012010 (2019), https://doi.org/10.1088/1742-6596/1226/1/012010

[66] A. Dal Corso, *Computational Material Science* 95, 337 (2014)

[67] V. Fiorentini and A. Baldereschi, *Phys. Rev. B* **51**, 17196 (1995); https://doi.org/10.1103/PhysRevB.51.17196

[68] G. Casu, A. Bosin and V. Fiorentini, *Phys. Rev. Materials* **4**, 075404 (2020); https://doi.org/10.1103/PhysRevMaterials.4.075404

[69] P. Y. Yu and M. Cardona, *Fundamentals of Semiconductors* (Springer, Berlin, 2010), Chap. 5.

[70] J. F. Nye, *Physical Properties of Crystals* (Clarendon, Oxford,UK, 1985)

[71] N. Ishizawa, F. Marumo, S. Iwai, M. Kimura, T. Kawamura, *Acta Crystallogr. B* **38**, 368-372; https://doi.org/10.1107/S0567740882002994

[72] A. G. Kalinichev, J. D. Bass, C. S. Zhab, P. D. Han, and D. A.Payne, *J. Appl. Phys.* **74**, 6603 (1993);

[73] F. Chen, L. Kong, W. Song, C. Jiang, S. Tian, F. Yu, L. Qin, C. Wang, and X. Zhao, *J. Materiomics* **5**, 73 (2019).

[74] A. Krause, W. M. Weber, D. Pohl, B. Rellinghaus, A. Kersch, and T. Mikolajick, *J. Phys. D: Appl. Phys.* **48**, 415304 (2015); https://doi.org/10.1088/0022-3727/48/41/415304

[75] J. Lopez-Perez and J. Iniguez, *Phys. Rev. B* **84**, 075121 (2011); https://doi.org/10.1103/PhysRevB.84.075121

[76] S. Nanamatsu, M. Kimura, K. Doi, S. Matsushita, and N. Yamada, *Ferroelectrics* **8**, 511 (1974); https://doi.org/10.1143/JPSJ.38.817

[77] B. A. Strukov, S. T. Davitadze, S. N. Kravchun, S. A. Taraskin, B. M. Goltzman, V. V. Lemanov, and S. G. Shulman, *J. Phys.: Condens. Matter* **15**, 4331 (2003), 10.1088/0953-8984/15/25/304

[78] F. Lichtenberg, A. Herrnberger, K. Wiedenmann, J. Mannhart *Prog. Solid State Chem.*, **29** (2001), https://doi.org/10.1063/1.1572960

[79] T. D. Sparks, P. A. Fuierer, and D. R. Clarkew, *J. Am. Ceram. Soc.* **93**, 1136 (2010); https://doi.org/10.1111/j.1551-2916.2009.03533.x

[80] Inorganic Solid Phases, edited by P. Villars and Karin Cenzual, *Springer Materials database* (Springer, Heidelberg, 2016)

[81] L. C. Robinson, *Physical Principles of Far-Infrared Radiation*, Vol **10** (1 ed.) (1973).

[82] J. Khaliq, C. Li, K. Chen, B. Shi, H. Ye, A. M. Grande, H. Yan,and M. J. Reece, *J. Appl. Phys.* **117**, 075101 (2015); https://doi.org/10.1063/1.4908209

[83] H. B. G. Casimir, *Physica 5*, **495** (1938);

[84] R. Berman, F. E. Simon, and J. M. Ziman, *Proc. R. Soc. London, Ser. A* **220**, 171 (1953)

[85] R. Berman, E. L. Foster, and J. M. Ziman, *Mathematical and Physical Sciences* **231**, 130 (1955)

[86] V. Fiorentini, R. Farris, E. Argiolas, and M. B. Maccioni *Phys. Rev. Materials* **3**, 022401(R) (2019); https://doi.org/10.1103/PhysRevMaterials.3.022401

[87] M. J. van Setten, M. Giantomassi, E. Bousquet, M. J. Verstraete, D. R. Hamann, X. Gonze, and G.-M. Rignanese, *Comput. Phys. Commun.* **226**, 39 (2018); http://www.pseudo-dojo.org

[88] J. S. Coursey, D. J. Schwab, J. J. Tsai, and R. A. Dragoset, Atomic Weights and Isotopic Compositions, NIST, Gaithers- burg, MD, 2015; http://physics.nist.gov/Compon2018/10/02

[89] Pei, Y., Wang, H. Snyder, G. J. Band engineering of thermoelectric materials, *Adv. Mater.* ***24***, 6125-6135 (2012); https://doi.org/10.1002/adma.201202919

[90] Zachary M. Gibbs, *npj Computational Materials* **3** : 8 (2017); https://doi.org/10.1038/s41524-017-0013-3

[91] E. A. Pfeif and K. Kroenleina, *APL Materials* ***4***,053203 (2016) ; https://doi.org/10.1063/1.4942634

[92] A. Jain et al., A high-throughput infrastructure for density functional theory calculations, *Comp. Mater. Sci.* ***50***, 2295 - 2310 (2011); https://doi.org/10.1016/j.commatsci.2011.02.023

[93] S. P. Ong et al., Python Materials Genomics (pymatgen) : A Robust, Open-Source Python Library for Materials Analysis. *Computational Materials Science* **68**, 314-319. (2013); https://doi.org/10.1016/j.commatsci.2012.10.028

[94] P. Kaur, S. Chakraverty, A. K. Ganguli, and C. Bera, (2017). High anisotropic thermoelectric effect in palladium phosphide sulphide. *Physica Status Solidi (b)*, 254(9) (2017). https://doi:10.1002/pssb.201700021

[95] L. Bjerg, B. B. Iversen, and G. K. H. Madsen, *Phys. Rev. B* **89**, 024304 (2014), https://doi.org/10.1103/PhysRevB.89.024304

[96] R. Pässler, *J. Appl. Phys.* **101**, 093513 (2007); https://doi.org/10.1063/1.1753076

[97] A. Dal Corso, The thermo_pw software; https://dalcorso.github.io/thermo_pw

[98] M.T. Dove, *Structure and dynamics*, Oxford. (2003)

[99] G. A. Slack, *in Solid State Physics*, edited by F. S. Henry Ehrenreich and D. Turnbull (Academic, New York), Vol. 34, pp. 1-71 (1979)